

**Investigating the Binding Energy between Folic acid Receptor  $\alpha$   
and Functionalized Polymeric Drug Carrier and the use of  
Encapsulated Indium-Oxine for early diagnosis of Pancreatic  
Cancer**

**Étude de l'énergie de liaison entre le récepteur  $\alpha$  de l'acide folique  
et un transporteur de médicament polymérique fonctionnalisé et  
l'utilisation de l'indium-oxine encapsulé pour le diagnostic  
précoce du cancer du pancréas**

A Thesis Submitted to the Division of Graduate Studies of the Royal Military

College of Canada by

In Gue Chang, BSc, rmc

A/SLt

In Partial Fulfillment of the Requirement for the Degree of Master of Science

April 2025

©This thesis may be used within the Department of National Defence but  
copyright for open publication remains the property of the author.

If you can't fly, then run. If you can't run, then walk. If you can't walk, then crawl.

But whatever you do, you have to keep moving forward.

-Martin Luther King Jr.

## **Acknowledgements**

I would like to acknowledge those who helped throughout this journey. First and foremost, I would like to thank Dr. Cecile Malardier-Jugroot for her guidance, support, and encouragement, as well as for allowing me to understand what true research is. Thank you to Mr. Matt McTaggart for his guidance which led me to pursue research. Thank you also to Dr. Patrick Julien for his suggestions and ideas. I would also like to thank Dr. Olivier Lebel for his master knowledge in organic and Dr. Pavel Samuleev for running the neutron activation analysis. Thank you to Dr. Urs Häfeli for introduction and guidance with radioactive isotopes. Thank you to my friends and family for supporting me throughout this journey.

## Abstract

Pancreatic cancer is often referred to as the hardest cancer to diagnose due to its symptomless behaviour until the later stages. Patients are often diagnosed as stage 3, 4 or terminal by the time symptoms are detected. Thus, the 5-year survival rate is one of the lowest out of various cancers. The biggest challenge in treating and detecting cancer is the ability of the drug or the marker to specifically target the tumour cells without affecting the normal healthy cells. Interestingly, it has been found that pancreatic cancer overexpresses folic acid receptor alpha, FR $\alpha$ . This overexpression becomes a valuable target for targeted therapy. Folic acid (FA) can be conjugated with an amphiphilic polymer, poly (styrene-maleic acid), PSMA, using a linker, 2,4-diaminobutyric acid (DABA) to target preferentially cancer cells for detection or treatment. Previous *in vitro* studies have found significant decrease in the cancer cell viability when empty FA-DABA-PSMA was used. A main cause of this finding could be due to strong interaction between the FR $\alpha$  and FA-DABA-PSMA, where it may exert a significant increase in the binding energy, prohibiting the release of FR $\alpha$  and FA-DABA-PSMA and preventing the reuse of FA and FR $\alpha$  in metabolic preprocessed. When this phenomenon occurs, the cell produces more FR $\alpha$  on its surface, as the signaling loop will indicate that more FR $\alpha$  is needed on the surface of the cells to support its growth.

To determine the binding energy between FR $\alpha$  and FA-DABA-PSMA, computational studies using a quantum theoretical model were performed between FA with FR $\alpha$  and between FA-DABA-PSMA with FR $\alpha$ . The calculation was performed using ONIOM method. The results were compared between the FA and FA-DABA-PSMA along with experimental results obtained through microscale thermophoresis (MST). The comparison of results indicates that the FA-DABA-PSMA is unable to be released from the FR $\alpha$  despite a decrease in pH due to multiple hydrogen bonding between the maleic acid of the PSMA and hydrophilic amino acids at the surface of the receptor.

Next, the potential application of FA-DABA-PSMA as direct targeting radiopharmaceuticals for early diagnosis of tumours with FR $\alpha$  overexpression was investigated. To label the polymer, Indium 8-hydroxyquinoline (In-Oxine) was selected due to its hydrophobicity and suitability of <sup>111</sup>Indium as a gamma emitter. To determine the encapsulation of In-Oxine, fluorescence spectroscopy and neutron activation analysis (NAA) was conducted using non-radioactive In-Oxine. Thin layer chromatography (TLC) experiments were conducted using radioactive <sup>111</sup>In-Oxine to simulate an *in vivo* experiment. Three characterizations revealed the capability of FA-DABA-PSMA to encapsulate In-Oxine in its hydrophobic core.

## Résumé

Le cancer du pancréas est souvent considéré comme le cancer le plus difficile à diagnostiquer en raison de son absence de symptômes jusqu'aux stades avancés. Les patients sont souvent diagnostiqués aux stades 3, 4 ou terminale lorsque les symptômes sont détectés. Ainsi, le taux de survie à cinq ans est l'un des plus bas parmi les divers types de cancers. Le plus grand défi dans le traitement et la détection du cancer est la capacité du médicament ou du marqueur à cibler spécifiquement les cellules tumorales sans affecter les cellules saines normales. Fait intéressant, il a été constaté que le cancer du pancréas surexprime le récepteur de l'acide folique  $\alpha$ ,  $FR\alpha$ . Cette surexpression devient une cible précieuse pour la thérapie ciblée. L'acide folique (AF) peut être conjugué à un polymère amphiphile, le poly(styrène-acide maléique) (PSMA), à l'aide d'un lien, l'acide 2,4-diaminobutyrique (DABA), pour cibler préférentiellement les cellules cancéreuses en vue de leur détection ou traitement. Des études *in vitro* antérieures ont révélé une diminution significative de la viabilité des cellules cancéreuses lorsque le FA-DABA-PSMA vide était utilisé. Une cause principale de cette constatation pourrait être due à l'interaction forte entre le  $FR\alpha$  et le FA-DABA-PSMA, où cela pourrait entraîner une augmentation significative de l'énergie de liaison, empêchant la libération du  $FR\alpha$  et du FA-DABA-PSMA, et empêchant ainsi la réutilisation de l'AF et du  $FR\alpha$  dans le métabolisme prétraité. Lorsque ce phénomène se produit, la cellule produit davantage de  $FR\alpha$  à sa surface, car la boucle de signalisation indiquera qu'il faut plus de  $FR\alpha$  à la surface des cellules pour soutenir sa croissance.

Pour déterminer l'énergie de liaison entre  $FR\alpha$  et FA-DABA-PSMA, des études computationnelles utilisant un modèle théorique quantique ont été réalisées entre FA et  $FR\alpha$  et entre FA-DABA-PSMA et  $FR\alpha$ . Le calcul a été effectué en utilisant la méthode ONIOM. Les résultats ont été comparés entre le FA et le FA-DABA-PSMA, ainsi qu'avec les résultats expérimentaux obtenus par thermophoresis à l'échelle microscopique (MST). La comparaison des résultats indique que le FA-DABA-PSMA ne peut pas être libéré du  $FR\alpha$  malgré une diminution du pH, en raison de multiples liaisons hydrogène entre l'acide maléique du PSMA et les acides aminés hydrophiles à la surface du récepteur.

Ensuite, l'application potentielle du FA-DABA-PSMA en tant que radiopharmaceutiques de ciblage direct pour le diagnostic précoce des tumeurs avec surexpression de  $FR\alpha$  a été explorée. Pour marquer le polymère, l'indium 8-hydroxyquinoline (In-Oxine) a été sélectionné en raison de son hydrophobicité et de la convenance de l'indium-111 en tant qu'émetteur gamma. Pour déterminer l'encapsulation de l'In-Oxine, des analyses de spectroscopie de fluorescence et d'activation neutronique (NAA) ont été réalisées en utilisant de l'In-Oxine non radioactif. Des expériences de chromatographie sur couche mince (TLC) ont été menées avec de l'In-Oxine radioactif  $^{111}\text{In}$  pour simuler une expérience *in vivo*. Trois caractérisations ont révélé la capacité du FA-DABA-PSMA à encapsuler l'In-Oxine dans son noyau hydrophobe.

## Table of Contents

|   |           |
|---|-----------|
| <b>Acknowledgements .....</b>                                 | <b>3</b>  |
| <b>Abstract.....</b>  | <b>4</b>  |
| <b>Résumé.....</b>  | <b>5</b>  |
| <b>List of Tables .....</b>                                   | <b>9</b>  |
| <b>List of Figures.....</b>                                   | <b>10</b> |
| <b>1. Introduction.....</b>                                   | <b>15</b> |
| 1.1. Cancer.....  | 15        |
| 1.1.1. Types of Cancer .....                                  | 15        |
| 1.1.2. Cause / Origin .....                                   | 16        |
| 1.1.2.1. Physical Factors .....                               | 16        |
| 1.1.2.2. Chemical Factors .....                               | 17        |
| 1.1.2.3. Biological Factors .....                             | 17        |
| 1.1.3. Pancreatic Cancer.....                                 | 18        |
| 1.2. Treatment .....  | 19        |
| 1.2.1. Surgery .....  | 20        |
| 1.2.2. Chemotherapy .....                                     | 20        |
| 1.2.3. Other Treatment Options and Combinations of Treatments | 21        |
| 1.3. Drug Delivery System .....                               | 22        |
| 1.3.1. Nanoparticles .....                                    | 22        |
| 1.3.2. Poly (styrene- <i>alt</i> -maleic acid) .....          | 23        |
| 1.3.3. Encapsulation – Hydrophobic Molecules .....            | 24        |
| 1.4. Radioactive Tracers.....                                 | 25        |
| 1.4.1. <sup>111</sup> Indium .....                            | 25        |
| 1.4.2. <sup>111</sup> In-Oxyquinoline (Oxine).....            | 26        |
| 1.5. Direct targeting Strategy .....                          | 27        |
| 1.5.1. Folic Acid (FA).....                                   | 27        |
| 1.5.2. Folic Acid Receptor Alpha (FR $\alpha$ ).....          | 29        |
| 1.5.3. Polymeric Targeted Carrier.....                        | 32        |
| 1.6. Research Objective.....                                  | 34        |
| <b>2. Methods.....</b>  | <b>36</b> |

|  |           |
|--|-----------|
| 2.1. Basic Quantum Theory.....   | 36        |
| 2.2. Wavefunction Approximation.....                                   | 38        |
| 2.3. Basis Sets.....   | 38        |
| 2.3.1. 3-21G .....   | 39        |
| 2.3.2. 6-31G** (d,p).....  | 40        |
| 2.4. The Variational Principle .....                                   | 40        |
| 2.5. Hartree Fock.....   | 41        |
| 2.6. Density Functional Theory .....                                   | 41        |
| 2.6.1. Hohenberg-Kohn Theory .....                                     | 42        |
| 2.6.2. Kohn-Sham method .....  | 44        |
| 2.6.3. Exchange-correlation Energy .....                               | 45        |
| 2.6.4. Hybrid Functionals.....   | 45        |
| 2.7. Semi Empirical.....   | 46        |
| 2.8. Molecular Mechanics .....   | 46        |
| 2.8.1. Force Field Models .....  | 47        |
| 2.9. Conclusion.....   | 49        |
| <b>3. Experimental Methods .....</b>                                   | <b>50</b> |
| 3.1. Microscale Thermophoresis (MST) .....                             | 50        |
| 3.2. Fluorescence Spectroscopy .....                                   | 51        |
| 3.3. Neutron Activation Analysis (NAA).....                            | 53        |
| 3.4. Thin Layer Chromatography .....                                   | 54        |
| 3.5. Phosphor Imaging.....   | 55        |
| <b>4. Computational Results .....</b>                                  | <b>57</b> |
| 4.1. Introduction .....  | 57        |
| 4.2. Methods.....  | 58        |
| 4.3. Results and Discussion.....                                       | 59        |
| 4.3.1. Method #1 .....   | 59        |
| 4.3.1.1. Interaction of FA with FR $\alpha$ .....                      | 60        |
| 4.3.1.2. Interaction of FA-DABA-PSMA with FR $\alpha$ .....            | 64        |
| 4.3.2. Method #2 .....   | 72        |
| 4.3.2.1. Interaction of FA with FR $\alpha$ optimized with 3-21G ..... | 72        |

|  |            |
|--|------------|
| 4.3.2.2. Interaction of FA with FR $\alpha$ optimized using 6-31G** .... | 76         |
| 4.3.2.3. Interaction of FA-DABA-PSMA with FR $\alpha$ .....              | 82         |
| 4.4. Conclusion.....   | 89         |
| <b>5. Microscale Thermophoresis.....</b>                                 | <b>91</b>  |
| 5.1. Introduction .....  | 91         |
| 5.2. Methods.....  | 91         |
| 5.3. Results and Discussion.....   | 92         |
| 5.4. Conclusion.....   | 96         |
| <b>6. Indium Oxine Encapsulation .....</b>                               | <b>97</b>  |
| 6.1. Introduction .....  | 97         |
| 6.2. Methods.....  | 98         |
| 6.3. Results and Discussion.....   | 99         |
| 6.3.1. Non-Radioactive Indium-Oxine.....                                 | 99         |
| 6.3.1.1. Fluorescence Spectroscopy.....                                  | 99         |
| 6.3.1.2. Neutron Activation Analysis.....                                | 106        |
| 6.3.2. Radioactive In-Oxine .....  | 110        |
| 6.3.2.1. Thin Layer Chromatography.....                                  | 111        |
| 6.4. Conclusion.....   | 114        |
| <b>7. Conclusion and Future Outlook .....</b>                            | <b>116</b> |
| <b>8. Reference .....</b>  | <b>119</b> |



## List of Tables

|   |     |
|---|-----|
| <b>Table 1.</b> List of amino acids and interaction with FA at pH 7.4 .....   | 62  |
| <b>Table 2.</b> List of amino acids and interaction with FA at pH 5.5 .....   | 63  |
| <b>Table 3.</b> List of amino acids and interaction with FA-DABA-PSMA at pH 7.4 ...   | 66  |
| <b>Table 4.</b> List of amino acids and interaction with FA-DABA-PSMA at pH 5.5 ...   | 69  |
| <b>Table 5.</b> Summary of binding and interaction energy using method #1 .....   | 70  |
| <b>Table 6.</b> List of amino acids and interaction with FA at pH 7.4 .....   | 73  |
| <b>Table 7.</b> List of amino acids and interaction with FA at pH 5.5 .....   | 75  |
| <b>Table 8.</b> List of amino acids and interaction with FA at pH 7.4 .....   | 77  |
| <b>Table 9.</b> List of amino acids and interaction with FA at pH 5.5 .....   | 79  |
| <b>Table 10.</b> Summary of binding and interaction energy between FA and FR $\alpha$ using<br>method # 2, 3-21G vs 6-31G** ..... | 81  |
| <b>Table 11.</b> List of amino acids and interaction with FA-DABA-PSMA at pH 7.4 .  | 84  |
| <b>Table 12.</b> List of amino acids and interaction with FA-DABA-PSMA at pH 5.5 .  | 87  |
| <b>Table 13.</b> Summary of binding and interaction energy between FA-DABA-PSMA<br>and FR $\alpha$ using method # 2, 3-21G .....  | 88  |
| <b>Table 14.</b> NAA results of sample used for fluorescence spectroscopy .....   | 106 |
| <b>Table 15.</b> NAA result of diluted samples from Table 14 .....  | 107 |
| <b>Table 16.</b> Control Test of In-Oxine in PBS.....   | 107 |
| <b>Table 17.</b> FA-DABA-PSMA with EtOH as a solvent for In-Oxine.....  | 108 |
| <b>Table 18.</b> 3 $\mu$ M vs 200 $\mu$ M concentration test of FA-DABA-PSMA .....  | 109 |
| <b>Table 19.</b> 500 $\mu$ M vs 2000 $\mu$ M concentration test of FA-DABA-PSMA .....   | 110 |

## List of Figures

|  |    |
|--|----|
| Figure 1. An example of Whipple procedure where the head of pancreas, duodenum, bile duct, gallbladder, and lymph nodes are removed along with tumour..... | 20 |
| Figure 2. Different types of nanoparticles are used as nanomedicine.....   | 23 |
| Figure 3. Self-Assembly of 350 kDa PSMA into sheets with hydrophobic inner core represented as blue and hydrophilic outer core represented as red.....     | 24 |
| Figure 4. Decay Diagram of $^{111}\text{In}$ with spins and energies of different excitation levels .....  | 26 |
| Figure 5. Chemical structure of $^{111}\text{In}$ Oxine. Three Oxine chelated to $^{111}\text{In}$ ...   | 26 |
| Figure 6. Image of $^{111}\text{In}$ -labeled leukocyte accumulation in the infected prosthetic vascular graft in the right thigh (arrowheads).....        | 27 |
| Figure 7. Different conjugation of functional compounds and chelator on FA .....   | 28 |
| Figure 8. Folate cycle and methionine cycle. Folic acid acts as a starting compound to initiate the cycle which leads to DNA synthesis.....                | 29 |
| Figure 9. Pathway of $\text{FR}\alpha$ in the cell after endocytosis or binds with GP130 .....   | 30 |
| Figure 10. Cross-section of $\text{FR}\alpha$ with docked FA displaying hydrogen bonds in green dotted line and hydrophobic interaction in red line .....  | 31 |
| Figure 11. Binding Energy $K_d$ between different amino acids in the receptor and FA .....   | 31 |
| Figure 12. Charge distribution of $\text{FR}\alpha$ on -3 eV to +3 eV electrostatic scale.....   | 32 |
| Figure 13. Synthesis pathway of FA-DABA-PSMA. FA is linked with linker 2,4 – diamino butyric acid before PSMA is added. ....                               | 33 |
| Figure 14. Mechanism of action of FA-DABA-PSMA targeting .....   | 34 |
| Figure 15. Representation of the mechanism of MST and the data obtained .....  | 51 |
| Figure 16. Jablonski diagram representing the excitation and fluorescence emission .....   | 52 |
| Figure 17. Diagram of the fluorometer with excitation and emission monochromators .....  | 53 |

|  |    |
|--|----|
| Figure 18. Cross section of High Purity Germanium detectors with p-type and n-type bands with movements of electrons .....   | 54 |
| Figure 19. The different intensities in the phosphor screen depend on the radioactivity of the compound. ....  | 55 |
| Figure 20. The electron movement due to radiation, low energy photon excitation, and emission of photons .....   | 56 |
| Figure 21. Overview of the FA and FR $\alpha$ with amino acids that interact FA are represented as Balls and sticks, rest of the proteins as wireframe and FA as a tube at pH 7.4..... | 60 |
| Figure 22. Hydrogen bonding between FA and amino acid (D81, R106 and H135) in the FR $\alpha$ at pH 7.4.....   | 60 |
| Figure 23. Hydrogen bonding between FA and amino acid (W102, K136, G137, and W140) in the FR $\alpha$ at pH 7.4.....   | 61 |
| Figure 24. Hydrophobic Interaction between FA and amino acid (Y85, W171, and Y175) in the FR $\alpha$ at pH 7.4.....   | 61 |
| Figure 25. Hydrogen bonding between FA and amino acid (D81, R106, and H135) in the FR $\alpha$ at pH 5.5.....  | 62 |
| Figure 26. Hydrogen bonding between FA and amino acid (W102, K136, G137, and W140) in the FR $\alpha$ at pH 5.5 .....  | 63 |
| Figure 27. Hydrogen bonding between FA-DABA-PSMA and amino acid (D81, R103, and R106) in the FR $\alpha$ at pH 7.4 .....   | 64 |
| Figure 28. Hydrogen bonding between FA-DABA-PSMA and amino acid (G137, W138, and W140) in the FR $\alpha$ at pH 7.4 .....  | 65 |
| Figure 29. Hydrogen bonding between FA-DABA-PSMA and amino acid (D99 and K136) in the FR $\alpha$ at pH 7.4.....   | 65 |
| Figure 30. Top view of the PSMA chain with a green line to present the linearity of the polymer backbone.....  | 66 |
| Figure 31. Hydrogen bonding between FA-DABA-PSMA and amino acid (D81 and H135) in the FR $\alpha$ at pH 5.5.....   | 67 |

|  |    |
|--|----|
| Figure 32. Hydrogen bonding between FA-DABA-PSMA and amino acid (W102, G137, and W140) in the FR $\alpha$ at pH 5.5 .....                                | 67 |
| Figure 33. Hydrogen bonding between FA-DABA-PSMA and amino acid (D99, Q100, S101 and G137) in the FR $\alpha$ at pH 5.5.....                             | 68 |
| Figure 34. Top view of the PSMA chain with a green line to present the bending of the polymer backbone.....  | 68 |
| Figure 35. Top view of PSMA hexamer with a green line representing the linear backbone carbon chain.....   | 69 |
| Figure 36. Hydrogen bonding between FA and amino acid (D81, R106, H135, and S174) in the FR $\alpha$ at pH 7.4. Optimized using DFT 3-21G .....          | 72 |
| Figure 37. Hydrogen bonding between FA and amino acid (K136, G137, and W140) in the FR $\alpha$ at pH 7.4. Optimized using DFT 3-21G .....               | 72 |
| Figure 38. Hydrogen bonding between FA and amino acid (R103, R106, and S174) in the FR $\alpha$ at pH 5.5. Optimized using DFT 3-21G.....                | 74 |
| Figure 39. Hydrogen bonding between FA and amino acid (K136, G137, and W140) in the FR $\alpha$ at pH 5.5. Optimized using DFT 3-21G .....               | 74 |
| Figure 40. Hydrogen bonding between FA and amino acid (D81, R106, S174, and H135) in the FR $\alpha$ at pH 7.4. Optimized using DFT 6-31G** .....        | 76 |
| Figure 41. Hydrogen bonding between FA and amino acid (G137, K137, and W140) in the FR $\alpha$ at pH 7.4. Optimized using DFT 6-31G** .....             | 76 |
| Figure 42. Hydrogen bonding between FA and amino acid (R103, S174, and Y175) in the FR $\alpha$ at pH 5.5. Optimized using DFT 6-31G**.....              | 78 |
| Figure 43. Hydrogen bonding between FA and amino acid (R103, K136, G137, and W140) in the FR $\alpha$ at pH 5.5. Optimized using DFT 6-31G** .....       | 78 |
| Figure 44. The structure of FA at pH 7.4 from the FR $\alpha$ complex. The complex was optimized using basis set 6-31G**.....                            | 80 |
| Figure 45. The structure of FA at pH 5.5 from the FR $\alpha$ complex. The complex was optimized using basis set 6-31G**.....                            | 80 |
| Figure 46. Hydrogen bonding between FA-DABA-PSMA and amino acid (D81, R103, R106, and S174) in the FR $\alpha$ at pH 7.4. Optimized using DFT 3-21G..... | 82 |

|  |     |
|--|-----|
| Figure 47. Hydrogen bonding between FA-DABA-PSMA and amino acid (K136, G137, W138, and W140) in the FR $\alpha$ at pH 7.4. Optimized using DFT 3-21G ..... | 83  |
| Figure 48. Hydrogen bonding between FA-DABA-PSMA and amino acid (V98, Q100, S101, and W102) in the FR $\alpha$ at pH 7.4. Optimized using DFT 3-21G        | 83  |
| Figure 49. Top view of the PSMA chain with a green line to present the bending of the polymer backbone.....  | 84  |
| Figure 50. Hydrogen bonding between FA-DABA-PSMA and amino acid (R103, R106, and S174) in the FR $\alpha$ at pH 5.5. Optimized using DFT 3-21G.....        | 85  |
| Figure 51. Hydrogen bonding between FA-DABA-PSMA and amino acid (W102, G137, W138, AND W140) in the FR $\alpha$ at pH 5.5. Optimized using DFT 3-21G ..... | 86  |
| Figure 52. Hydrogen bonding between PSMA and amino acid (V98, D99, S101, and K136) in the FR $\alpha$ at pH 5.5. Optimized using DFT 3-21G.....            | 86  |
| Figure 53. Top view of the FA-DABA-PSMA chain at pH 5.5 with a green line to present the bending of the polymer backbone .....                             | 87  |
| Figure 54. Binding affinity curve of FA-DABA-PSMA 350 kDa at pH 7.5 .....  | 93  |
| Figure 55. Binding affinity curve of FA-DABA-PSMA 20 kDa at pH 7.5 .....   | 94  |
| Figure 56. Binding affinity curve of FA-DABA-PSMA 350 kDa at pH 7.5 .....  | 95  |
| Figure 57. Binding affinity curve of FA-DABA-PSMA 20 kDa at pH 5.5 .....   | 95  |
| Figure 58. 3D EEM plot of Indium-Oxine.....  | 99  |
| Figure 59. 3D EEM plot of FA-DABA-PSMA 350 kDa.....  | 100 |
| Figure 60. 2D Emission plot converted from 3D EEM plot of FA-DABA-PSMA 350 kDa.....  | 100 |
| Figure 61. 3D EEM plot of FA-DABA-PSMA 20 kDa.....   | 101 |
| Figure 62. 2D Emission plot converted from 3D EEM plot of FA-DABA-PSMA 20 kDa.....   | 101 |
| Figure 63. 3D EEM plot of 0.3 mg of In-Oxine added to FA-DABA-PSMA 350   | 102 |
| Figure 64. 2D Emission plot converted from 3D EEM of 350 kDa and In-Oxine  | 102 |

|  |     |
|--|-----|
| Figure 65. 3D EEM plot of 0.3 mg of In-Oxine added to FA-DABA-PSMA 20 kDa .....                                | 103 |
| Figure 66. 2D Emission plot converted from 3D EEM of 20 kDa and In-Oxine .                                     | 103 |
| Figure 67. 3D EEM plot of In-Oxine dissolved in DMSO added to FA-DABA-PSMA 350 kDa.....                        | 104 |
| Figure 68. 2D emission plot from 3D EEM plot of In-Oxine dissolved in DMSO added to FA-DABA-PSMA 350 kDa ..... | 104 |
| Figure 69. 3D EEM plot of In-Oxine dissolved in DMSO added to FA-DABA-PSMA 20 kDa.....                         | 105 |
| Figure 70. 2D emission plot from 3D EEM plot of In-Oxine dissolved in DMSO added to FA-DABA-PSMA 20 kDa .....  | 105 |
| Figure 71. Lateral view of TLC of free $^{111}\text{In}$ -Oxine .....  | 111 |
| Figure 72. Summary of TLC of free $^{111}\text{In}$ -Oxine.....  | 111 |
| Figure 73. Lateral view of TLC of FA-DABA-PSMA 350 kDa with $^{111}\text{In}$ -Oxine.....                      | 112 |
| Figure 74. Summary of TLC of FA-DABA-PSMA 350 kDa with $^{111}\text{In}$ -Oxine....                            | 112 |
| Figure 75. Lateral view of TLC of FA-DABA-PSMA 20 kDa with $^{111}\text{In}$ -Oxine. ....                      | 113 |
| Figure 76. Summary of TLC of FA-DABA-PSMA 20 kDa with $^{111}\text{In}$ -Oxine.....                            | 113 |

## **1. Introduction**

### **1.1. Cancer**

In the 1800s, the life expectancy was about 35 years for an average person. Conversely, in 2021, the world average life expectancy increased to 71 years<sup>1</sup>. With a detailed understanding of human physiology and medical research, humanity has made significant advancements toward treating all life-threatening diseases. Yet, cancer remains the biggest challenge in the medical field despite enormous ongoing research. According to WHO, in 2020, cancer alone caused over 10 million deaths, contributing 17% of worldwide death counts<sup>2</sup>. Cancer cells are malignant tumour that have mutated from healthy cells caused by DNA damage or genetic and epigenetic mutation<sup>3</sup>. The mutations are often heavily regulated and repaired by either cell's DNA repair mechanisms or killed by the immune system; however, cancer cells often have the ability to impair activation of the systems<sup>4</sup>. As a result, the cancer cells are able to proliferate uncontrollably at an exponential rate, generating a tumour microenvironment and inhibiting the function of healthy cells. As the healthy cells become impaired and unable to function properly, it ultimately leads to an organ failure, leading to death<sup>5</sup>. DNA damage can be caused internally; by replication error, DNA base mismatch, oxidation, hydrolysis, and alkylation and external damages are caused by chemicals, ionizing radiation, and ultraviolet (UV) radiation<sup>6</sup>. The cancer cells during tumour growth progression are highly unstable, and they continue to mutate and compete with each other. Ultimately, a group of cells that exerts dominance in rapid growth, invasion, and survival leads to metastasis. Metastasis occurs when the cancer cells enter the blood and or lymph vessels and begin forming a new tumour in a different organ in the body<sup>7</sup>. The bloodstream poses enormous stress on foreign cells with fluid pressure and immune cells, yet the cancer cells that are able to undergo metastasis are able to survive such conditions. These cells attach to an organ and begin forming new tumour microenvironments with an ability to evade immunological signals and withstand chemotherapy if treatment is ongoing<sup>7</sup>. These metastasized cells pose challenges in detection and treatment due to positive mutations for the tumour cells, causing difficulty in treatment as they become resistant to the treatments<sup>8</sup>.

#### **1.1.1. Types of Cancer**

Cancer is a generic term for a large group of disease, indeed, more than 200 different types of cancers have been identified<sup>9</sup>. With such a number, cancer can be classified into three broad categories: solid, blood, and mixed. The main difference between the three are its the origin of formation. Solid cancers include carcinomas, which originate from epithelial tissues, and sarcomas, from connective or supportive tissues of the body<sup>10</sup>. The carcinomas can be further classified into different subtypes including adenocarcinoma (breast, colon and prostate), basal cell carcinoma (outer layer of skin), squamous cell carcinoma (under skin, stomach, intestines, lungs,

bladder, and kidney), and transitional cell carcinoma (bladder, ureters, and kidneys)<sup>3</sup>. The name of the cancers originates based on the types of cells present in different organs in the body<sup>11</sup>. Examples of sarcoma include osteosarcoma (bone), chondrosarcoma (cartilage), and rhabdomyosarcoma or leiomyosarcoma (muscle cells). Next, blood cancers are types of cancers that originate from the blood or the lymphatic system. They are broken down into leukemia (white blood cells), lymphoma (lymph glands), and multiple myeloma (plasma cells). Lastly, mixed cancers are types of cancer that involve two types of solid or blood cancer. Examples include carcinosarcoma (a mixture of carcinoma and sarcoma) and adenosquamous carcinoma (squamous and gland)<sup>9,10</sup>. These different types of cancer have various rates of growth, symptoms, and the malignancy they pose, along with their metastasis capability<sup>12</sup>. Furthermore, the frequency of occurrence among the population, the diagnosis likelihood ratio, and the 5-year survival rate are heavily varied among the cancers<sup>13</sup>.

### **1.1.2. Cause / Origin**

Carcinogenesis, oncogenesis, or tumorigenesis are the terms used to describe the formation of cancer. Cancer cells originate from healthy cells in the body and due to exogenous or endogenous factors, the healthy cells undergo mutation to form cells that proliferate at an abnormal rate<sup>10</sup>. This proliferation expands to overtake the healthy required cells for the organs. This takeover results in organ failure, eventually leading to a person's death unless organ transplantation is possible. Unfortunately, the cause of cancer is due to multiple factors, including physical, chemical, biological, and viral<sup>14-16</sup>. These factors share a similar characteristic of causing DNA damage or mutation. The damage or mutation to the DNA causes changes in the DNA, which triggers the initiation of the DNA repair mechanism. When this system fails, as a result, cancer cells are formed and begin to proliferate uncontrollably<sup>15</sup>. There are five different types of DNA damage caused by the three factors. Base mismatch, single-strand break, double-strand break, interstrand crosslink, and bulky intrastrand crosslinks<sup>17</sup>. Currently, the International Agency for Research on Cancer (IARC) of the World Health Organization (WHO) has classified 132 agents into Group 1, carcinogenic to humans, 96 agents into Group 2A, probably carcinogenic to humans, 320 agents into Group 2B, possibly carcinogenic to humans, and 499 agents to group 3: not classifiable as to its carcinogenicity to humans<sup>18</sup>.

#### **1.1.2.1. Physical Factors**

Non-ionizing radiation and ionizing radiation are the two main carcinogens in the physical factor. However, within the non-ionizing radiation spectrum, ultraviolet (UV) is the only source that causes cancer<sup>19</sup>. The ionizing radiation is classified into electromagnetic waves radiation (gamma or x-rays) and particle radiation (neutrons, beta, and alpha), and both of them are classified into IARC Group 1 carcinogens. Ionizing radiation has enough energy to release electrons from



atoms, which can have a primary effect by breaking the covalent bonds, causing single-strand or double-strand breakage and a secondary effect of generating reactive oxygen species (ROS), which causes oxidative damage to the DNA<sup>20</sup>. Exposure to ionizing radiation is the key to causing cancer, as increasing the exposure time and dosage exponentially increases the possibility of cancer. If a person is exposed to an acute radiation poisoning, more than 2 sieverts (Sv), a person's chromosomes may be completely destroyed.

### **1.1.2.2. Chemical Factors**

Among the three factors, chemical factors are the major contributors to carcinogenesis. Numerous chemicals have been identified as carcinogens, and some chemicals include compounds that can easily be exposed to. From IARC group 1, examples include acetaldehyde, ethanol in alcoholic beverages, arsenic, benzene, coal tar, formaldehyde, outdoor pollution, perfluorooctanoic acid (PFOA), silica gel, and wood dust<sup>18</sup>. Within groups 1, 2A, and 2B, the chemical substances are the main category out of the physical, chemical, and biological factors. Due to the diverse types of chemicals included, the exact mechanism of action varies<sup>21</sup>. Yet, in common, they either cause ROS radicals or DNA damage. The chemicals can be exposed through inhalation, ingestion, injection, or absorption. Unlike radiation, where strict restrictions are applied, chemical exposures can often occur without any realization of exposure<sup>22</sup>.

### **1.1.2.3. Biological Factors**

The biological factors include viruses, bacteria, and worms, with viruses being the main contributors among the pathogens<sup>23</sup>. Unlike physical or chemical factors, where exposure is the key, biological factors are based on infection by the pathogens. Viruses include Human Papillomaviruses (HPVs), Epstein-Barr virus (EBV), Hepatitis B virus (HBV), Hepatitis C virus (HCV), Human Immunodeficiency virus (HIV), Human Herpes virus 8 (HHV-8), Human T-lymphotropic virus-1 (HTLV-1), and Merkel cell polyomavirus (MCV)<sup>24</sup>. Viruses act as carcinogens by generating ROS species and causing DNA damage. However, in comparison to chemical DNA damage, viruses directly cause changes in the DNA by implementing their own, breaking the DNA of the original healthy cell and inactivation of p53 protein which is known to be a tumour suppressor<sup>25</sup>. Furthermore, the infection and damage to the DNA result in inflammation of the area, which has been found to promote cancer as it induces cell proliferation and activation of inflammatory cells. This increases ROS at the cellular level, which leads to oxidative DNA damage and reduces the DNA repair mechanism<sup>26</sup>. There are two bacteria, *Helicobacter pylori* and *Chlamydia trachomatis*, that are carcinogenic. Bacteria have an interesting property, as unlike other factors, it has been known to cause cancer when they become a long-term infection by damaging the organ and causing inflammation<sup>27</sup>. Lastly, there are three different IARC group 1 parasites: *Clonorchis sinensis*, *Opisthorchis viverrini*, and *Schistosoma haematobium*. The three are

flatworms with *Clonorchis sinensis* and *Opisthorchis viverrini* being liver flukes and *Schistosoma haematobium* being a blood fluke. Similar to carcinogenic bacteria, the parasites become carcinogenic as they become a long-term infection, causing a series of inflammation, ROS generation, and physical damage<sup>28</sup>.

With such diverse types of cancers and causes, specific cancers must be selected to understand the pathology, activate signalling pathways and specifications and characteristics of the cancer.

### **1.1.3. Pancreatic Cancer**

Among various high-proliferating cancer cells, pancreatic cancer cells have been considered one of the deadliest. It has been reported that the five-year survival rate of pancreatic cancer is 5 to 10 percent, while patients with stage IV have a five-year survival rate that decreases to less than one percent<sup>29</sup>. This poor survival rate is directly related to poor and late diagnosis. Pancreatic cancer is symptomless until it reaches stage 3 or 4, which brings difficulty as at this stage, metastasis have already occurred. As previously described, cancer becomes extremely difficult to cure when metastasizing begins, as the cells become more resistant to chemotherapy and invade multiple organs in the body. This limits the treatment options as multiple organ failure is impossible to treat. Pancreatic cancers are particularly highly invasive and proliferate rapidly. Furthermore, as it is symptomless, it is extremely difficult to make an early diagnosis. Some common signs and symptoms could be caused by cancer however, they overlap with common sickness symptoms and are often ignored until the tumour has progressed to advanced stages.

Pancreatic cancer is a solid adenocarcinoma cancer that can be classified into two main types: exocrine and neuroendocrine tumours. Exocrine tumours form from exocrine cells of the pancreas, which make up 95% of the pancreas, with its main function of producing digestive enzymes for the body<sup>30</sup>. The exocrine tumours account for over 90% of pancreatic cancer, with adenocarcinoma as the most common type<sup>10</sup>. Adenocarcinoma is a type of cancer that originates from the glands in the organs. Neuroendocrine tumours are developed from the endocrine system of the pancreas and are made of islet cells that play a key role in generating hormones and releasing them into the bloodstream. Neuroendocrine tumours are typically slow growing compared to exocrine tumours and due to their involvement with hormones, the blood sugar level and gastric acid are heavily impacted<sup>31</sup>. It is also worth mentioning that diabetes and pancreatic cancers are highly correlated, as one of the early symptoms of pancreatic cancer is diabetes, as the function of the pancreas begins to fail<sup>32</sup>.

Currently, there are multiple possible diagnostic protocols including blood tests, computed tomography (CT) scans, positron emission spectroscopy (PET), endoscopic retrograde cholangiopancreatography (ERCP), endoscopic ultrasound, magnetic resonance imaging (MRI), and biopsy using tissue tests<sup>33</sup>. With the

diagnostic tools, the tumour, node, metastasis (TNM) model is used for classifying the stage of pancreatic cancer<sup>34</sup>.

- Tumour size (T):
  - o TX: Tumour cannot be assessed
  - o T0: No evidence of a tumour
  - o Tis: Carcinoma in tissue
  - o T1: Tumour size less than 2 cm
  - o T2: Tumour size larger than 2 cm but less than or equal to 4 cm
  - o T3: Tumour size larger than 4cm
  - o T4: Tumour has grown into the celiac axis, superior mesenteric artery and common hepatic artery
- Lymph node (N):
  - o NX: Lymph nodes cannot be assessed
  - o N0: Tumour has not spread into a lymph node
  - o N1: Tumour has spread to one to three lymph nodes
  - o N2: Tumour has spread to four or more lymph nodes
- Metastasis status (M):
  - o The tumour has not spread
  - o The tumour has spread to other organs and lymph nodes

After diagnosis of the cancer, various treatment options are explored to find the best treatment method with minimum side effects it may pose on the patient.

## 1.2. Treatment

Currently, there are multiple treatment options available, such as surgery, radiation therapy, chemotherapy, chemoradiation therapy, and targeted therapy<sup>35</sup>. The type of treatment and plan is determined by the patient and healthcare team, comprising an oncologist and a general surgeon. However, even with multiple treatment options, treatment refusal is present among patients<sup>36,37</sup>. This refusal derives from severe adverse side effects to the body, including hair loss, fatigue, nausea, diarrhea, and vomiting<sup>38</sup>. Furthermore, it should be noted that the majority of the patients who are diagnosed with pancreatic cancer are between 50-70+ years old<sup>36</sup>. While surgical removal is often the optimal treatment option with minimized side effects, it is limited by the stage of the cancer and the patient's age, as a person who is over 70 years old can't undergo an extended surgery. In the late stage of the cancer, surgical treatment is impossible as it would lead to the removal of the majority of the organs, and if the patient is old and organ transplantation is unavailable, the surgery becomes difficult. An alternative and popular method is chemotherapy, yet the patients experience adverse side effects during the treatment.

### 1.2.1. Surgery

Three common types of surgery include the Whipple procedure, total pancreatectomy, and distal pancreatectomy<sup>39</sup>. Whipple procedure is for patients with cancer in the pancreas head and the surgeon removes the head of the pancreas, duodenum, and gall bladder and reattaches the pancreas and the stomach directly to the small intestine as seen in *Figure 1*. Total pancreatectomy removes the pancreas, duodenum, gall bladder, and nearby lymph nodes, and directly attaches the stomach to the small intestine. Distal pancreatectomy removes the tail of the pancreas and the spleen that is attached to it<sup>40</sup>. As described, surgery is one of the optimal ways to remove the majority of the cancer. However, an adjuvant treatment is often necessary as a follow-up after the surgery. Surgery is highly invasive and causes major stress to the body, as it can take between 4 to 12 hours. Furthermore, the surgeries involve removing major organs such as stomach, bile duct, gallbladder, duodenum, pancreas, and small intestine which are vital organs for the body. With such major surgery, the recovery time of the surgery is often very lengthy, and as previously mentioned, patients who are diagnosed with pancreatic cancer are often aged. Thus, the complexity of the surgery, recovery time, and financial burden lead to the refusal of the treatment by the patients. Finally, the surgery can remove tumours that are visually seen by the operator during the surgery, which poses challenges as small tumours or tumours proliferating slowly at the cellular level that are too small to be seen can't be identified and removed<sup>41</sup>.

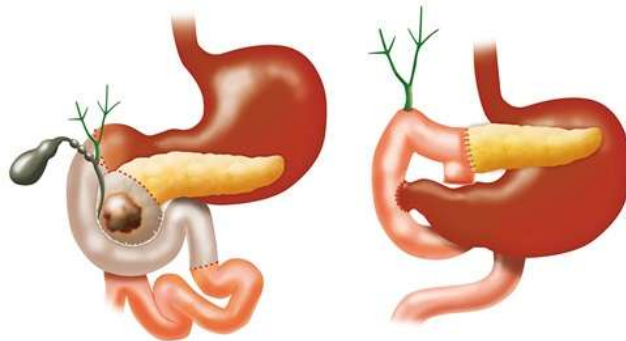


Figure 1. An example of Whipple procedure where the head of pancreas, duodenum, bile duct, gallbladder, and lymph nodes are removed along with tumour.

(Reproduced from Ref <sup>42</sup>)

### 1.2.2. Chemotherapy

Among various treatment options, chemotherapy, along with surgery and radiation therapy, is most commonly used for treatment and as an adjuvant<sup>43</sup>. The chemotherapeutic drugs are classified under five different categories: alkylating agents, antimetabolites, antitumour antibiotics, topoisomerase inhibitors, and mitotic

inhibitors<sup>44</sup>. The chemotherapeutic drugs share a similar mechanism, which is either damaging the DNA, RNA, and/or proteins or disrupting the cell cycle. Alkylating agents exert their effects by covalently bonding with amino, carboxyl, sulfhydryl, and phosphate groups of DNA, RNA, and proteins in the cell<sup>45</sup>. Within the alkylating agents, nitrosoureas are a group that is able to cross through the blood-brain barrier (BBB). This ability is unique as BBB is very difficult to cross for all chemotherapeutic drugs as the barrier is highly selective and limited compounds can pass through<sup>46</sup>. Antimetabolites interfere with the building blocks of DNA and RNA and are effective in cells in the S phase of the cell cycle. This disrupts the cell cycle, leading to a stoppage of the cell cycle and proliferation. Anthracyclines are part of antitumour antibiotics that bind directly to DNA base pairs and inhibit DNA topoisomerase I and II which directly causes disruption to the DNA, preventing DNA replication<sup>47</sup>. Topoisomerase inhibitors are similar to antitumour antibiotics as they directly interfere with topoisomerase, preventing DNA separation. Finally, mitotic inhibitors prevent cell division and damage the cells throughout the cell cycle.

With various types of chemotherapeutic drugs that are approved by the FDA, the challenge to minimize the side effects and increase efficiency remains a difficult one. Chemotherapeutic drugs are not selective and they are able to exert their effects on any type of cell. This brings the major drawback of chemotherapy as it can the effect both the healthy and cancer cells. Cancer cells are fast-growing cells and require a high concentration of nutrients to support their growth. Therefore, chemotherapeutic drugs are injected to target the cancer cells without a functioning targeting mechanism, but based on pharmacokinetics and probability of the drug reaching the cancer cells. This lack of targeting efficiency leads to toxic side effects of chemotherapy, as fast-growing cells in hair, the intestinal, and the mouth are vigorously impacted by the drugs as they share a similar characteristic as the cancer cells. The type of drug and the dosage control are the current methods of minimizing the side effects of chemotherapy. Without absolute control of the drug, the tumour is exposed to inconsistent dosages of the drug. This allows cancer cells to gain drug-resistant capability resulting in higher dosage or altering the type of drug used. As mentioned, each time the drug is injected into the patient, healthy cells are heavily impacted and reducing the dosage to mitigate side effects leads to a long treatment option, potentially allowing the tumour to become drug-resistant. Thus, an effort to find a chemotherapeutic agent that is highly efficient yet minimizes the side effects must be made.

### **1.2.3. Other Treatment Options and Combinations of Treatments**

The surgery and chemotherapy for cancer have a major drawback of being invasive and exerting multiple side effects. To overcome these challenges, diverse treatment options are more actively becoming available due to success in research. Radiation therapy, immunotherapy, photodynamic therapy, hormone therapy, targeted therapy, blood stem cell transplant, biomarker testing for cancer treatment, cryoablation, and bone marrow transplants are different types of therapy that have

been developed and implemented in hospitals<sup>48-50</sup>. The type of cancer, stage of cancer, patient status, medical history, and financial status are part of the considerations for an oncologist in selecting the type of treatment. An oncologist may also implement a combination therapy which includes two or more types of therapy as a treatment. The most common combined therapies are the use of two different types of chemotherapeutic drugs, chemotherapy and immunotherapy, and chemotherapy and radiation therapy<sup>51,52</sup>. The rationale behind combination therapy is to increase the effectiveness of the treatment while reducing the toxicity of the drug. Immunotherapy has been one of the most used treatments for combination therapy with chemotherapy, as immunotherapy can change the tumour microenvironment and promote or suppress different immune systems to reduce the side effects and increase the effectiveness of the drug<sup>53</sup>. Yet, the challenges of combined therapy remain. First and most importantly, due to different combinations and dosages available, mass research and trials must be performed to find the optimal combination and dosage. Due to such probability, time, research, and funding remain to be fulfilled. Second, immunotherapy remains a relatively new field in oncology compared to the surgery or chemotherapy<sup>54</sup>. Thus, there are several limitations due to the lack of research and data obtained, which must be researched to ensure its effectiveness as well as its safety<sup>55</sup>.

As a result, an improvement must be made in the treatment options that is highly efficient in targeting the tumours by reducing the off-targeting effects and toxicity to the healthy cells.

### **1.3. Drug Delivery System**

With significant drawbacks from the current chemotherapeutic drugs, the targeted drug delivery system has been under a fast-growing field of research<sup>56</sup>. The targeted drug delivery system aims to specifically target the cancer cells while reducing their interaction with healthy cells and reducing side effects linked to the treatment. Research has been underway to classify specific proteins, receptors, and biomarkers to specifically target cancer cells using a ‘smart’ drug delivery system incorporated with nanoparticles.

#### **1.3.1. Nanoparticles**

With the discovery of nanoparticles, potential applications in medical research have been actively pursued. Nanoparticles are molecules that form a structure between 1 – 100 nm<sup>57</sup>. The U.S Food and Drug Administration (FDA) classifies medicinal products or drugs that are manufactured in this size as nanomedicine. Nanomedicine brings a unique advantage due to its size and engineering capability. *Figure 2* depicts examples of different nanoparticles that are used as nanomedicine, including liposomes, polymer nanoparticles, antibody conjugation with drug, dendrimer, micelle, quantum dots, and virus vectors have been previously studied and several studies have proven their effectiveness and are

underway in clinical trials<sup>58</sup>. Drugs are conjugated with biological nanoparticles such as antibodies or biological molecules to specifically target cancer cells<sup>59</sup>. Drugs can also be loaded onto polymer nanoparticles or micelles. It should be noted that encapsulation of nanoparticles is not limited to chemotherapeutic drugs but other compounds or molecules such as mRNA or a radioactive isotope<sup>59</sup>. The encapsulation of the drug is one of the key advantages of nanoparticles, as the same polymer or liposomes can be used to target different cells by simply replacing the conjugated biomolecule used to target the cancer cell. Furthermore, with a well-developed system, different types of compounds can be loaded onto the system for different purposes. Different chemotherapeutic drugs, radioactive tracers, and radioactive materials for internal radiation therapy can be loaded onto the system and delivered to different targeting tumour cells.

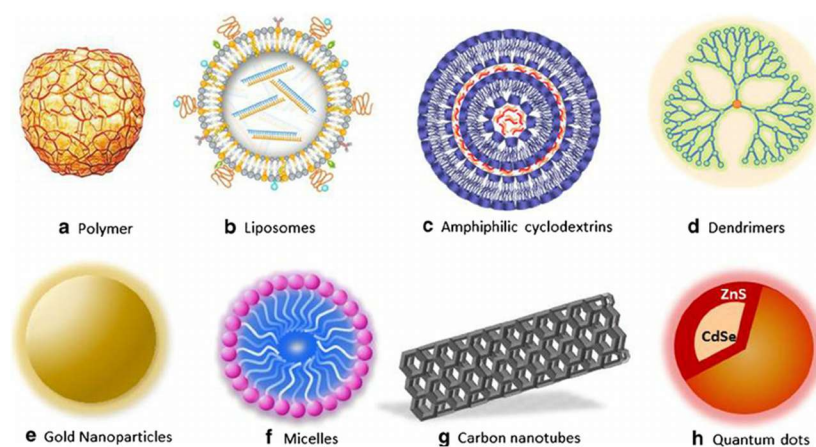


Figure 2. Different types of nanoparticles are used as nanomedicine.

(Reproduced from Ref <sup>60</sup>)

### 1.3.2. Poly (styrene-*alt*-maleic acid)

Among the various types of carriers developed recently, one presents a specific advantage when it comes to the functionality and potential application in treatment and diagnosis. Poly (styrene-*alt*-maleic anhydride) is a polymer composed of styrene and maleic anhydride, which becomes poly (styrene-*alt*-maleic acid) (PSMA) when the anhydride rings open up to form two carboxylic groups through hydrolysis. The polymer is an alternating co-polymer in which the hydrophobic groups (styrene) and hydrophilic groups (maleic anhydride) alternates along the chain allowing a very uniform interaction and mimicking biological systems. The hydrophilic group of the polymer is due to maleic acids that is pH-dependent, and the hydrophobicity from the styrene ring. This combination allows PSMA to become a self-assembling amphiphilic copolymer that is dependent on the pH. PSMA brings unique and interesting chemical properties as it is able to self-assemble at neutral pH

into two different shapes depending on its molecular weight. Previous studies found that PSMA at 20 kDa forms a cylindrical nanotube while 350 kDa forms a rectangular sheet as depicted in *Figure 3*<sup>61</sup>. After the polymer self-assembles, the polymer forms an inner hydrophobic cavity from the styrene rings with a hydrophilic outer layer from the maleic acids. The polymer has a 2.8 nm inner and 4.0 nm outer radius, with the hydrodynamic radius changing from ~100 nm at pH 7 and a few nm at pH 3. The self-assembly is an energy-efficient process as it is a resultant structure of the optimization to its lowest energy state. Interestingly, even with different molecular weights, the cavities formed by the self-assembly process have identical chemical properties. Using the amphiphilic characteristics, encapsulation or conjugation can be achieved with the polymer. A hydrophobic compound can be encapsulated into the inner hydrophobic cavity of the polymer and transported protected, while the hydrophilic outer core can be conjugated with an organic or biological molecule for targeting specific receptors<sup>62</sup>. This brings unlimited possibilities and advantages to the drug delivery system as PSMA is fully biocompatible, and different drugs and biological molecules could be used for different targeting mechanisms.

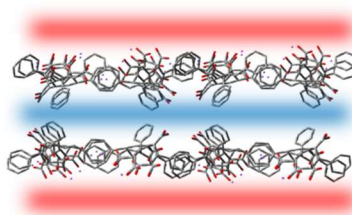


Figure 3. Self-Assembly of 350 kDa PSMA into sheets with hydrophobic inner core represented as blue and hydrophilic outer core represented as red

(Reproduced from Ref<sup>63</sup>)

### 1.3.3. Encapsulation – Hydrophobic Molecules

The PSMA can be utilized to encapsulate different types of payloads into the polymer. Various chemotherapeutic drugs or radioactive tracers can be encapsulated into the polymer. Previous experiments have demonstrated the possibility of encapsulating the hydrophobic drug, curcumin and its efficiency *in vitro*<sup>63,64</sup>. Thus, different hydrophobic chemotherapeutic drugs could be encapsulated into the polymer to treat cancer. As previously described, the hydrophobic inner core protects the drug from releasing into healthy cells before it reaches the tumour by maintaining its self-assembly. The cancer cells have an acidic extracellular environment, which fits perfectly with the polymer's self-assembly capability as the drug would only be allowed release from the tumour when it reaches the tumour due to decrease in pH. The healthy cells do not possess an acidic extracellular environment, allowing the polymer to maintain its assembly and protect



the drug<sup>65</sup>. This is highly advantageous in contrast to current chemotherapy system as it limits the adverse side effects as the polymer would only be able to release the drug once it reaches the acidic tumour environment.

## 1.4. Radioactive Tracers

In addition to chemotherapeutic drugs, different radioactive isotopes chelated with a hydrophobic compound can be encapsulated into the polymeric system. In general, three types of radiation are used in treatment and diagnosis: alpha particles, beta particles, and gamma rays<sup>66</sup>. Alpha particles consist of two protons and two neutrons, making them the heaviest and highest in ionizing radiation, with the lowest penetration. Beta particles can be either  $\beta^-$ , a high-speed electron or  $\beta^+$ , a positron. Beta particles' ionizing radiation and penetration ability lie between alpha particles and gamma rays. Gamma rays are high-energy electromagnetic radiation with high penetration ability with low ionizing radiation<sup>66</sup>. The high ionisation ability of alpha and beta particles makes them suitable for radiation treatment, while gamma rays serve as an excellent diagnostic agent using single photon emission computed tomography (SPECT). SPECT imaging is combination of conventional computed tomography, CT with addition of its ability to detect  $\gamma$ -rays emitted from radioactive isotopes. The detected  $\gamma$ -rays are While  $\beta^-$  is only used for treatment,  $\beta^+$ , a positron, can be used as a diagnostic agent using positron emission tomography (PET). A specific radioactive tracer can be selected depending on the emission energy, decay time, its chemical composition, and the availability of the radioactive tracer<sup>67</sup>.

### 1.4.1. <sup>111</sup>Indium

<sup>111</sup>Indium is a radioactive isotope synthetically produced by proton irradiation of <sup>112</sup>Cadmium (p,2n) in a cyclotron. As depicted in *Figure 4*, <sup>111</sup>In decays into stable <sup>111</sup>Cd through electron capture with a half-life of 2.80 days. The electron capture of <sup>111</sup>In transitions into excited <sup>111</sup>Cd with a spin state of  $+\frac{7}{2}$  which decays to  $+\frac{1}{2}$  through gamma-ray decay<sup>68</sup>. The emission of gamma rays allows the utilization of SPECT, which can perform a CT scan to generate a 3D scan of a person's body. One of the radioactive isotopes used for such a scan is <sup>111</sup>In as the highest energy of the gamma photon is 245 keV requiring only the tenth value layer is only 3mm<sup>69</sup>. The tenth value layer is where the radiation is reduced by one-tenth. With a reasonable decay time, radiation energy, and commercial availability, <sup>111</sup>In has been one of the popular radioactive isotopes in research for radioligand labelling for targeted cancer diagnosis<sup>70</sup>.

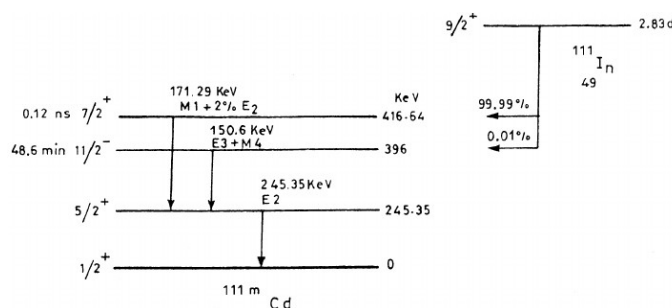


Figure 4. Decay Diagram of  $^{111}\text{In}$  with spins and energies of different excitation levels

(Reproduced from Ref <sup>71</sup>)

#### 1.4.2. $^{111}\text{In}$ -Oxyquinoline (Oxine)

One of the functional compounds of  $^{111}\text{In}$  is  $^{111}\text{In}$ -oxyquinoline (oxine), where the oxine acts as a metal chelator to form an octahedral shape with the  $^{111}\text{In}$  metal as a 1:3 complex. The oxine, oxyquinoline is a heterocyclic phenol group with a pyridine ring with the hydroxy and the nitrogen group are able to form a chelation bond with a metal as seen in *Figure 5*. This oxine poses a strong hydrophobicity due to its heterocyclic group that surrounds the metal. Thus, the oxine chelator  $^{111}\text{In}$  becomes a very hydrophobic compound that could be encapsulated inside the polymer. Currently, the  $^{111}\text{In}$ -Oxine is used as a diagnostic radiopharmaceutical for radiolabeling autologous leukocytes, which has been approved by the FDA as seen in *Figure 6* where radiolabeled leukocytes can be seen accumulating in the infected area of the patient<sup>72</sup>. The FDA approval indicates effectiveness and the safety of  $^{111}\text{In}$ -Oxine inside the body.

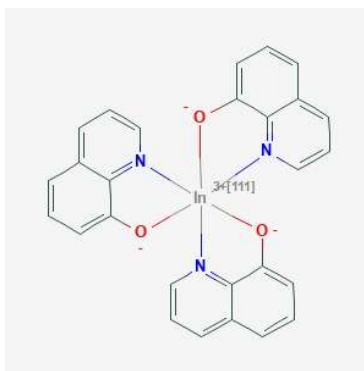


Figure 5. Chemical structure of  $^{111}\text{In}$ Indium Oxine. Three Oxine chelated to  $^{111}\text{In}$

(Reproduced from Ref <sup>73</sup>)



Figure 6. Image of  $^{111}\text{In}$ -labeled leukocyte accumulation in the infected prosthetic vascular graft in the right thigh (arrowheads)

(Reproduced from Ref<sup>74</sup>)

## 1.5. Direct targeting Strategy

### 1.5.1. Folic Acid (FA)

To target  $\text{FR}\alpha$ , a folic acid, FA must be used for active targeted drug delivery. Folate is a general term often referred to as vitamin  $\text{B}_9$ , and FA is the most commonly used for vitamin supplements or folate-rich food<sup>75</sup>. The structure of the FA is comprised of a 2-amino-4-hydroxy-pteridine ring, p-aminobenzoic acid, and glutamic acid. The three compounds are conjugated via peptide bonds, and the carboxylic groups of glutamic acid at the end of the FA can be conjugated with different linkers or chelators as seen in *Figure 7*. FA plays a key role in the prevention of neural tube defects during embryogenesis, which is crucial in forming the brain and spine of a fetus during the early stage of pregnancy<sup>76</sup>. Furthermore, FA is needed in the folate cycle of the cell which is important in DNA synthesis. Thus, folate deficiency is often found during pregnancy and folate uptake is critical for mothers during pregnancy for healthy fetal growth<sup>77</sup>. This signifies the importance of FA during the proliferation of the cells. FA within the body plays a key role in one-carbon metabolism often referred to as the folate cycle. The pre-folate cycle begins from FA reduction to dihydrofolate (DHF) via dihydrofolate reductase, and reduced further into tetrahydrofolate (THF), which is the only biologically active form of FA in the body<sup>78</sup>. Formation of THF begins the folate cycle, reacting with the catalyst enzyme serine hydroxymethyltransferase (SHMT), resulting 5,10-methylene-THF (5,10-me-THF) and glycine as a by-product. 5,10-me-THF is reduced by methylenetetrahydrofolate reductase (MTHFR) using vitamin B2 as a

cofactor to produce 5-methyltetrahydrofolate (5-mTHF). 5-mTHF initiates the methionine cycle catalyzed by methionine synthase (MS) and vitamin B12 as cofactors, resulting in methionine. Methionine is reacted with adenosine by methionine adenosyl transferase 2A to produce s-adenosyl methionine, which plays a critical role in DNA methylation, as seen in *Figure 8*. This DNA methylation process and part of DNA synthesis explain the crucial role of folic acid during the proliferation of cells and fetal neural tube development and without FA, this cycle can't be initiated. Previous studies have found the inhibition of the cell cycle and a decrease in cell proliferation with folate deficiency<sup>79,80</sup>. Thus, the overexpression of FR $\alpha$  in malignant tumours could be explained due to the important proliferation role of FA in the cell as observed with increase number in FR $\alpha$  on the surface of cancerous cells. With such importance and demand from the tumour cells, FA becomes an excellent compound to be used for targeted drug delivery systems.

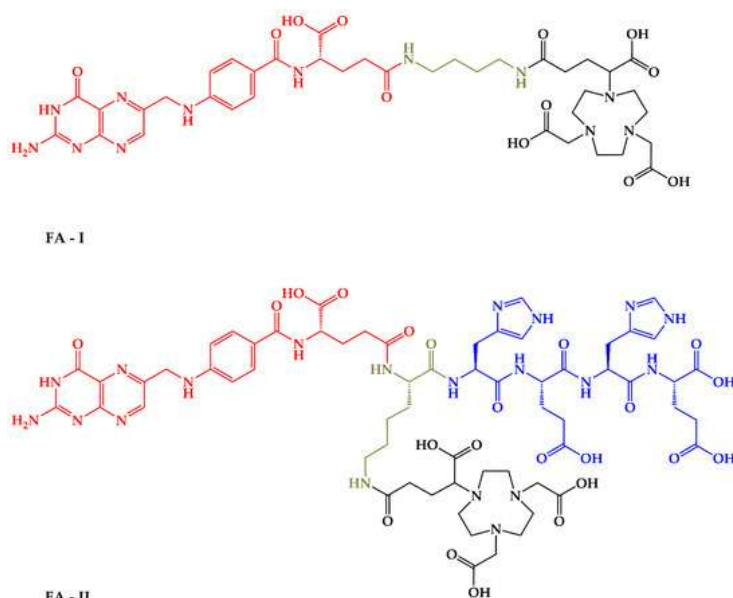


Figure 7. Different conjugation of functional compounds and chelator on FA

(Reproduced from Ref<sup>81</sup>)

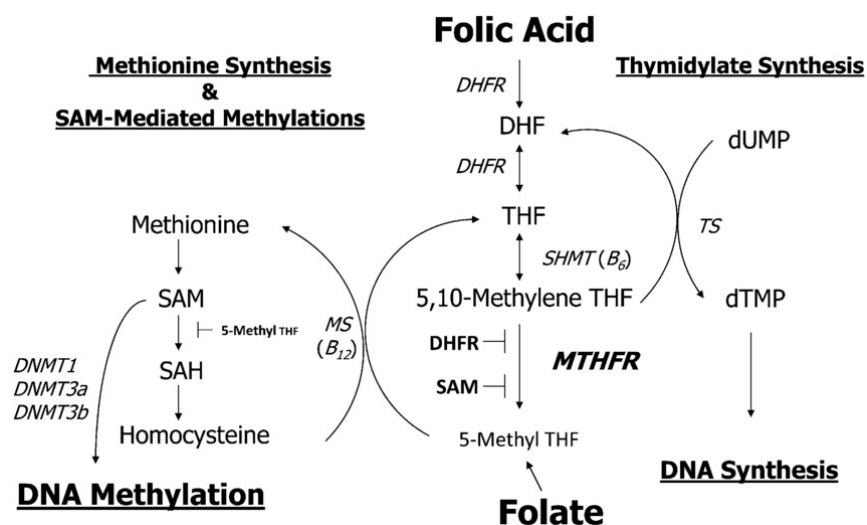


Figure 8. Folate cycle and methionine cycle. Folic acid acts as a starting compound to initiate the cycle which leads to DNA synthesis.

(Reproduced from Ref <sup>(82)</sup>)

### 1.5.2. Folic Acid Receptor Alpha (FR $\alpha$ )

For a successful and efficient targeted drug delivery, a target must be present solely on the tumour cells. Exclusive expression on the tumour cells leads to reduced off-targeting to the healthy cells which ultimately results in decreased side effects. The folic acid receptor alpha (FR $\alpha$ ) is an excellent target for targeted drug delivery systems as the expression level is doubled in ovarian, lung, brain, head and neck, renal cell, breast, and pancreatic cancers<sup>83,84</sup>. Normal cells require folic acid however, the receptors are located in apical portions of the cells, therefore, it is difficult for FA to bind to the receptors while circulating in the blood system<sup>85</sup>. In contrast, due to the microenvironment tumour cells form, the tumour has direct access to the blood system, allowing more accessibility of FA. The FR $\alpha$  is one of the three isomeric forms, the FR in the body that function for cellular folic acid intake<sup>86</sup>. FR $\alpha$  is a glycosylphosphatidylinositol (GPI) - anchored glycoprotein with a high affinity ( $K_d = 0.4$  nmol/L) for folate protein<sup>87,88</sup>. The process of FA endocytosis can be seen in *Figure 9* where the GPI-anchor allows the receptor to wave on the surface of the cell and seek for FA to bind with and enter the cell through endocytosis once the binding occurs. After FA is internalized into the cell, the pH drops to around 5.5 in the lysosome which initiates release of FA from the receptor<sup>89</sup>. After the separation, the FR $\alpha$  is recycled to the surface of the cell. Another key function of the FR $\alpha$  is its function as a DNA transcription factor, binding with cis-regulatory elements in the nucleus and activating transcription genes including *HES1*, *FGFR4*, and *Oct4*<sup>90,91</sup>. *Oct4* activation is important as it interacts with STAT3 and Myc, which are important transcriptional genes that regulate the proliferation of the cell<sup>92</sup>.

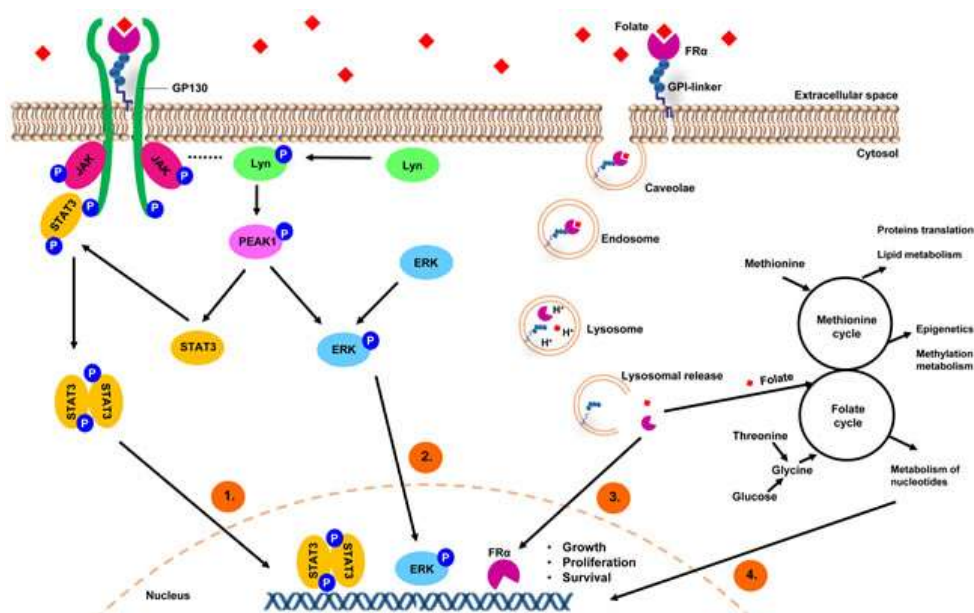


Figure 9. Pathway of FR $\alpha$  in the cell after endocytosis or binds with GP130

(reproduce from ref <sup>93</sup>)

Chen and his group crystallized FR $\alpha$  with FA inside the binding pocket of the receptor. They reported the amino acids of the receptor that interact with FA via hydrogen bonds and amino acids that have hydrophobic interactions with FA<sup>94</sup>. *Figure 10* highlights the amino acids in the receptor that interact with the FA. *Figure 11* displays the mutated amino acid and its impact on the binding affinity between specific amino acids and the FA<sup>94</sup>. The group was also able to generate a charge distribution surface of FR $\alpha$  including the inner binding dock, which can be seen in *Figure 12*. It should be highlighted that the outer surface of the binding pocket is positively charged, at +3 eV, while the inner binding is negatively charged at -3 eV.

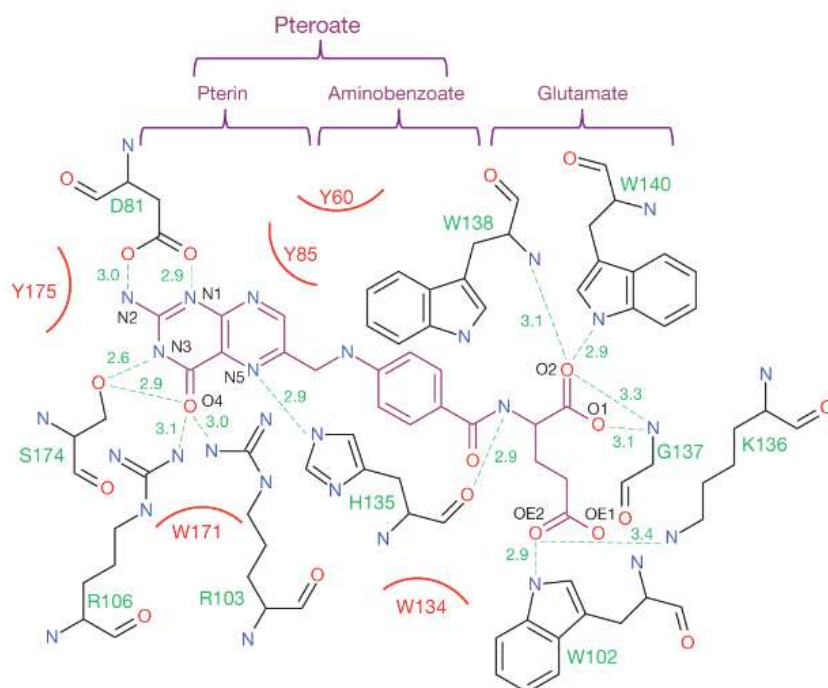


Figure 10. Cross-section of FRA with docked FA displaying hydrogen bonds in green dotted line and hydrophobic interaction in red line

(Reproduce from Ref<sup>94</sup>)

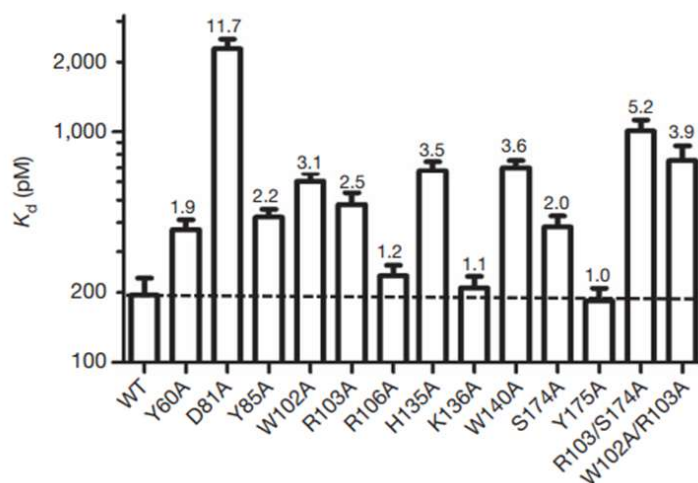


Figure 11. Binding Energy Kd between different amino acids in the receptor and FA

(Reproduced from Ref<sup>94</sup>)

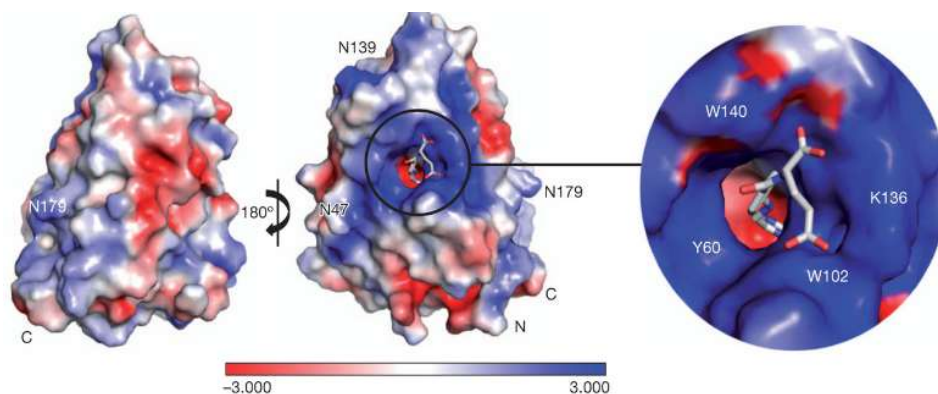


Figure 12. Charge distribution of FR $\alpha$  on -3 eV to +3 eV electrostatic scale

(Reproduced from Ref <sup>94</sup>)

### 1.5.3. Polymeric Targeted Carrier

With the hydrophobic compound encapsulation capability of the polymer and unique over-expression of FR $\alpha$  in the tumour cells, conjugation of FA with PSMA is a novel nanoparticle synthesized for targeted drug delivery. However, the polymer backbone must be able to maintain its linearity despite addition of a compound. The disruption to its hydrogen bonding would interfere with the ability to self-assemble into its respectable shape in accordance with its molecular weight, prohibiting encapsulation of a hydrophobic compound. If the FA is attached directly to the PSMA, the cross-linking occurs between the carboxylic groups of the polymer and the pterin ring of the FA can disrupt the self-assembly of the polymer. To overcome this challenge, previous study has tested various biocompatible linkers and concluded that the 2,4-diaminobutyric acid (DABA) is an appropriate linker to conjugate FA and PSMA<sup>62</sup>. The resulting product is FA-DABA-PSMA and it is fully biocompatible and safe for the body. The FA-DABA compound was attached to every 10 monomers of the polymer to maintain the polymer's self-assembly structure but to maximize the probability of the complex binding with the receptor. *Figure 13* displays the synthesis pathway of FA-DABA-PSMA regardless of the polymer's molecular weight. The assembled FA-DABA-PSMA becomes the target drug delivery system as it is able to encapsulate hydrophobic drugs into the polymer and carry them until it is released due to the acidic tumour microenvironment as depicted in *Figure 14*. To verify this hypothesis, the synthesized FA-DABA-PSMA was tested *in vitro* using MDA-MB-231 triple-negative breast, PANC-1 pancreatic, and DU-145 Prostate cancer to test its functionality and efficiency<sup>63,64,95</sup>. The experiments found that cell viability decreased with empty FA-DABA-PSMA and with curcumin, 5-FU, and paclitaxel encapsulated. To add to this novel finding, the 20 kDa and 350 kDa PSMA had different results. The 350 kDa PSMA was able to disrupt the oncogenes such as p53, STAT-3, and c-Myc of the cell as it was able to penetrate through to the nucleus, while 20 kDa didn't remain in the cytoplasm of the



cell<sup>95</sup>. From this study, the importance of size and the structure of the polymer in decreasing the cell viability became a factor for consideration. Interestingly, recent study found an increase in internalization of the functionalized polymers when different lectins were used *in vitro*<sup>96</sup>. This internalization contradicts the initial expectation of the study, as lectins are commonly used to reduce the internalization of drugs.

The decrease in cell viability by the empty FA-DABA-PSMA could be potentially due to the strong binding of FR $\alpha$  with FA. As previously mentioned, the FR $\alpha$  plays an important role as a DNA transcriptional factor, and the inability of the FR $\alpha$  to release the FA could explain the decrease in cell viability as it can't function as a transcriptional factor. However, the exact mechanism behind this finding is yet to be proven. Based on previous results, the FA-DABA-PSMA complex could be used as a targeted drug delivery system and be loaded with different types of hydrophobic chemotherapeutic or radioactive agents for direct targeting therapy. To further note, the FDA has recently approved mirvetuximab soravtansine-gynx, which is a nanomedicine that targets FR $\alpha$  using an antibody<sup>97,98</sup>. Thus, nanomedicine targeting FR $\alpha$  has a promising future for targeted drug delivery.

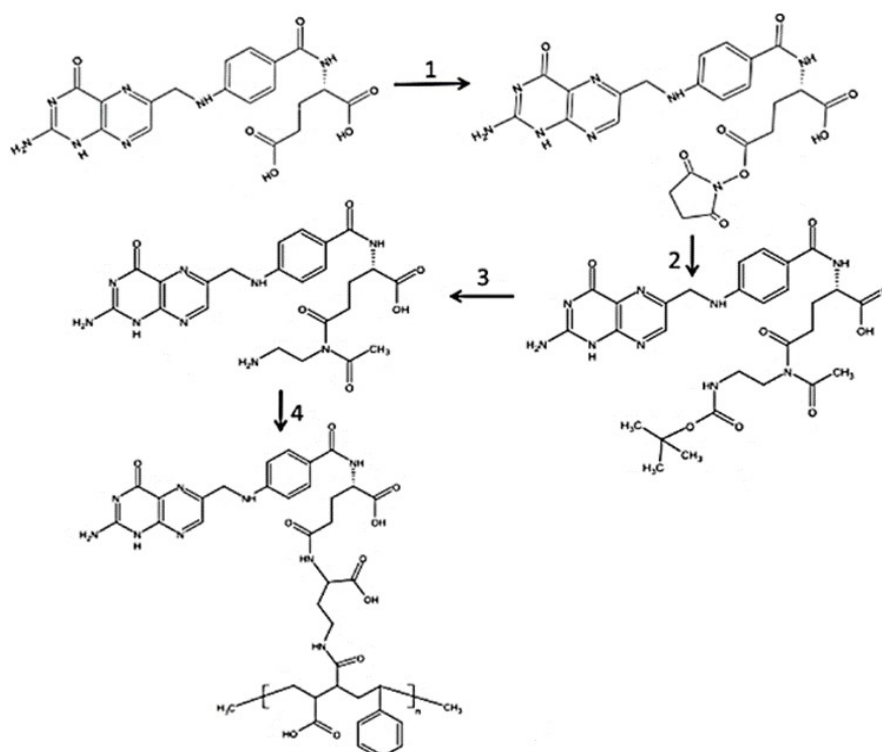


Figure 13. Synthesis pathway of FA-DABA-PSMA. FA is linked with linker 2,4 – diamino butyric acid before PSMA is added.

(Reproduced from Ref<sup>62</sup>)

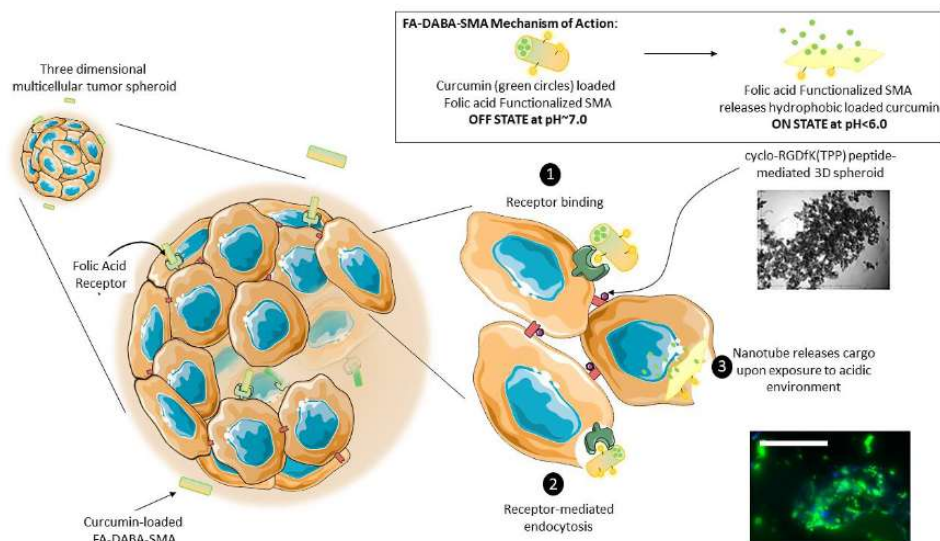


Figure 14. Mechanism of action of FA-DABA-PSMA targeting

(Reproduced from Ref <sup>95</sup>)

## 1.6. Research Objective

Previous studies have proven the capability of the functionalized FA-DABA-PSMA system to provide an effective vehicle for cancer treatment. As discussed, the mechanism of FA-DABA-PSMA reducing cell viability needs to be explained. The  $FR\alpha$  may be poisoned due to the FA-DABA-PSMA, and this poisoning could be explained by analyzing the binding energy. The primary purpose of this study is to investigate the effect polymeric carriers have on binding energy with  $FR\alpha$  and its capability to encapsulate Indium-Oxine, a hydrophobic diagnostic radiopharmaceutical that can be used for diagnosis.

Chapter two will discuss the various theoretical backgrounds of the methods used to explore to calculate the binding energy between FA, FA-DABA-PSMA, and  $FR\alpha$ . This will include optimization of the FA with  $FR\alpha$  and FA-DABA-PSMA with  $FR\alpha$  structures using Gaussian software. The optimization will be performed using different computational chemistry methods, including AMBER for field in molecular mechanics, PM6 in semi-empirical methods, and 3-21G and 6-31G\*\* in density functional theory (DFT).

Chapter three will discuss microscale thermophoresis (MST), an experimental method used to determine the binding energy between the polymeric carrier and  $FR\alpha$ . Next, the methods used for characterizing the encapsulation of the

In-Oxine, fluorescence spectroscopy, neutron activation and thin layer chromatography will be discussed.

Chapter four will discuss the results of the computational optimization. This will include the interaction and binding energy between FA-FR $\alpha$  and FA-DABA-PSMA-FR $\alpha$  calculated by setting FA, FA-DABA-PSMA and the amino acids of the receptor that interact with the ligand to 3-21G and 6-31G\*\* in DFT and the rest of the amino acids as AMBER using MM. The simulation will be performed at pH 7.4 to simulate the binding occurring at the surface of the cells and pH 5.5 to simulate the release of the ligand in the lysosome of the cell after endocytosis. The chapter will also break down the movement of amino acids corresponding to the change due to the difference in ligands.

While the simulations are calculated in a perfect setting without any interferences from other compounds such as water, performing an experimental test is an excellent way to compare with the computational simulation. Chapter five will discuss the results obtained experimentally through MST. The binding affinity obtained will be discussed and compared to the results from the computational simulation. Through comparison analysis, the effect of FA-DABA-PSMA 350 kDa and 20 kDa on FR $\alpha$  will be discussed.

Chapter six will be shifting towards encapsulation of the Indium-Oxine, a hydrophobic radiopharmaceutical that is used as a diagnostic agent. With FA-DABA-PSMA showing promising results in targeting treatment, encapsulation can lead to determining the pharmacokinetics of FA-DABA-PSMA *in vivo*. To determine the encapsulation of the drug inside the hydrophobic pocket, results from fluorescence spectroscopy, neutron activation, and thin-layer chromatography will be discussed to determine the encapsulation of the In-Oxine inside the polymer.

Chapter seven will conclude with the findings from this study and future remarks. The results and conclusions from all chapters will be summarized and future outlook, a possibility of FA-DABA-PSMA used as diagnostic or theragnostic agent will be discussed.

## 2. Methods

It is a challenge to examine and understand how the functionalized polymer is reacting with the cells and resulting decrease in cell viability. Out of a few hypotheses, the inability of FR $\alpha$  to release FA due to a very strong binding energy could be the cause of the success of the targeted approach. To determine the validity of the hypotheses, without an experimental procedure is to calculate the binding energy through computational chemistry. Computational chemistry can optimize the structure and the energy of the receptor and the functionalized polymer to estimate the binding energy between FA, FA-DABA-PSMA and FR $\alpha$ .

Computational chemistry describes and calculates the electron configuration of an atom using mathematical functions. This is beneficial for chemists interested in energy and structures of the compound that are difficult to obtain through experiments. There are 3 major approaches to describing the electronic structures in computational chemistry: *ab initio* and semi-empirical and molecular mechanics (MM). *Ab initio* is based on theoretical calculations and solves the Schrödinger equation without any experimental data while the semi empirical methods use data applied from experiments. Two types of *ab initio* methods, Hartree-Fock (HF), density functional theory (DFT), are commonly used for calculation. In addition, the fundamentals of MM will be discussed.

### 2.1. Basic Quantum Theory

The birth of quantum and computational chemistry began with the discovery of Max Planck's quantization of energy in 1901.

$$E = h\nu \quad (1)$$

Where  $E$  represents energy  $\nu$  is the frequency of light and  $h$  represents Planck's constant. The equation was formed initially for blackbody radiation however, this idea where energy could be quantized would later be applied as one of the most critical parts of Albert Einstein's photoelectric effect. The photoelectric effect recognized the light energy, photons to be treated as a particle. This would lead to the discovery of a critical relationship between the mass of the photon and the energy.

$$E = mc^2 \quad (2)$$

The combination of Planck's and Einstein's equations would result:

$$\lambda = \frac{h}{mc} \quad (3)$$

Where  $\lambda$  is the wavelength inversely proportional to the mass. 20 years later, Louis de Broglie proposed that electrons possess the properties of particles and waves. He added that this is only true when the particle doesn't travel in the speed of a light<sup>99</sup>.

$$\lambda = \frac{h}{mv} = \frac{h}{p} \quad (4)$$

Where  $v$  is the velocity of the particle. This equation could be simplified as the momentum of the particle. Thus, the wavelength is inversely proportional to the speed of the particle; an increase in speed results in a shorter wavelength. Given the velocity, a sum of energies,  $E$ , can be added by summing the kinetic,  $K$  and potential energy,  $V$ .

$$\lambda = \frac{h}{\sqrt{2m(E - V)}} \quad (5)$$

Given  $E$ , it can be isolated to fit the classical time-independent wave equation and solve time-independent Schrödinger's equation<sup>100</sup>:

$$\frac{\partial^2 \Psi}{\partial x^2} + \frac{8\pi^2 m}{h^2} (E - V) \Psi = 0 \quad (6)$$

This can be reduced to a simpler equation using a Hamiltonian operator to represent the energy operator and energy eigenvalue. The simplification of the equation is feasible due to Born-Oppenheimer's approximation<sup>101</sup>. It states that nuclei and electron wavefunctions are independent of each other as the electronic orbitals are able to adapt instantly following a nuclear movement; thus, the nuclei can be treated as static and negligible in the energy calculation:

$$\hat{H}\Psi = E\Psi \quad (7)$$

The  $\Psi$ , is a sum of  $\Psi(x_n)$  where  $x_n$  represents the spin coordinate  $(\pm \frac{1}{2}) s_i$  and spin-orbital space  $r_i$ . The Hamiltonian is a sum of the kinetic energy of the electrons, the potential field created by the nuclei and inter-electron repulsion energy.

$$\hat{H} = \sum_i^{electrons} \frac{-\nabla_i^2}{2} + \sum_i^{electrons} \sum_A^{nuclei} \frac{-Z_A}{r_{iA}} + \sum_{i>j}^{electrons} \frac{1}{r_{ij}} \quad (8)$$

It should be noted that in the summation of the potential field, the radius of the nucleus is proportional to the charge of the atom,  $Z$ .

## 2.2. Wavefunction Approximation

From the Born-Oppenheimer approximation, systems that were bigger than hydrogen systems were unsolvable. However, in 1926, Max Born formed Born's rule, which solved the Schrödinger's equation through a different approach. While Schrödinger argued that the amplitude of the wavefunction corresponds to the density of the particle at a specific point; Born argued that the amplitude corresponds to the probability of finding the particle. It was quickly found that the square function of the wavefunction,  $|\Psi|^2$  was able to generate the probability needed<sup>102</sup>.

This argument not only solved the Schrödinger's equation but it unlocked the potential to describe any system by a linear combination of different wavelengths. Furthermore, with this rule, only optimization of the wave function needs to be made.

## 2.3. Basis Sets

To describe the probability of finding an electron, a linear combination of one electron function within atomic orbitals needs to be combined. These combined functions are called basis functions. The first basis functions used were called Slater-type orbital (STO) basis functions, described as<sup>103</sup>:

$$STO = Nr^{n-1}e^{-\zeta r} \quad (9)$$

Where  $N$ , is the normalizing constant,  $n$ , is a principal quantum number,  $\zeta$ , is the effective charge of the nucleus, and  $r$ , is radius of the electron from the nucleus. The STOs successfully describe hydrogen like systems yet, a cusp formed  $r = 0$ , and exponential decay as  $r$  increases. Basis sets are combination integral evaluation of each electron in a molecular orbital system. Thus, STO becomes limited for atoms with multiple electrons within its orbital as it becomes computationally expensive to evaluate.

A second basis set in contrast to STO is called Gaussian type orbitals (GTOs), where it forms a Gaussian distribution curve. The GTOs eases the difficulty in mathematical computation, allowing for multi electron systems to be available for computation<sup>104</sup>.

$$GTO = Nr^{n-1}e^{-\zeta r^2} \quad (10)$$

To maximize the usage of the GTOs, a linear combination of atomic orbitals (LCAO) must be implied. Combining the Gaussian orbitals allows a basis set function,  $\varphi_\mu$  can be formed using such an equation:

$$\varphi_\mu = \sum_s d_{\mu s} g_s \quad (11)$$

With the basis set function of the multiple electron wavelength summed, an atomic orbital,  $\phi_n$  can be built to accurately describe the atomic orbital or multi-electron system.

$$\phi_n = \sum_{\mu} j_{n\mu} \varphi_{\mu} \quad (12)$$

Where  $j_{n\mu}$  is a coefficient of  $\mu$  of basis function  $\varphi_{\mu}$ , which is described using GTO. Now, the atomic orbital  $\phi_n$ , can be linearly combined to find the molecular orbital  $\psi$ , by applying the molecular orbital (MO) theory.

$$\psi_k = \sum_n c_{kn} \phi_n \quad (13)$$

Where  $c_{kn}$  is the molecular orbital expansion coefficient. Similar to probability of finding an electron using a wavefunction, squaring molecular orbital represents the probability of finding electrons in a location given the nuclei is stationary.

With the method and functionals defined for a calculation, last but most importantly, the basis sets have to be appropriately selected. In our study, 32-1G and 6-31G\*\* were selected for the density functional theory simulations.

### 2.3.1. 3-21G

Earlier, the fundamental basics of the basis sets were discussed. Among multiple types of basis sets currently used, Pople's basis sets, a split-valence basis sets, are among the popular basis sets used for first to fourth-row elements. The notation is written as:

$$X - YZg \quad (14)$$

Where  $X$  represents the number of primitive Gaussians as a single function that is used to present each atomic orbital,  $Y$  and  $Z$  represent the split basis set that represents the number of Gaussian functions used to describe smaller and larger orbitals. The 3-21G is the smallest double zeta basis set out of the Pople's basis sets. It contains three Gaussian primitives and splits the valence orbitals into two basis functions: two Gaussians for the contracted inner function and one Gaussian for the outer function. The 3-21G was used as an optimization tool to decrease the required computational time for 6-31G\*\*.

### 2.3.2. 6-31G\*\* (d,p)

The main drawback of the 3-21G is its inaccuracy and inability to correctly model contractions and diffusions of the atom. This is especially true for compounds that form hydrogen bonds as the Gaussian restrict the orbital of the hydrogen, an *s*-orbital from any movement. To correct this restriction, a polarized basis set can be employed to enhance the accuracy to another level. Polarized basis sets add a higher angular momentum number to the basis set to give flexibility to the atom. As mentioned, during hydrogen bonding, the hydrogen will not maintain a uniform spherical symmetry. With the addition of a higher angular momentum, *p*-orbital in this case, it would allow the orbitals to form non-spherical symmetry. It should be noted that the addition doesn't imply that the high levels will always be occupied. They exist to provide a more accurate flexibility of electron density when bonding occurs, generating a more accurate result. Together, this can be used with 6-31G, six Gaussian primitives, three contracted Gaussian basis functions for inner and one Gaussian for outer with polarized basis set, \*\* or (d,p). The \*\* and (d,p) can be used interchangeably, with *d* and *p* representing the d-type or p-type function that has been added to the basis set.

The basis sets provide the wavefunctions that describes the system. However, there is only one exact wavefunction that can describe the lowest energy system of the system. Thus, variational principle must be discussed to approximate the wavefunction of the system.

## 2.4. The Variational Principle

The objective of 3 equations linearly combining functions is to achieve 'optimization', which is often referred to as the ground state energy,  $E_0$  and ground state wavefunction,  $\Psi_0$ . However, it is impossible to achieve the ground state wavefunction or energy as approximations are made. Thus,  $E_k > E_0$  and by multiplying  $\Psi$  into eq (7), Schrödinger's equation, integrating, and solving the integration gives:

$$E[\psi_k] = \frac{\sum_k |c_k|^2 E_k}{\sum_k |c_k|^2} \quad (15)$$

There is only one wave function that describes the lowest energy possible. When the wavefunction,  $\Psi_k \neq \Psi_0$ , the energy resulting will be a less stable system with higher energy than the true ground state energies,  $E_k \geq E_0$ . From the equation above, every possible improvement is made to produce the lowest energy possible. Thus, the energy calculated is minimized until it reaches the lowest energy state possible, nearing the true ground state energy. It will be impossible to reach the true ground state energy however, with MO theory and variational method, energy closest to this state can be arbitrarily achieved.



## 2.5. Hartree Fock

The application of variation theory is Hartree Fock's theory. To determine the energy,  $E_k$ , the Hamiltonian operator to the molecular orbital must be applied. Multi multi-electron Hamiltonian operator must be approximated by the Fock operator, which is a one-electron Hamiltonian operator<sup>105</sup>.

$$F(i) = H^{core} + \sum_i (2J_i - K_i) = -\frac{1}{2}\nabla_i^2 - \frac{Z}{r_i} + \sum_i (2J_i - K_i) \quad (16)$$

Where  $H^{core}$  is the nuclear energy that contributes while  $J_i$ , is Coulomb, the potential operator and  $K_i$  is the exchange, kinetic operator. The Coulomb operator is the repulsion energy of each electron remaining in the field while the exchange operator a quantum effect for each electron pair<sup>105</sup>.

To calculate the orbital energy, the Fock operator can be used in the following equation by multiplying by the spin-orbital  $\psi_i$  to generate a Hartree Fock equation:

$$F(i)\psi_i = \varepsilon_i\psi_i \quad (17)$$

The addition of electron exchange energy significantly improves the representation of the Fock operator, which can be developed using the molecular orbitals in matrix form using Roothaan-Hall equations<sup>106,107</sup>:

$$\sum_{v=1}^N (F_{\mu v} - \varepsilon_i S_{\mu v}) c_{vi} = 0 \quad (18)$$

Where  $\mu = 1, 2, \dots, N$ .  $F_{\mu v}$  is an  $N \times N$  Fock matrix operator,  $\varepsilon_i$  is the energy of each spin-orbital,  $S_{\mu v}$  is an  $N \times N$  overlap matrix, and  $c_{vi}$  is a coefficient variation principle.

The Hartree Fock is capable of producing a solution that neglects electron correlation energy. As a result, it will always produce an energy that is higher than the true ground energy.

## 2.6. Density Functional Theory

Density functional theory (DFT) utilizes electron density to calculate the total energy of the system instead of a multi-electron wavefunction. The Thomas-Fermi model proposed a uniform distribution of electrons into small cubic volumes where the volume  $\Delta V$  contains  $\Delta N$  electrons in a space. Using the model led to an equation where electron density,  $\rho$  can be calculated by:

$$\rho = \frac{\Delta N}{\Delta V} \quad (19)$$

This equation can be further developed into a kinetic energy equation as a functional of electron density:

$$K_{TF}[\rho] = \frac{3}{10}(3\pi^2)^{\frac{2}{3}} \int \rho^{\frac{5}{3}}(\mathbf{r}) d\mathbf{r} \quad (20)$$

This kinetic energy can be applied to find the total energy of the system by adding nuclear-electron attraction potential and electron-electron repulsion:

$$E_{TF}[\rho] = K_{TF} - Z \int \frac{\rho(\mathbf{r})}{r} d\mathbf{r} + \frac{1}{2} \iint \frac{\rho(\mathbf{r}_1)\rho(\mathbf{r}_2)}{|\mathbf{r}_1 - \mathbf{r}_2|} d\mathbf{r}_1 d\mathbf{r}_2 \quad (21)$$

The Thomas-fermi model was a good foundation in the development of DFT and successfully modeled atomic energies when modified. However, at the molecular level, it couldn't account for chemical bonds, leading to a failure in modeling.

### 2.6.1. Hohenberg-Kohn Theory

After the development of the Thomas-fermi model, research and attempts to improve this model continued till 1964, when Hohenberg and Kohn took an alternate approach to understanding the relationship between electron density and the description of the system. Till this point, under Born-Oppenheimer's approximation, where the kinetic and electron interactions are minimized as they rearrange themselves to the unchanged position of the nucleus<sup>101</sup>. To tackle this problem, they proposed two theorems. The first theorem they proposed states as follows: the electron density uniquely determines the external potential<sup>108</sup>. With this statement, the Hamiltonian operator can now be determined by the electron density. This is possible as the electron density is able to provide the external potential and total number of electrons,  $N$  which can be computed by integration of the space of the electron density. As the Hamiltonian operator is determined, the wave function of all states in the density can be easily computed. This alone was a huge improvement in the DFT as electron density can single-handedly determine the charges and position of the nucleus.

The proof of the first method runs on *reductio ad absurdum* where external potential  $V_{\text{ext}}$  and  $V'_{\text{ext}}$  are different but result in the same electron density  $\rho(\vec{r})$ . The two external potentials are the only difference in the two Hamiltonian,  $\hat{H} = \hat{T} + \hat{V}_{ee} + \hat{V}_{\text{ext}}$  and  $\hat{H}' = \hat{T} + \hat{V}_{ee} + \hat{V}'_{\text{ext}}$  and these two Hamiltonians have two different ground state wavefunction  $\Psi$  and  $\Psi'$  that corresponds to two ground state energy  $E_0$

and  $E'_0$  where  $E_0 \neq E'_0$  while generating the same electron density. The ground state energy,  $E_0$  is defined as:

$$E_0 = \langle \Psi' | \hat{H} | \Psi' \rangle \quad (22)$$

By applying the variation principle previously mentioned,

$$E_0 < \langle \Psi' | \hat{H} | \Psi' \rangle = \langle \Psi' | \hat{H} | \Psi' \rangle + \langle \Psi' | \hat{H} - \hat{H}' | \Psi' \rangle \quad (23)$$

This equation can be expanded and simplified in terms of external potential:

$$E_0 < E'_0 + \int \rho(\vec{r}) \{V_{ext} - V'_{ext}\} d\vec{r} \quad (24)$$

Exchanging the primed quantities and repeating the steps results in the following equation:

$$E'_0 < E_0 - \int \rho(\vec{r}) \{V_{ext} - V'_{ext}\} d\vec{r} \quad (25)$$

Adding the two equations together results in inconsistent results:

$$E_0 + E'_0 < E'_0 + E_0, 0 < 0 \quad (26)$$

Through these equations, it can be concluded that two different  $V_{ext}$  that yield the same ground state cannot exist and must be within a constant. Thus, the energy of the density function contains information about the wave function. Furthermore, the density is sufficient enough to determine the kinetic energy,  $K$ , electron interaction energy  $U_{ee}$ , and external potential,  $V_{ext}$  and this equation is the central theorem in the DFT.

$$E[\rho] = K[\rho] + U_{ee}[\rho] + V_{ext}[\rho] \quad (27)$$

The second theorem incorporates the variational principle with the energy and states that the functional of the ground state energy delivers the lowest energy if the input density is the true ground state density,  $\rho_0$ . This can be described as such equation:

$$E_0 \leq E[\rho] = K[\rho] + U_{ee}[\rho] + V_{ext}[\rho] \quad (28)$$

With a condition where any trial density  $\rho(\vec{r})$ , satisfies the condition,  $\rho(\vec{r}) \geq 0$  and where  $N = \int \rho(\vec{r}) d\vec{r}$ . Furthermore, since the trial density can define its own Hamiltonian, it can define its wavefunction,  $\tilde{\Psi}$ . With the true external potential  $V_{ext}$ , a Hamiltonian can be generated and the wavefunction can be taken as a trial wavefunction, which results in:

$$\langle \tilde{\Psi} | \hat{H} | \tilde{\Psi} \rangle = K[\tilde{\rho}] + U_{ee}[\tilde{\rho}] + \int \tilde{\rho}(\vec{r}) V_{ext} d\vec{r} \quad (29)$$

This equation can be simplified to result in the final equation:

$$E[\tilde{\rho}] \geq E_0[\rho_0] = \langle \Psi_0 | \hat{H} | \Psi_0 \rangle \quad (30)$$

### 2.6.2. Kohn-Sham method

Previously, the approaches to achieving the lowest energy using the DFT involved solely modifying the density. However, the Kohn-Sham method approaches in solving the kinetic energy by distinguishing non-interacting electrons called Kohn-Sham determinants<sup>109</sup>. They also added electron interaction correction,  $E_{xc}$ . The overall energy can be described as such:

$$E[\rho] = T_s[\rho] + J_s[\rho] + E_{xc}[\rho] + \int \rho(\mathbf{r}) v(\mathbf{r}) d\mathbf{r} \quad (31)$$

where the kinetic energy,  $T_s[\rho]$  is expressed as the following:

$$T_s[\rho] = -\frac{1}{2} \sum_i^N \langle \psi_i | \nabla^2 | \psi_i \rangle \quad (32)$$

Note that the equation doesn't represent the true kinetic energy but the non-interacting electrons. In return, it can produce true ground state density using:

$$\rho(\mathbf{r}) = \sum_i^N |\psi_i|^2 \quad (33)$$

Where  $N$  represents the orbitals occupied by non-interacting electrons.

The  $J_s[\rho]$  is represents the non-interaction potential energy of the electrons. The  $E_{xc}$  plays a critical part as it accounts for the difference between the non-interacting kinetic (true) energy and classical electron-electron interaction energy. However, to correctly account for the difference, it requires the following equation, the Kohn-Sham equation, to find the best orbitals.

$$\left[ -\frac{1}{2} \nabla^2 + v_{eff} \right] \psi_i = \varepsilon_i \psi_i \quad (34)$$

Where  $\varepsilon_i$  is the Kohn-Sham kinetic energy and  $v_{eff}(\mathbf{r})$  is expressed as the following:

$$v_{eff}(\mathbf{r}) = v(\mathbf{r}) + \int \frac{\rho(\mathbf{r}')}{|\mathbf{r} - \mathbf{r}'|} d\mathbf{r}' + v_{xc}(\mathbf{r}) \quad (35)$$

And  $v_{xc}(\mathbf{r})$

$$v_{xc}(\mathbf{r}) = \frac{\delta E_{xc}[\rho(\mathbf{r})]}{\delta[\rho(\mathbf{r})]} \quad (36)$$

Structurally, the Kohn-Sham equations are identical to the Hartree-Fock equations, with the difference that the non-local exchange potential is replaced by the  $v_{xc}$ , local exchange-correlation correction. Both methods are non-linear and solved through multiple iterations; however, the exact electron exchange and correlation energy is not known.

### 2.6.3. Exchange-correlation Energy

Since the exact electronic exchange and correlation are unknown, an approximation must be made. Thus, finding a better exchange-correlation energy has been on-going research. Some of the approximations include local density approximation (LDA) using a homogeneous electron gas model and using an electronic density at a point in space<sup>110</sup>. Therefore, in an inhomogeneous system, it results in incorrect energies. This is true when different charges are present within the system and the presence of any van der Waals bonding interaction. An improvement to LDA is generalized gradient approximation, GGA where the gradient of the density is used for non-homogeneity of the electron density<sup>111</sup>. This corrects the energies for rapid density-changing systems and density changes from the coordinate of calculation.

### 2.6.4. Hybrid Functionals

Later, hybrid functionals, approximations on exchange-correlation energy functionals combined with exact exchange energy calculated using HF, were created. The exact exchange energy functionals are expressed using Kohn-Sham orbitals. This approach was made by Becke in 1993, and the functionals were called “B3” representing “Becke, 3 parameters” where the “3 parameters” are HF exchange, Slater exchange, and Vosko-Wilk-Nusair (VWN) correlation<sup>112</sup>. An improvement was B3 was B3LYP (Becke, 3 parameters, Lee-Yang-Parr), which quickly became the gold standard of the functionals as it significantly improved the thermodynamic properties (atomization energies, bond lengths, and vibration frequencies) of salts and organic compounds<sup>113</sup>. The B3LYP was calculated by multiplying the Becke 88 exchange functionals with LYP correlation functionals<sup>114</sup>.

$$E_{xc} = E_{xc}^{LSDA} + a_0(E_x^{HF} - E_x^{LSDA}) + a_x(E_x^{B8} - E_x^{LSDA}) + a_c(E_c^{LYP} - E_c^{LSDA}) \quad (37)$$

Where  $a_0 = 0.20$ ,  $a_x = 0.72$ , and  $a_c = 0.81$ .

## 2.7. Semi Empirical

As mentioned previously, computational quantum chemistry is always about selecting a method that results in acceptable results within an appropriate time. MM is highly computationally efficient; however, the results often lack accuracy, while the DFT method is one of the most accurate methods, yet it is computationally expensive<sup>115</sup>. However, between the two methods lies the semi-empirical method which utilizes the HF equations with approximations and parameters obtained by empirical data or results from *ab initio* calculations. The parameterization allows the omission of some computationally expensive integrals by replacing them with given data<sup>116</sup>. The method is based on NDDO, neglect of diatomic differential overlap and going back to equation (18),

$$\sum_{v=1}^N (F_{\mu v} - \varepsilon_i S_{\mu v}) c_{vi} = 0 \quad (18)$$

The  $S_{\mu v}$ , N x N overlap matrix is neglected completely. Further improvements were made on the initial model of NDDO and developed into AM1, Austin model 1 where nuclear-nuclear repulsion was implanted for a higher accuracy. As a result, PM6, parameterization method 6 was developed where hydrogen bonds and improved data were implemented for enhanced accuracy<sup>117</sup>. For this study, a semi-empirical method with PM6 as its parameter was used as an initial calculation to decrease the time needed for DFT calculations.

## 2.8. Molecular Mechanics

In contrast to using a quantum mechanics basis, HF and DFT, molecular mechanics (MM) uses Newtonian classical mechanics. The MM ignores quantum mechanics completely and assigns each atom as a “ball” and bonds as a “spring”<sup>118</sup>. The particles are each assigned a radius, polarizability, and charge. Combined, the particles push and pull each other in accordance with their assignment. In contrast to HF or DFT, where individual electrons are considered, MM completely ignores the movement and properties of the electrons. As a result, the energy of the system can be calculated using the following equation:

$$E = E_{covalent} + E_{noncovalent} \quad (38)$$

Where:

$$E_{covalent} = E_{bond} + E_{angle} + E_{dihedral} \quad (39)$$

$$E_{noncovalent} = E_{electrostatic} + E_{van\ der\ Waals} \quad (40)$$

The covalent energies are considered as short-range interactions between individual particles, while the noncovalent energies are long-range interactions between particles that are three or more bonds away from it. Thus, the noncovalent energies could expand to every single particle within the system. To increase the computational speed, a reasonable cutoff distance is applied to increase the efficiency. In general, MM is used to predict and obtain a general idea of the energy and structural parameters with a reduced computational time without the aim of obtaining a high accuracy<sup>119</sup>.

### 2.8.1. Force Field Models

For MM, the force field (FF) is used as its function to define the atomic parameters. The FFs are determined *in silico* and experimentally. The parameters can be summed to find the potential energy using the following equation<sup>120</sup>:

$$E_{MM}(R) = \sum_{bonds} \frac{k_i}{2} (l_i - l_{i,0})^2 + \sum_{angles} \frac{k_i}{2} (\theta_i - \theta_{i,0})^2 + \sum_{torsions} \frac{V_n}{2} (1 + \cos(n\omega - \gamma)) + \sum_{i=1} \sum_{j=i+1} \left( 4\epsilon_{ij} \left[ \left( \frac{\theta_{ij}}{r_{ij}} \right)^{12} - \left( \frac{\theta_{ij}}{r_{ij}} \right)^6 \right] + \frac{q_i q_j}{4\pi\epsilon_0 r_{ij}} \right) \quad (41)$$

The summations represent the parameters of atomic bonds, angles, torsions, van der Waals and electrostatic energies, respectively in order. Note that the bonding and bending terms are expressions of a Taylor series in a second term, as the expansion is often negligible, yet an expansion is available if needed.

In the first summation, atomic bonds are modelled using a harmonic (spring) oscillator and the energy becomes significantly poor as the length of the bond increases. Thus, the equation is very similar to Hooke's law equation, where  $k_i$  is the bonding stretch force constant of the specific atom and  $l_{i,0}$  is an equilibrium bond length<sup>120</sup>. The bonding stretch force constant is defined from values obtained by experiments such as infrared or Raman spectrum<sup>120</sup>.  $l_{i,0}$ , an equilibrium bond length is when the two atoms are bonded and the most stable, lowest energy state they can achieve. The units are expressed as kcal and angstrom.

Second, the summation of bending is the angles produced between three different atoms. The bending summation follows the same mechanism as the bonding summation, where  $k_i$  is a force constant in kcal and  $\theta_{i,0}$  is an equilibrium bond angle expressed in rad.

Third, the torsional terms represent the twisting resulting from the dihedral angles of 4 atoms in a molecule. Given the atoms are numbered consecutively, the rotation results from the second and third atoms.  $V_n$  is the energy barrier of the rotation for a specific bond in kcal. It can be considered as an amplitude of the periodic dihedral graph.  $\omega$  is the dihedral angle in rad and  $\gamma$  is the phase offset in rad.  $V_n$  and  $\gamma$  fit into the parameter values of the equation while  $\omega$  is the only variable value in the equation. The  $n$  term here describes the periodicity of the dihedral function and depends solely on the structure of the molecule. The  $\omega$  angle determines the synperiplanar, gauche, eclipsed, or antiperiplanar (ethane as an example).

Lastly, the last summations are a combination of non-bonding interactions that include the van der Waals and electrostatic interactions. The van der Waals interaction energy summation is expressed as a Lennard-Jones potential equation<sup>120</sup>:

$$E_{vdW} = \sum_{i=1} \sum_{j=i+1} \left( 4\epsilon_{ij} \left[ \left( \frac{\theta_{ij}}{r_{ij}} \right)^{12} - \left( \frac{\theta_{ij}}{r_{ij}} \right)^6 \right] \right) \quad (42)$$

Where the attractive and repulsive forces are dependent on the interatomic distances. The energy is close to zero when the distance is significantly large. In contrast, a decrease in distance leads to an exponential increase in repulsion energy. In between the two exists an optimal distance where attraction exists due to dipole-dipole interactions.  $\epsilon_{ij}$  and  $\theta_{ij}$  are the parameters of the equation, where  $\epsilon_{ij}$  represents the strength of the interactions in kcal and  $\theta_{ij}$  is the van der Waals radius in angstrom. The variable value of the equation is  $r_{ij}$ , the interatomic distance in angstroms.

The electrostatic interaction is heavily influenced by the electronic cloud generated by positive and negatively charged atoms, and the energy is represented by the following equation, the Coulomb potential<sup>120</sup>:

$$E_{el} \sum_{i=1} \sum_{j=i+1} \left( \frac{q_i q_j}{4\pi\epsilon_0 r_{ij}} \right) \quad (43)$$

The two parameters are the charges of the atom,  $q_i$  for  $i$  atom and  $q_j$  for a  $j$  atom. The variable is  $r_{ij}$  which is an interatomic distance. The electrostatic energy becomes critically important for polar and ionic molecules where the atomic charges significantly dominate the potential energy.

In this study, a specific force field AMBER, assisted model building and energy refinement, developed by Kollam was selected for this study as the parameters were optimized specially for peptides, proteins, and nucleic acid<sup>121</sup>. The parameter sets start with "ff" and for this study, ff96 defined by Cornell et al in 1994



was selected as the torsions were modified for *ab initio* calculations. Yet, the equation for the energy calculation remains the same as the original force field calculation.

## 2.9. Conclusion

Efforts to enhance understanding of quantum chemistry allowed the formulation of Schrödinger's equation and Hartree-Fock's equation. Now, different methods of theories and corresponding basis sets can be applied to optimize the structure of the compound, a full-size protein in this study, to estimate the molecular geometries and energy. Although it is impossible to find the exact ground state energy of any compound, the incorporation of different basis sets attempts to minimize this difference. The optimization was first performed using the PM6 semi-empirical method, then DFT using 3-21G and finally with 6-31G\*\* (d,p). This sequence of optimization was performed to minimize the computational time while increasing the accuracy of the optimization. As computational, a theoretical method was discussed, and experimental methods will be discussed. Results from both theoretical and experimental studies show important aspects of the overall findings.

### 3. Experimental Methods

#### 3.1. Microscale Thermophoresis (MST)

Microscale thermophoresis, MST, is a powerful tool that allows the determination of binding affinity,  $K_d$  between protein-ligand, protein-RNA, protein-DNA, and RNA-ligand. MST is based on detecting the change in fluorescence with a temperature change<sup>122</sup>. The sample is loaded onto 4  $\mu$ L capillary and the initial fluorescence of the capillary are measured. An IR laser is applied to the sample to heat the sample, measured for about 30 seconds, then the laser is turned off. The change in temperature,  $\Delta T$ , caused by the IR laser, leads to a local change in molecule concentration, which leads to diffusion or confinement<sup>122</sup>. This movement of concentration due to temperature is called thermophoresis. This migration is dependent on the hydrodynamic radius, charge, and solvation of the sample. It should be noted that temperature-related intensity change (TRIC) can also occur along or independently with thermophoresis<sup>122</sup>. The TRIC is an effect where the fluorescence intensity is temperature-dependent. Soret coefficient,  $ST$ , and percentage of concentration change per Kelvin can be applied to complete the equation of:

$$\frac{C_{hot}}{C_{cold}} = e^{(-S_T \Delta T)}$$

The measured fluorescence values are displayed as normalized fluorescence ( $F_{norm}$ ), which can be calculated using the following equations:

$$F_{norm} = \frac{F_1}{F_0}$$

$$F_{norm} = (1 - X)F_{norm}^{[A]} + F_{norm}^{[AL]}$$

Where  $F_1$  is the fluorescence of the sample that is IR activated, and  $F_0$  is the initial fluorescence of the sample before it is heated.  $X$  is the fraction of fluorescent compounds that formed a complex with a ligand.  $F_{norm}^{[A]}$  is the fluorescence of unbounded complex and  $F_{norm}^{[AL]}$  is the fluorescence of the bonded complex. The first equation is fluorescence measured from TRIC and the latter represents the change from thermophoresis. After analyzing a series of samples, it can be determined which equation should be used. The  $F_{norm}$  can be plotted using a logarithm against ligand concentration to produce a sigmoidal binding curve<sup>123</sup>. From the graph, the binding affinity,  $K_d$ , expressed as the following can be found<sup>124</sup>:

$$K_d = \frac{[A][L]}{[AL]}$$

Where  $[A]$  is the concentration of free fluorescent molecule,  $[L]$  is the concentration of free ligand, and  $[AL]$  is the concentration of the complex.  $[A]$  and  $[L]$  are known concentrations thus, through the quadratic fitting,  $[AL]$  can be found using the following equation<sup>124</sup>:

$$[AL] = \frac{1}{2} (([A_0] + [L_0] + K_d) - (([A_0] + [L_0] + K_d)^2 - (4[A_0][L_0]))^{\frac{1}{2}})$$

As a result, MST is ideal for obtaining the binding affinity between a receptor and its ligand due to ease of operation, small sample quantity requirement, and its accuracy.

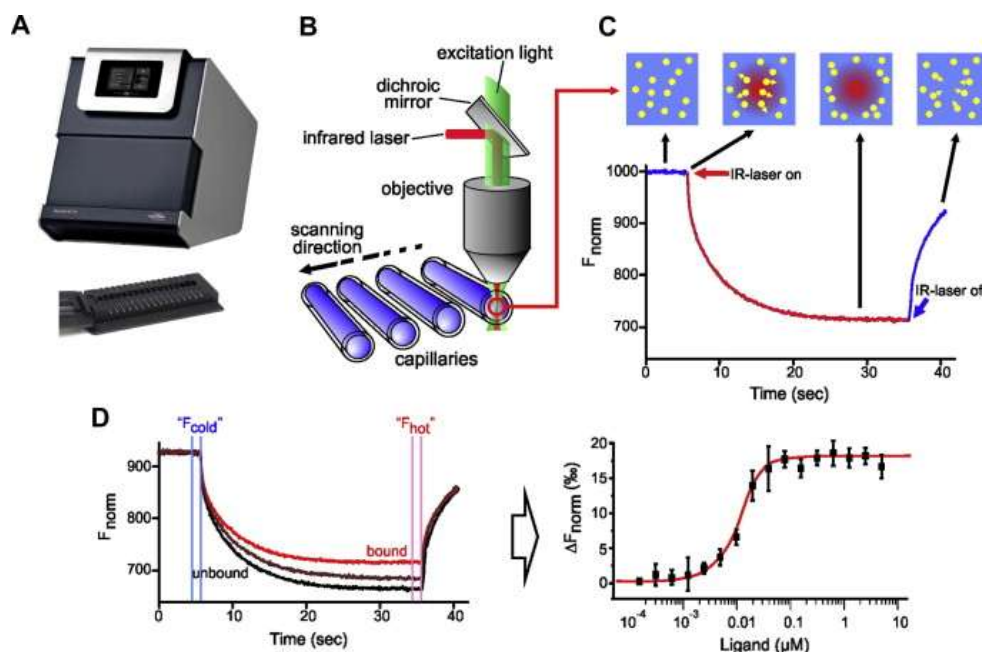


Figure 15. Representation of the mechanism of MST and the data obtained

(Reproduced from Ref <sup>125</sup>)

### 3.2. Fluorescence Spectroscopy

Atoms in their natural state will always attempt to stabilize themselves and achieve ground-state energy. In fluorescence, atoms are excited when a photon is absorbed. As a photon is absorbed, the molecule will become excited and proceed into internal conversion and or vibrational relaxation before emitting fluorescence, a photon with a different wavelength. In the decay from the second excitation state,  $S_2$  to  $S_1$ , the first excitation state, thermal energy is lost due to the vibration of the atoms<sup>126</sup>. At the lowest  $S_1$ , the photon is then released from the compound, and this process often occurs within nanoseconds<sup>126</sup>. As a result, the wavelength of the

emission spectra will always have a higher wavelength in its maxima compared to absorption. This process is called the Stokes shift<sup>127</sup>. This overall process can be perfectly visualized by the Jablonski diagram as seen in *Figure 16*.

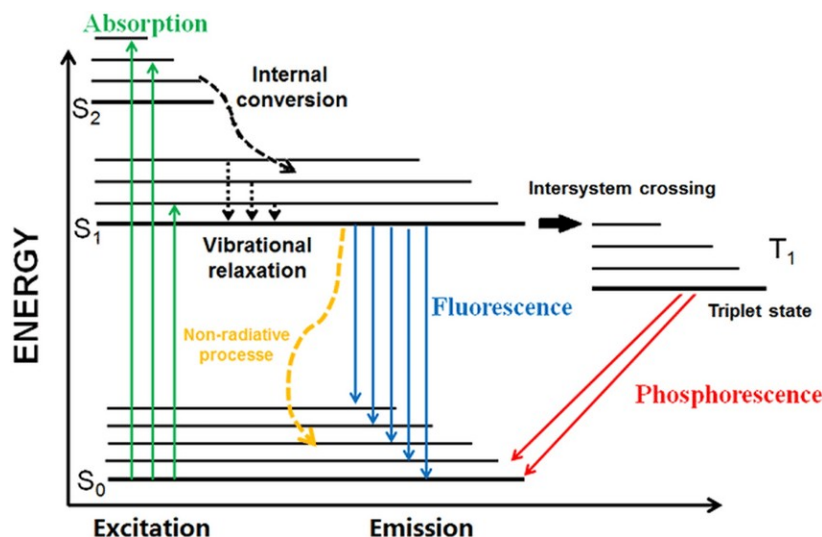


Figure 16. Jablonski diagram representing the excitation and fluorescence emission

(Reproduced from Ref<sup>128</sup>)

Following the Jablonski diagram, the fluorometer can measure and produce an excitation spectrum and an emission spectrum<sup>126</sup>. An excitation spectrum can be produced when the emission wavelength is fixed to a specific wavelength and the excitation monochromator wavelength is measured. Through this spectrum, a specific wavelength that is able to absorb and emit can be identified. An emission spectrum is when the excitation wavelength is fixed and scanned by changing the emission wavelength. As it scans, intensity vs emission wavelength can be plotted.

The instrument uses LEDs or xenon lamps to produce UV/Vis light which is passed through a monochromator with a specific slit size which allows the selection of specific wavelengths. The wavelength passes through a sample and is detected by a detector 90 degrees from the light source. The detector determines the intensity of the wavelength and produces a graph that can be used for analysis<sup>126</sup>.

Furthermore, thanks to recent developments, the excitation-emission matrix (EEM) can be measured. EEM is a compilation of graphs consisting of excitation wavelength vs emission wavelength vs fluorescence intensity visualized in a 3D graph<sup>129</sup>. As a result, it can be utilized to determine the three components of fluorescence with a single scan.

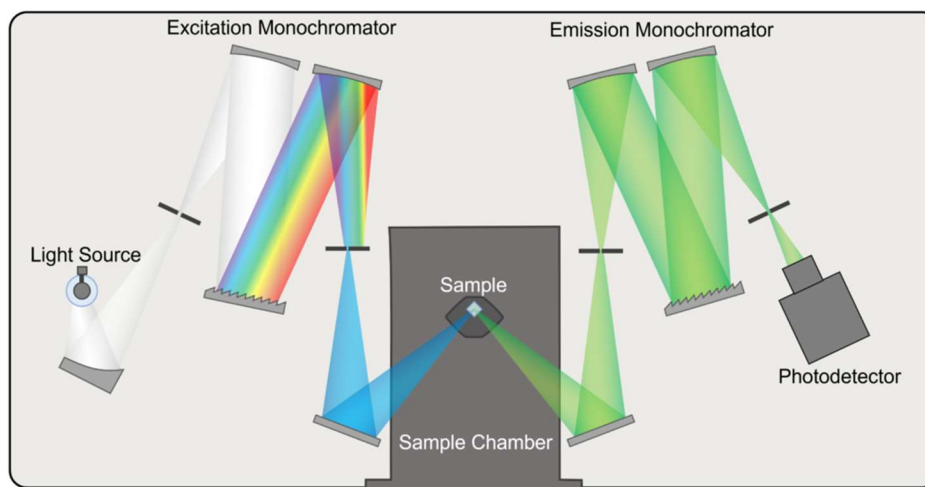


Figure 17. Diagram of the fluorometer with excitation and emission monochromators

(Reproduced from Ref <sup>130</sup>)

This method was used in our study to detect the fluorescence of Indium Oxine where it could be used to determine the encapsulation of Indium-Oxine inside PSMA.

### 3.3. Neutron Activation Analysis (NAA)

Neutron activation analysis is a powerful tool that can be used for elemental analysis of a sample on a ppm scale. A sample is exposed to neutrons, which are determined by the neutron flux of the reactor, and with the incidence of the neutrons, predominantly by neutron capture, the nucleus of the atoms becomes heavier and becomes excited into an unstable state. As a result, the unstable atoms attempt to stabilize themselves through various radioactive decay: alpha, beta, and gamma decay<sup>66</sup>. Before NAA, if the elements in the sample are known, an appropriate neutron flux and irradiation time can be set to obtain high-resolution results. Furthermore, the decay of the elements must be considered before the sample is irradiated to ensure a specific type of radioactive decay and time is obtained. A high-purity Germanium (HPGe) detector is used to detect the gamma rays produced by the sample and generate a graph of counts per selective energy value. HPGe uses Germanium, a semiconductor diode with a P-type contact (cathode boron) which is placed in the outer layer, N-type (anode lithium) in the center, and an intrinsic layer which is stationed between the P and N-type contacts with an electric field. The electric field generated in the intrinsic layer reacts with gamma radiation, producing free electrons and electron holes<sup>131</sup>. The free electrons move to the N-contact while the holes move to the P-contact. The number of electron-hole pairs is directly proportional to the number of energies of the gamma radiation. The number of hole

pairs is converted into a voltage pulse by a preamplifier, which is detected by a computer. Thus, the radiation can be converted to “gamma peaks” that correspond to the counts of the activity of the irradiated sample, determining the number of specific atoms that are present in the sample<sup>132</sup>.

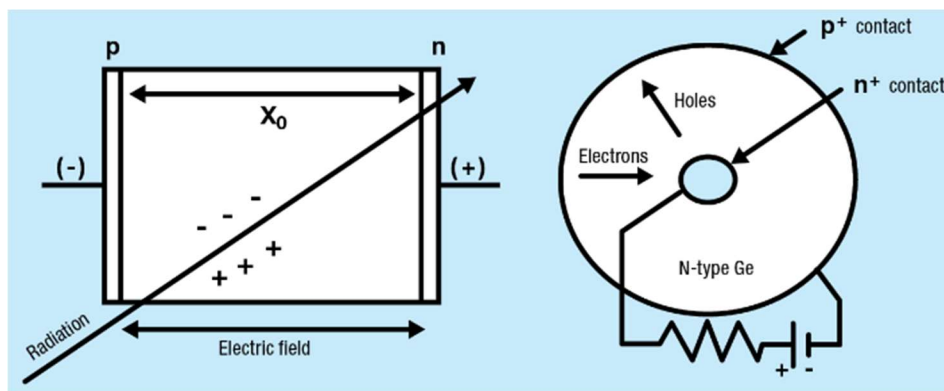


Figure 18. Cross section of High Purity Germanium detectors with p-type and n-type bands with movements of electrons

(Reproduced from Ref<sup>133</sup>)

This method was used in our study to determine the amount of Indium present in the polymer solution to determine the encapsulation of Indium-Oxine inside PSMA.

### 3.4. Thin Layer Chromatography

Chromatography is a method of analysis where a mixture of liquid or gas can be separated into different phases. Thin layer chromatography (TLC) is a separation analysis method using a stationary phase and a mobile phase. The stationary phase is determined by the TLC plates, which are made out of silica gel, cellulose or aluminum oxide. The stationary phase is chemically inert, and depending on the compounds in the mixture, a specific plate can be chosen. The mobile phase of the TLC is selected from a solvent selected, and these solvents can be a mixture of two compounds with a specific ratio. The ratio and compound used are determined by the sample solution being tested. The polarity of the sample and the solvent is the key part in determining the suitability. Less polar compounds will move up higher on the plate compared to more polar compounds, given the same solvent is used as a mobile phase. The separation is determined by the retention factor,  $R_f$  which can be calculated by<sup>134</sup>:

$$R_f = \frac{\text{distance traveled by sample}}{\text{distance traveled by solvent}}$$

The  $R_f$  value is between 0.0 to 1.0, where 0.0 is the initial starting point and 1.0 is the end point. The lines of 0.0 and 1.0 are drawn using a pencil, and the distances between the two lines must be measured. The distance is not significant however, distance is often linearly proportional to the time it takes for the sample to move. The samples are loaded to the 0.0 line and placed into a tube, and the solvent moves up the plate due to capillary action.

### 3.5. Phosphor Imaging

The analysis of the TLC can be completed using visual, fluorescence, or phosphor screens. Visual analysis can be done if the sample has a colour for a distinct classification, or fluorescence can be used if the sample has fluorescent properties<sup>134</sup>. For irradiated compounds, it is difficult to access the instruments due to the radiation. A solution to this problem is using phosphor imaging, where the radioactive TLC plates can be placed on the phosphor screen. Phosphor screens are composed of the photostimulable phosphor crystal lattice,  $\text{BaFBr}^-:\text{Eu}^{2+}$  which transitions into  $\text{BaFBr}:\text{Eu}^{3+}$  when radiation strikes the  $\text{Eu}^{2+}$  ions from the crystal structure. Electrons lost from the ion enter the conduction band and become trapped in the bromine. This transition moves the compound to a higher-energy stable state and a high wavelength; a low-energy photon allows for transition of  $\text{BaFBr}^-:\text{Eu}^{2+}$  to excited  $\text{BaFBr}^-:\text{Eu}^{2+*}$  state. From the excited state, it relaxes into its ground state by emitting a high energy, 400 nm blue-violet light<sup>135</sup>. The emitted light is captured by a phosphor image instrument. By the intensity of the imaging, the radioactivity can be estimated which can be especially useful in TLC as the movement phases can be seen.

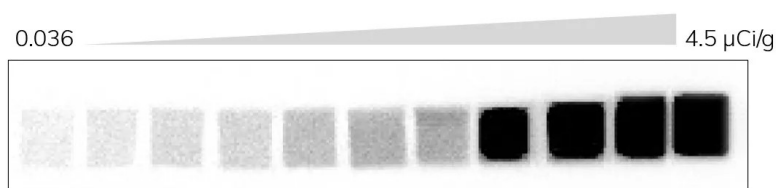


Figure 19. The different intensities in the phosphor screen depend on the radioactivity of the compound.

(Reproduced from Ref <sup>136</sup>)

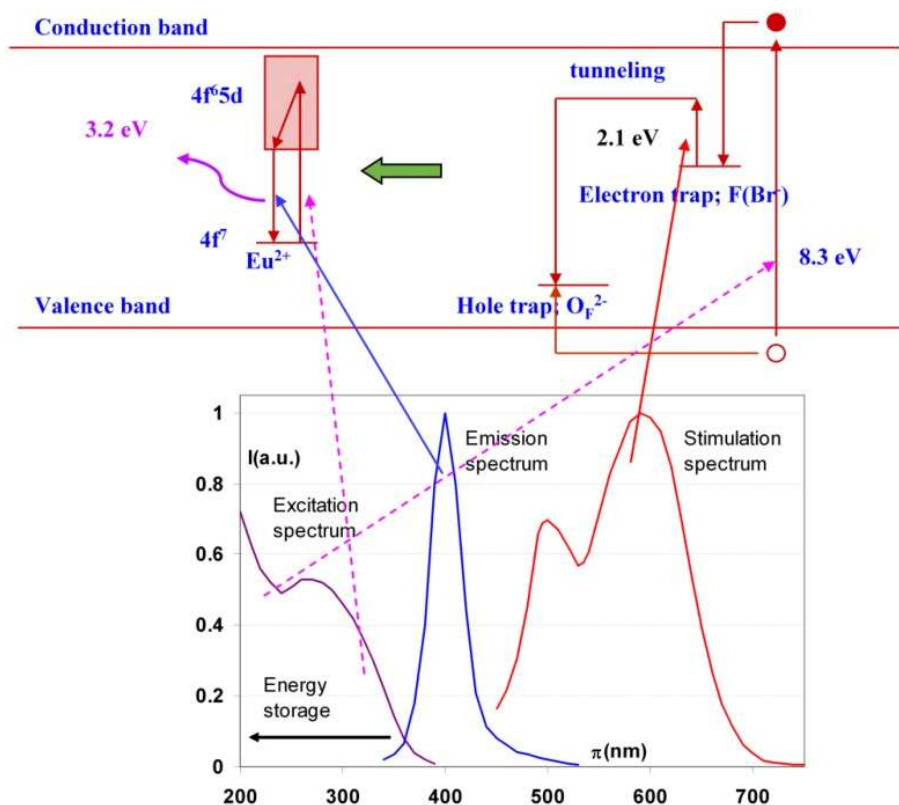


Figure 20. The electron movement due to radiation, low energy photon excitation, and emission of photons

(Reproduced from Ref<sup>135</sup>)

This method was used in our study to determine the encapsulation of radioactive  $^{111}\text{Indium-Oxine}$  inside the PSMA.



## 4. Computational Results

### 4.1. Introduction

Targeted drug delivery has been recognized as a promising method for effective cancer treatment while avoiding the negative impact on the quality of life of patients<sup>56</sup>. Previous experiments have determined the promising potential of functionalized polymer, FA-DABA-PSMA as a targeted drug carrier<sup>62,63,95,96</sup>. Using a 2,4-diaminobutyric acid (DABA) linker, folic acid (FA) and poly (styrene-alt-maleic acid) can be conjugated to form a functionalized polymer. At physiological pH, the polymer is able to form a self-assembled structure with a hydrophilic outer layer and a hydrophobic inner layer. The formation of this self-assembly is a result of hydrogen bonding between the maleic acids and the hydrophobic interactions of the styrene rings. When FA is conjugated to PSMA directly, the hydrogen bonding of the PSMA is disturbed, resulting breakage of the linearity of the backbone of the polymer. Thus, an appropriate linker that is able to maintain the linearity of the polymer backbone was determined to be the DABA through molecular simulation. The FA and DABA were attached to every 10th monomer of the polymer chain to maximize the intake probability while maintaining the linear backbone of the polymer. The polymer and the linker are both compatible compounds that have been approved by the FDA.

From previous studies, it has been observed that empty FA-DABA-PSMA was able to reduce the viability of the cancer cells *in vitro*<sup>95</sup>. This was a surprise finding as the four compounds in the functionalized polymer are all nontoxic compounds. The cause of this phenomenon could be due to the inability of FA to detach from FR $\alpha$  to take part in the normal cancer cell metabolism. Indeed, the FR $\alpha$  is positioned in the cell surface by the glycosyl-phosphatidylinositol (GPI) anchor enters the cell via endocytosis<sup>137</sup>. It moves through the endosome to reach the lysosome where it creates an acidic environment to release the FA from the receptor. Once detached, the FA enters the folate-methionine cycle to synthesize DNA, while the receptor is used as the DNA transcription factor in the nucleus or recycled back to the surface of the cell to encapsulate more FA. This important function agrees with the characteristics of cancers as they are mutated cells that are proliferating at uncontrollable rate. Thus, when the FR $\alpha$  is unable to release a FA or FA derivative, the receptor is unable to be used in the nucleus or recycled back to the surface of the cell. As a result, the cell produces more FR $\alpha$  to be present to encapsulate more FA. In addition, FA-DABA-PSMA is a derivative of FA which may behave differently in the folate cycle due to the addition of the polymer. In conclusion, with overexpression of FR $\alpha$  found in multiple cancers, it serves as an excellent target for targeted drug delivery and possible disruptor of the folate cycle and DNA transcription in the nucleus<sup>83,84</sup>.

Recent study has found that internalization of the FA-DABA-PSMA 350 kDa was enhanced with the usage of MAL2, SNA-1, and PNA lectins, while 20 kDa

only saw an increase in internalization when WGA lectin was used *in vitro*<sup>138</sup>. This improved endocytosis of the receptor could be explained by the additional flexibility of the FR $\alpha$  when interacting with lectins<sup>138</sup>. This recent finding suggests the importance of detailed analysis of FA-DABA-PSMA and its effects on FA interaction with FR $\alpha$ . Furthermore, by understanding the interaction and relationship between the FA-DABA-PSMA and FR $\alpha$ , it may serve as an important information for further study, usage of FA-DABA-PSMA as a theragnostic agent which will be discussed later in this paper.

To determine the effect of the polymer on the structure and binding strength of FR $\alpha$ , computational chemistry using molecular mechanics, semi-empirical, and density function theory can be used to optimize the complex to simulate the binding between FA, FA-DABA-PSMA with FR $\alpha$ . After optimization, a binding energy can be calculated by separating the complex and optimizing it individually.

## 4.2. Methods

The optimization of the complex was completed using Gaussian 16 software<sup>139</sup>. The FR $\alpha$  was obtained from RCSB Protein Data Bank, 4LRH, <https://doi.org/10.2210/pdb4lrh/pdb>. Specific amino acids, Y60, D81, Y85, W102, R103, R106, H135, K136, G137, W138, W140, W171, S174, and Y175 that directly have hydrophilic and hydrophobic interactions were selected as “High level” in the ONIOM model along with the FA and trimer of FA-DABA-PSMA<sup>94,140</sup>. Trimer was chosen to present the PSMA chain to accurately represent the polymer chain while reducing the computational time. The rest of the amino acids in the protein complex were chosen as “Low level” in the ONIOM model. The Low level was modeled using AMBER force field while the High level was modeled initially using semi-empirical PM6 then DFT using B3LYP functional with 3-21G then with 6-31G\*\*. The complex was protonated at pH 7.4 and pH 5.5 using PDB2PQR<sup>141</sup>. Optimization was performed using a computer cluster at the Centre for Advanced Computing.

Computation using a high level of theory requires a significant number of computational resources and time for completion. Thus, “pre-optimization” of the complex using a lower level is essential. An optimized structure of the complex from the lower level of theory is optimized using a higher level of theory. Besides the essential amino acids of the FR $\alpha$  that interact with the FA/FA-DABA-PSMA complex, the rest of the amino acids were kept at the AMBER force field. Two types of calculation were performed: first, optimized pH 7.4 at 3-21G structures were protonated to pH 5.5 and then optimized using 3-21G to simulate the release of the ligand from FR $\alpha$ . Second, unoptimized FR $\alpha$  was protonated to pH 5.5 and optimized as defined in method #1 and method #2 below:

Method #1: The first method was performed to determine if the release of the ligand from the FR $\alpha$  can be simulated as protonation was performed on the optimized pH 7.4 complex.

Method #2: The second method was performed by protonating the FR $\alpha$  to pH 5.5 without the use of optimized pH 7.4 to determine if any difference would be seen. The second method would eliminate any bias that may be caused by using an optimized pH 7.4 complex.

The binding energy was calculated using the following formula:

$$E_{binding} = E_{opt-complex} - (E_{opt-receptor} + E_{opt-ligand})$$

Where  $E_{opt-complex}$  is the energy of converged structure of the complex, ligand inside the receptor,  $E_{opt-receptor}$  is the energy of the converged structure of the receptor that was reoptimized after ligand was removed, and  $E_{opt-ligand}$  is the energy of the converged structure of the ligand that was reoptimized after the receptor is removed.

The interaction energy was calculated using:

$$E_{Int} = E_{opt-complex} - (E_{receptor} + E_{ligand})$$

Where  $E_{opt-complex}$  is the energy of the converged structure of the complex, ligand inside the receptor,  $E_{receptor}$  is the energy of the converged structure of the receptor without ligand or reoptimization, and  $E_{ligand}$  is the energy of the converged structure of the ligand without receptor or reoptimization.

## 4.3. Results and Discussion

### 4.3.1. Method #1

As discussed in the methods section, method #1 was used to simulate the release of FA or FA-DABA-PSMA. The complex was first optimized at pH 7.4. The optimized complex was then protonated to pH 5.5 and optimized. This protonation of the optimized pH 7.4 complex would simulate the release of the ligand *in vitro*. Green circles were drawn on the hydrogen bonds between the amino acids of the FR $\alpha$  and FA / FA-DABA-PSMA with red arrows indicating the 1-letter symbol and number of the specific amino acid of the receptor.

#### 4.3.1.1. Interaction of FA with FR $\alpha$

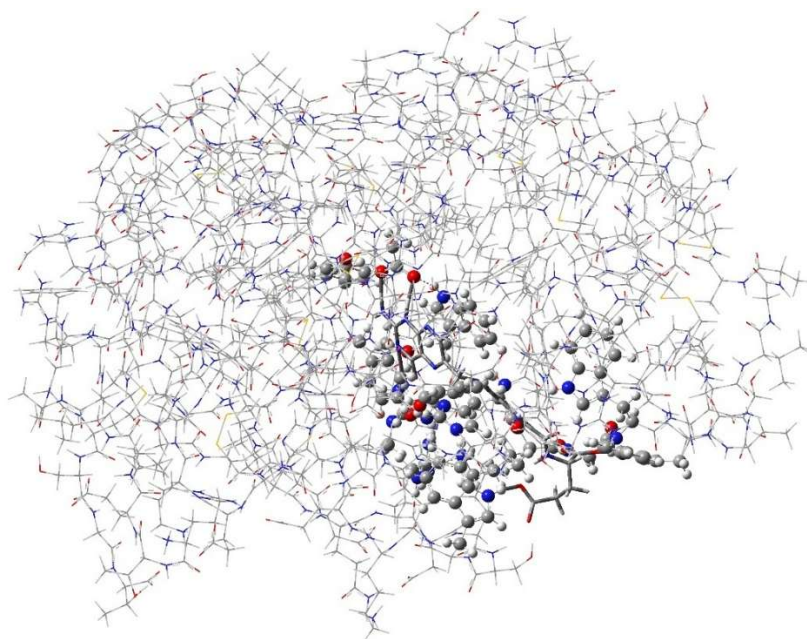


Figure 21. Overview of the FA and FR $\alpha$  with amino acids that interact FA are represented as Balls and sticks, rest of the proteins as wireframe and FA as a tube at pH 7.4.

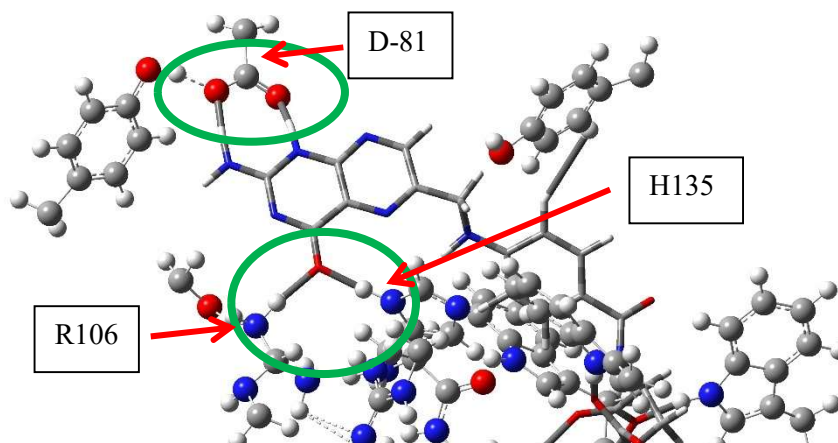


Figure 22. Hydrogen bonding between FA and amino acid (D81, R106 and H135) in the FR $\alpha$  at pH 7.4

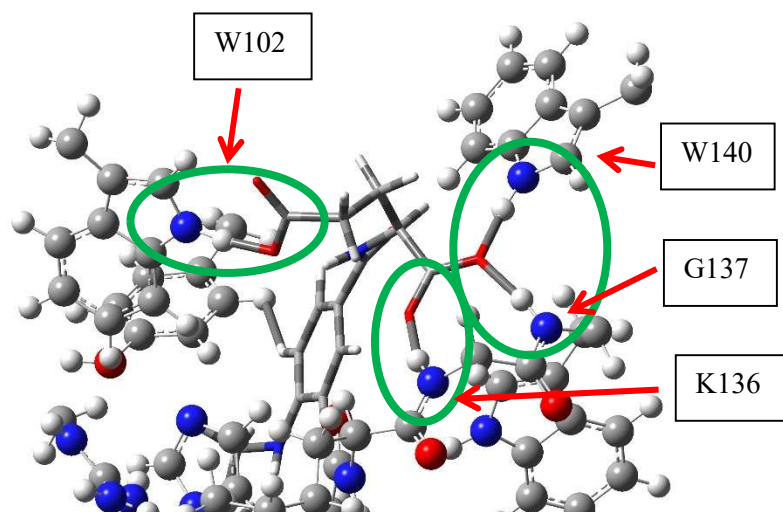


Figure 23. Hydrogen bonding between FA and amino acid (W102, K136, G137, and W140) in the FR $\alpha$  at pH 7.4

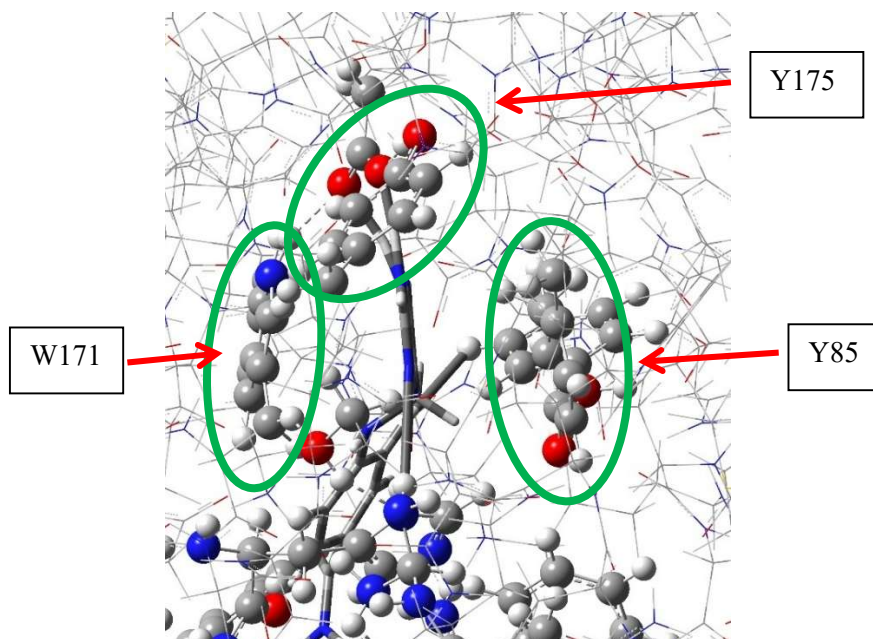


Figure 24. Hydrophobic Interaction between FA and amino acid (Y85, W171, and Y175) in the FR $\alpha$  at pH 7.4

**Table 1.** List of amino acids and interaction with FA at pH 7.4

| Abbreviation of the amino acid | Full name of the amino acid | Type of interaction with FA         | Bond length with FA |
|--------------------------------|-----------------------------|-------------------------------------|---------------------|
| Y60                            | Tyrosine - 60               | Hydrophobic: $\pi$ - $\pi$ stacking | N/A                 |
| D81                            | Aspartic Acid - 81          | Hydrogen bond                       | 1.66, 1.70          |
| Y85                            | Tyrosine - 85               | Hydrophobic: $\pi$ - $\pi$ stacking | N/A                 |
| W102                           | Tryptophan - 102            | Hydrogen bond                       | 1.82                |
| R103                           | Arginine - 103              | No Bonding                          | No Bonding          |
| R106                           | Arginine - 106              | Hydrogen bond                       | 1.83                |
| H135                           | Histidine - 135             | Proton Exchange                     | 1.33                |
| K136                           | Lysine - 136                | No Bonding                          | No Bonding          |
| G137                           | Glycine - 137               | Hydrogen bond                       | 1.83                |
| W138                           | Tryptophan - 138            | Hydrogen bond                       | 1.93                |
| W140                           | Tryptophan - 140            | Hydrogen bond                       | 1.66                |
| W171                           | Tryptophan - 171            | Hydrophobic: $\pi$ - $\pi$ stacking | N/A                 |
| S174                           | Serine - 174                | No Bonding                          | No Bonding          |
| Y175                           | Tyrosine - 175              | Hydrophobic: $\pi$ - $\pi$ stacking | N/A                 |

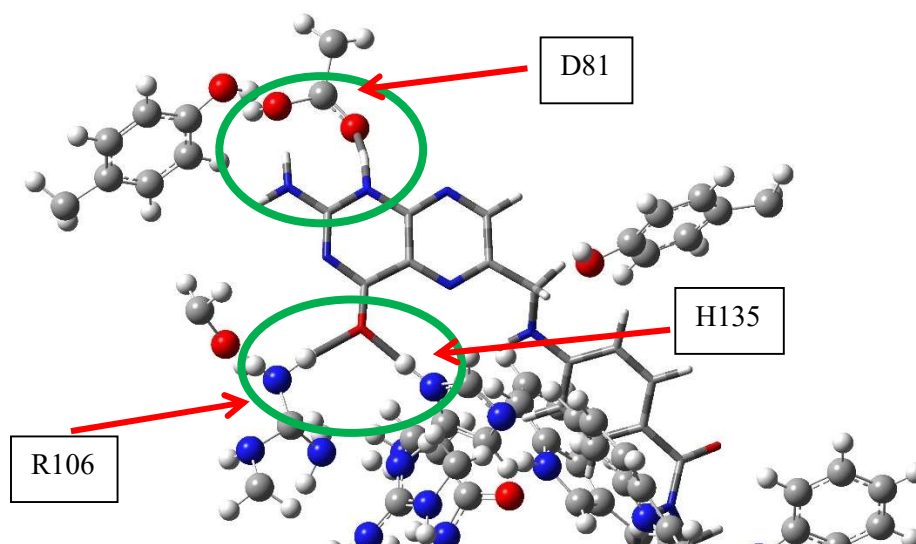


Figure 25. Hydrogen bonding between FA and amino acid (D81, R106, and H135) in the FR $\alpha$  at pH 5.5

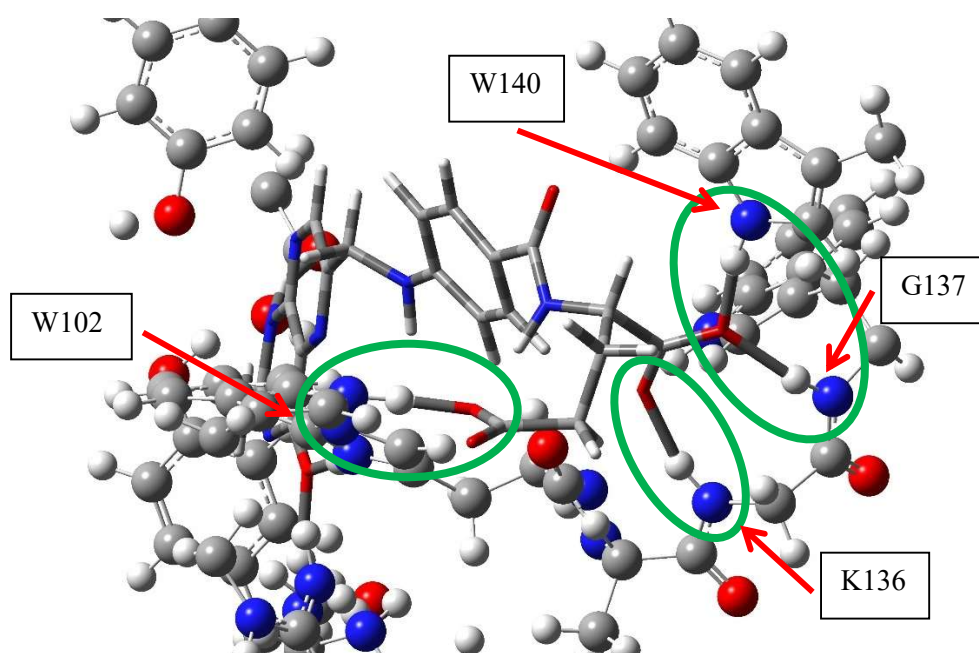


Figure 26. Hydrogen bonding between FA and amino acid (W102, K136, G137, and W140) in the FR $\alpha$  at pH 5.5

**Table 2.** List of amino acids and interaction with FA at pH 5.5

| Abbreviation of the amino acid | Full name of the amino acid | Type of interaction with FA         | Bond length with FA |
|--------------------------------|-----------------------------|-------------------------------------|---------------------|
| Y60                            | Tyrosine - 60               | Hydrophobic: $\pi$ - $\pi$ stacking | N/A                 |
| D81                            | Aspartic Acid - 81          | Hydrogen bond                       | 1.69, 1.82          |
| Y85                            | Tyrosine - 85               | Hydrophobic: $\pi$ - $\pi$ stacking | N/A                 |
| W102                           | Tryptophan - 102            | Hydrogen bond                       | 1.47                |
| R103                           | Arginine - 103              | No Bonding                          | No Bonding          |
| R106                           | Arginine - 106              | Hydrogen bond                       | 2.10                |
| H135                           | Histidine - 135             | Proton Exchange                     | 1.07                |
| K136                           | Lysine - 136                | No Bonding                          | No Bonding          |
| G137                           | Glycine - 137               | Hydrogen bond                       | 1.79                |
| W138                           | Tryptophan - 138            | Hydrogen bond                       | 1.97                |
| W140                           | Tryptophan - 140            | Hydrogen bond                       | 1.69                |
| W171                           | Tryptophan - 171            | Hydrophobic: $\pi$ - $\pi$ stacking | N/A                 |
| S174                           | Serine - 174                | No Bonding                          | No Bonding          |
| Y175                           | Tyrosine - 175              | Hydrophobic: $\pi$ - $\pi$ stacking | N/A                 |



As seen from *Figure 22* and *25*, the structures optimized through calculation method #1 showed that, despite the protonation of FR $\alpha$  to pH 5.5, the amino acids that formed the hydrogen bond at pH 7.4 can be observed similarly with pH 5.5. As previously mentioned, the amino acid D81 is the biggest contributor to the binding affinity of FA with FR $\alpha$ . The mutation of the amino acid significantly decreases the binding affinity, most likely decrease in the hydrogen bonding<sup>94</sup>. This suggests the carboxylic acid of this group strongly binds with nitrogen atoms in the pterin group. Thus, the protonation of D81 should repel the pterin group of the FA, yet, as seen in *Figure 25*, the protonated hydrogen repels away from the pterin group and interacts with the alcohol group of the Y175 amino acid. Next, the interaction between FA-DABA-PSMA and FR $\alpha$  will be discussed.

#### 4.3.1.2. Interaction of FA-DABA-PSMA with FR $\alpha$

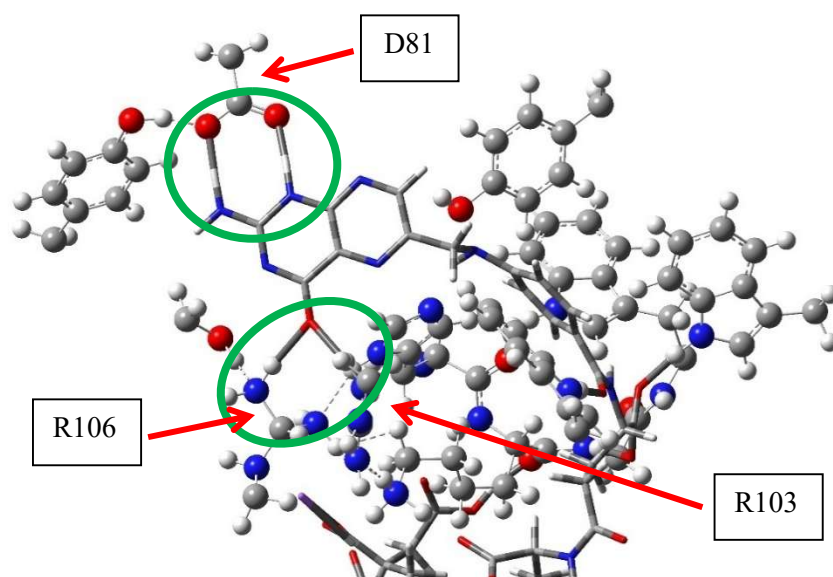


Figure 27. Hydrogen bonding between FA-DABA-PSMA and amino acid (D81, R103, and R106) in the FR $\alpha$  at pH 7.4



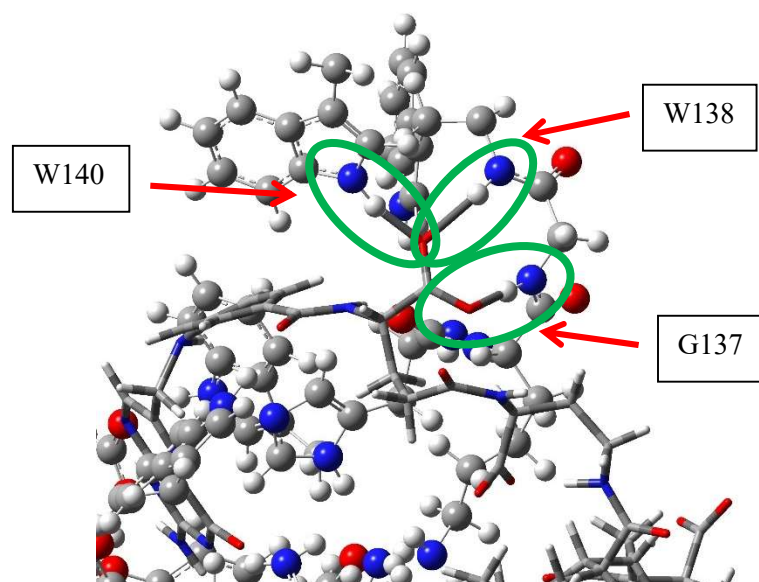


Figure 28. Hydrogen bonding between FA-DABA-PSMA and amino acid (G137, W138, and W140) in the FR $\alpha$  at pH 7.4

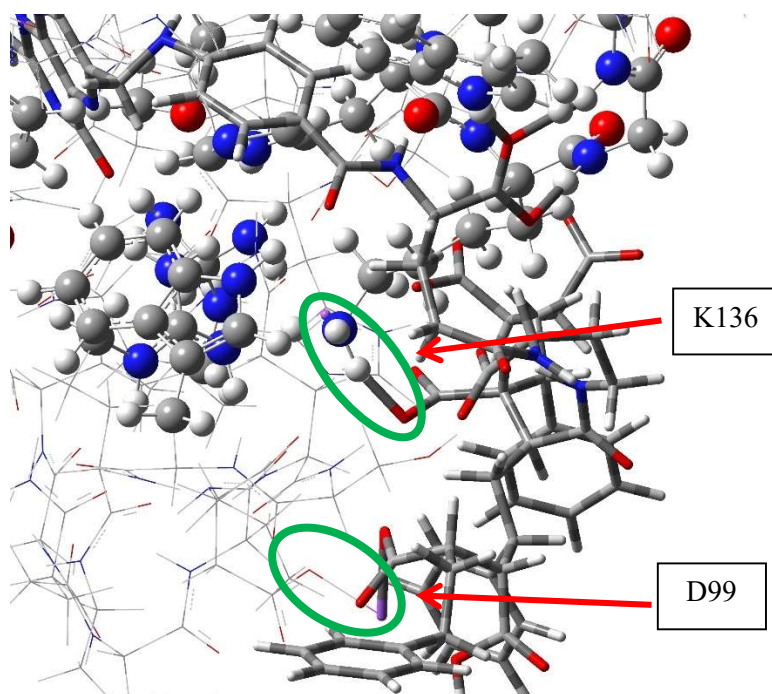


Figure 29. Hydrogen bonding between FA-DABA-PSMA and amino acid (D99 and K136) in the FR $\alpha$  at pH 7.4

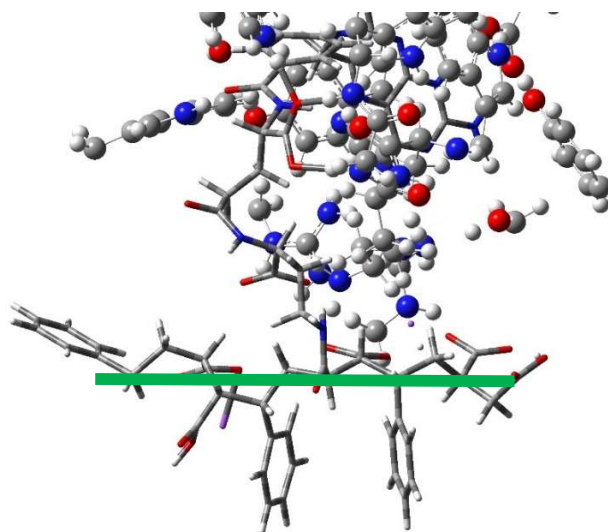


Figure 30. Top view of the PSMA chain with a green line to present the linearity of the polymer backbone

**Table 3.** List of amino acids and interaction with FA-DABA-PSMA at pH 7.4

| Abbreviation of the amino acid | Full name of the amino acid | Type of interaction with FA         | Bond length with FA-DABA-PSMA |
|--------------------------------|-----------------------------|-------------------------------------|-------------------------------|
| Y60                            | Tyrosine - 60               | Hydrophobic: $\pi$ - $\pi$ stacking | N/A                           |
| D81                            | Aspartic Acid - 81          | Hydrogen bond                       | 1.71, 1.75                    |
| D99                            | Aspartic Acid - 99          | Hydrogen bond                       | 2.19                          |
| Y85                            | Tyrosine - 85               | Hydrophobic: $\pi$ - $\pi$ stacking | N/A                           |
| W102                           | Tryptophan - 102            | Hydrogen bond                       | 1.65                          |
| R103                           | Arginine - 103              | Hydrogen bond                       | 2.10                          |
| R106                           | Arginine - 106              | Hydrogen bond                       | 2.05                          |
| H135                           | Histidine - 135             | No Bonding                          | No Bonding                    |
| K136                           | Lysine - 136                | Hydrogen bond                       | 1.63                          |
| G137                           | Glycine - 137               | Hydrogen bond                       | 1.58                          |
| W138                           | Tryptophan - 138            | Hydrogen bond                       | 2.04                          |
| W140                           | Tryptophan - 140            | Hydrogen bond                       | 1.66                          |
| W171                           | Tryptophan - 171            | Hydrophobic: $\pi$ - $\pi$ stacking | N/A                           |
| S174                           | Serine - 174                | No Bonding                          | No Bonding                    |
| Y175                           | Tyrosine - 175              | Hydrophobic: $\pi$ - $\pi$ stacking | N/A                           |

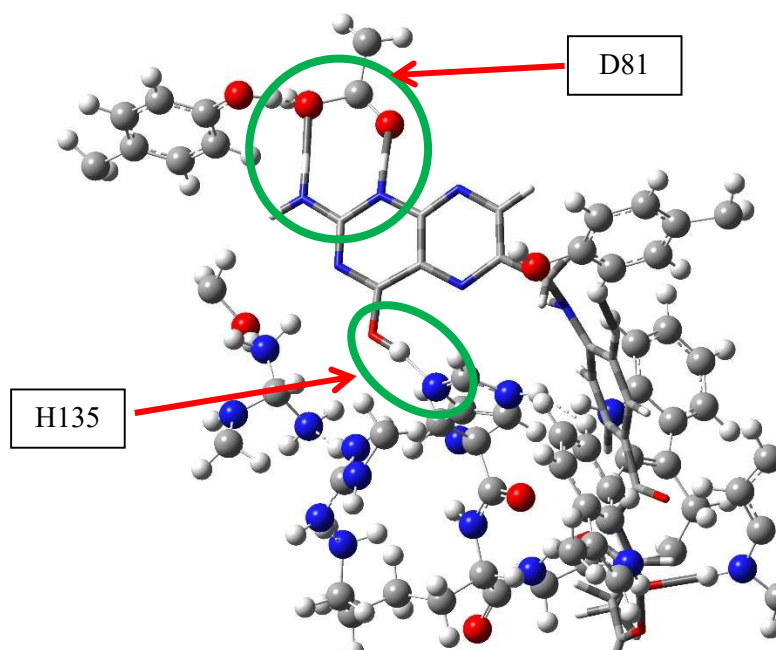


Figure 31. Hydrogen bonding between FA-DABA-PSMA and amino acid (D81 and H135) in the FR $\alpha$  at pH 5.5

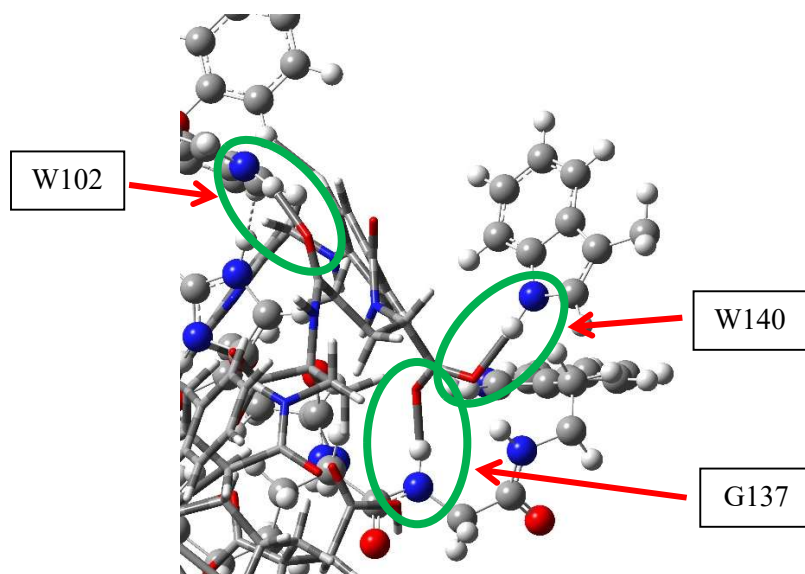


Figure 32. Hydrogen bonding between FA-DABA-PSMA and amino acid (W102, G137, and W140) in the FR $\alpha$  at pH 5.5

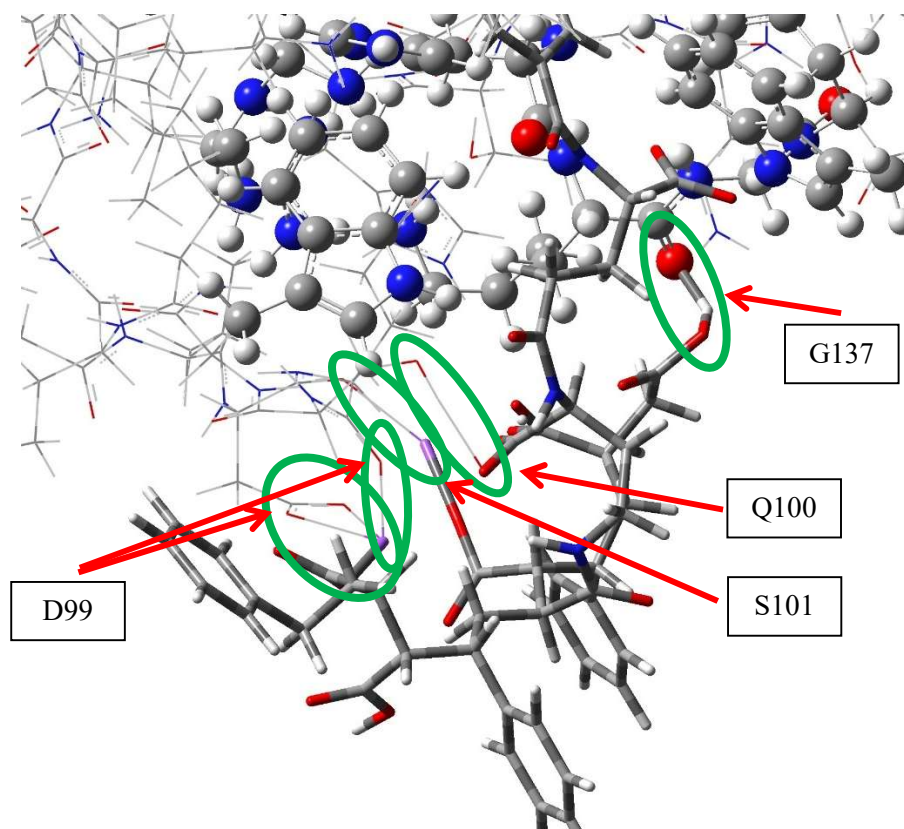


Figure 33. Hydrogen bonding between FA-DABA-PSMA and amino acid (D99, Q100, S101 and G137) in the FR $\alpha$  at pH 5.5

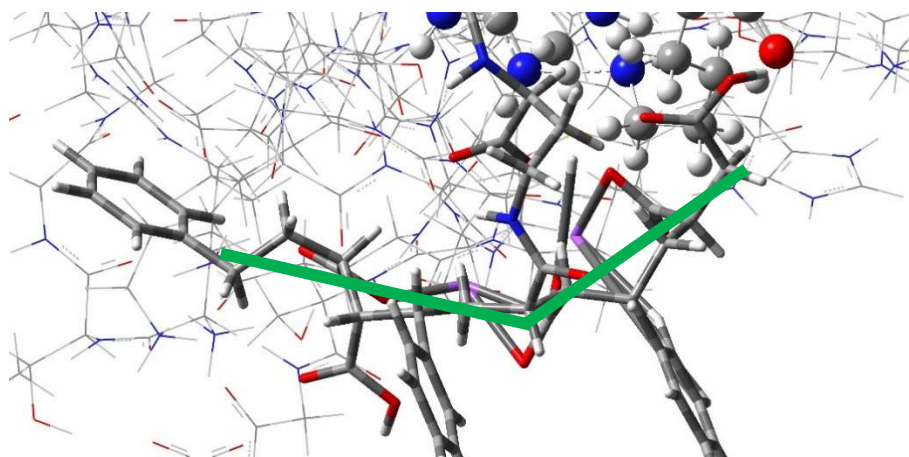
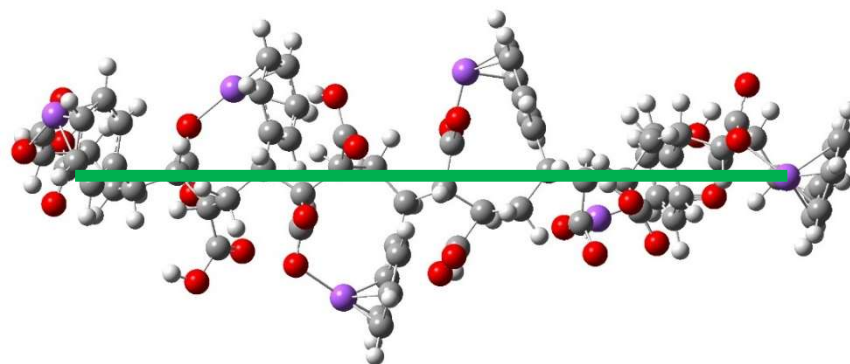


Figure 34. Top view of the PSMA chain with a green line to present the bending of the polymer backbone

**Table 4.** List of amino acids and interaction with FA-DABA-PSMA at pH 5.5

| Abbreviation of the amino acid | Full name of the amino acid | Type of interaction with FA         | Bond length with FA-DABA-PSMA |
|--------------------------------|-----------------------------|-------------------------------------|-------------------------------|
| Y60                            | Tyrosine - 60               | Hydrophobic: $\pi$ - $\pi$ stacking | N/A                           |
| D81                            | Aspartic Acid - 81          | Hydrogen bond                       | 1.66, 1.84                    |
| D99                            | Aspartic Acid - 99          | Hydrogen bond                       | 2.24, 2.32, 2.35              |
| Q100                           | Glutamine - 100             | Hydrogen bond                       | 2.36                          |
| S101                           | Serine - 100                | Hydrogen bond                       | 1.95                          |
| Y85                            | Tyrosine - 85               | Hydrophobic: $\pi$ - $\pi$ stacking | N/A                           |
| W102                           | Tryptophan - 102            | Hydrogen bond                       | 1.85                          |
| R103                           | Arginine - 103              | Proton Exchange                     | 1.05                          |
| R106                           | Arginine - 106              | No Bonding                          | No Bonding                    |
| H135                           | Histidine - 135             | No Bonding                          | No Bonding                    |
| K136                           | Lysine - 136                | No Bonding                          | No Bonding                    |
| G137                           | Glycine - 137               | Hydrogen bond                       | 1.60, 1.70                    |
| W138                           | Tryptophan - 138            | Hydrogen bond                       | 1.80                          |
| W140                           | Tryptophan - 140            | Hydrogen bond                       | 1.75                          |
| W171                           | Tryptophan - 171            | Hydrophobic: $\pi$ - $\pi$ stacking | N/A                           |
| S174                           | Serine - 174                | No Bonding                          | No Bonding                    |
| Y175                           | Tyrosine - 175              | Hydrophobic: $\pi$ - $\pi$ stacking | N/A                           |

**Figure 35.** Top view of PSMA hexamer with a green line representing the linear backbone carbon chain

As expected, the hydrophilic maleic acid of the polymer forms hydrogen bonds with the amino acids of the receptor. Inside the pocket, no major movements

were observed from the amino acids that interact with the pterin group when compared to FA with FR $\alpha$ . However, at pH 7.4, the oxygen from the pterin group formed a hydrogen bond with R103 and R106 instead of H135 as shown in *Figure 27*. The most important findings were the hydrogen bonds between the amino acid of the receptor and the maleic acid. At pH 7.4, amino acids D99 and G137 were identified forming a hydrogen bond with maleic acid as depicted in *Figure 29*, while at pH 5.5, D99, Q100, S101, and G137 participated which can be observed in *Figure 33*. This formation of hydrogen bonds suggests a strong interaction between the FA-DABA-PSMA with FR $\alpha$ . A consideration of the level must be made, as the lower level was optimized using an AMBER force field. AMBER force field doesn't allow the formation of hydrogen bonds between the low and high levels, as the high-level treats electron explicitly using DFT while the AMBER FF does not consider electrons in the optimization process. Unquestionably, if the surface of the FR $\alpha$  was selected as high and optimized using DFT, it is highly likely that the formation of hydrogen bonds between the FR $\alpha$  and FA-DABA-PSMA would increase. Subsequently, the backbone of the polymer chains was observed to identify if occurrence of bending. In pH 7.4, as in *Figure 30*, the polymer was able to maintain a straight backbone chain, whereas in *Figure 34*, a bending of the backbone can be observed. This agrees with the formation of the hydrogen bonds between the polymer and the receptor as the hydrophilic amino acids from the surface of the receptor are "drawing in" the polymer, allowing it to surround itself. This breakage of the linearity can be compared with *Figure 35*, an optimized structure of the PSMA hexamer. This agrees with the early findings where the 350 kDa, more flexible than 20 kDa, had an increased internalization<sup>138</sup>. This suggests, the flexibility of the polymer has a correlation with the binding and internalization of the polymer into the cell. Next, the binding and interaction energies of the optimized polymers were calculated and analyzed.

**Table 5.** Summary of binding and interaction energy using method #1

|                                     | FR $\alpha$<br>FA<br>pH 7.4 | FR $\alpha$<br>FA<br>pH 5.5 | FR $\alpha$<br>FA-DABA-<br>PSMA<br>pH 7.4 | FR $\alpha$<br>FA-DABA-<br>PSMA<br>pH 5.5 |
|-------------------------------------|-----------------------------|-----------------------------|---|---|
| Binding<br>Energy<br>(kcal/mol)     | -202.5                      | -267.8                      | -332.2                                    | -414.0                                    |
| Interaction<br>Energy<br>(kcal/mol) | -352.0                      | -466.5                      | -716.9                                    | -781.6                                    |

At pH 5.5, it was expected that the binding and interaction energy would be less than energies resulting from pH 7.4 or become a positive energy for the FA-FR $\alpha$  interaction. The positive value would indicate that the receptor and the ligand have dissociated. However, for both FA and FA-DABA-PSMA complex, the binding



energy increased despite the decrease in pH to 5.5. This could be due to a few possibilities. First, the water molecules are not present in the optimization calculation. The presence of water could alter the hydrogen bonding in the system. Second, similar to the first possibility, the environment of the complex is not identical to *in vivo* settings. Within the lysosome of a living cell, different aqueous compounds will interact with hydrogen protons that are pumped through the proton pump of the lysosome. In the simulations, five hydrogens are simply added to the amino acids that would be protonated at pH 5.5. However, in reality, the entire structure can collapse due to the change in the pH<sup>142</sup>. Third, due to the size of the complex, the degree of freedom increases exponentially. More than one possible optimized structure could be present, and the number of local minima in the potential energy surface would increase the complexity of the system significantly and would not allow an accurate result in the time allocated to the project. Furthermore, the energies found are much higher than expected. As an example, the oxygen-nitrogen hydrogen bond is -8.37 kcal/mol<sup>143</sup>. In the complex, there are multiple hydrogen bonds present along with hydrophobic interactions due to  $\pi$ - $\pi$  stacking interactions as seen in *Figure 24*. Thus, the energies observed could be justified due to multiple bonds between the receptor and the ligand.

Comparing the binding and interaction energy of FA and FA-DABA-PSMA at pH 7.4, the interaction energy reveals a higher energy compared to the binding energy can be observed. This increase could be due to the hydrophilic layer of the polymer interacting with the hydrophilic amino acids at the surface of the receptor, as previously mentioned. It should be noted that this is the energy obtained from the trimer of the polymer, yet in a full chain, the FA is attached to every 10<sup>th</sup> monomer of the polymer. If a full chain were modelled, there is a fair possibility that the hydrophilic chains would “wrap” the receptor, further increasing the binding energy. Often, the nanoparticles, such as micelles, become relatively rigid, preventing any transformation of their structure<sup>144</sup>. However, the FA-DABA-PSMA is fairly flexible with some mailability. When comparing the 350 kDa and 20 kDa, the longer 350 kDa chain showed more flexibility while the 20 kDa remained more rigid. This supports the previous finding where 20 kDa was seen remaining at the cytoplasm of the tumour cells, while the 350 kDa was able to transport into the nucleus of the tumour<sup>95</sup>.

The first method was a simulation completed to portray the release of the FA from pH 7.4 to pH 5.5. However, in the second method, instead of protonating an optimized pH 7.4 complex, the non-optimized pH 7.4 complex was protonated to pH 5.5 and optimized as pH 5.5 complex. The method of protonation, level of theory, functionals, basis sets, and charges were applied identically to the first method of calculation.

### 4.3.2. Method #2

#### 4.3.2.1. Interaction of FA with FR $\alpha$ optimized with 3-21G

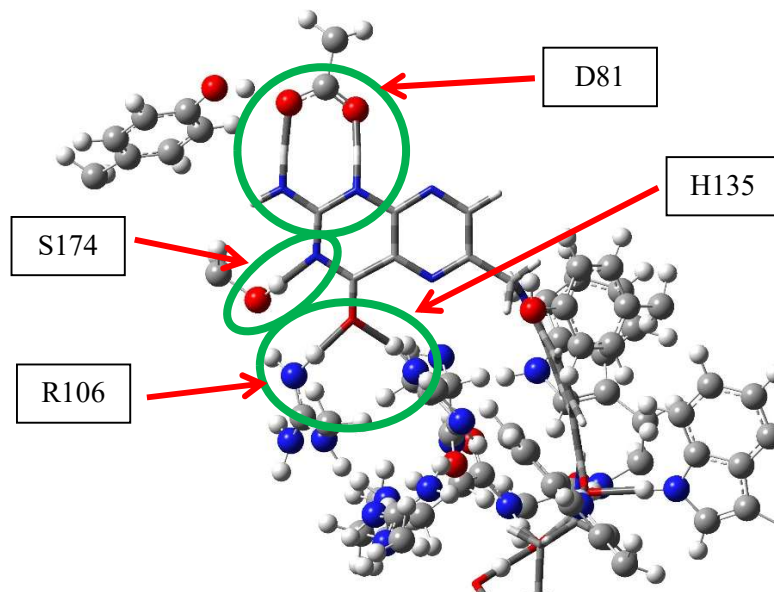


Figure 36. Hydrogen bonding between FA and amino acid (D81, R106, H135, and S174) in the FR $\alpha$  at pH 7.4. Optimized using DFT 3-21G

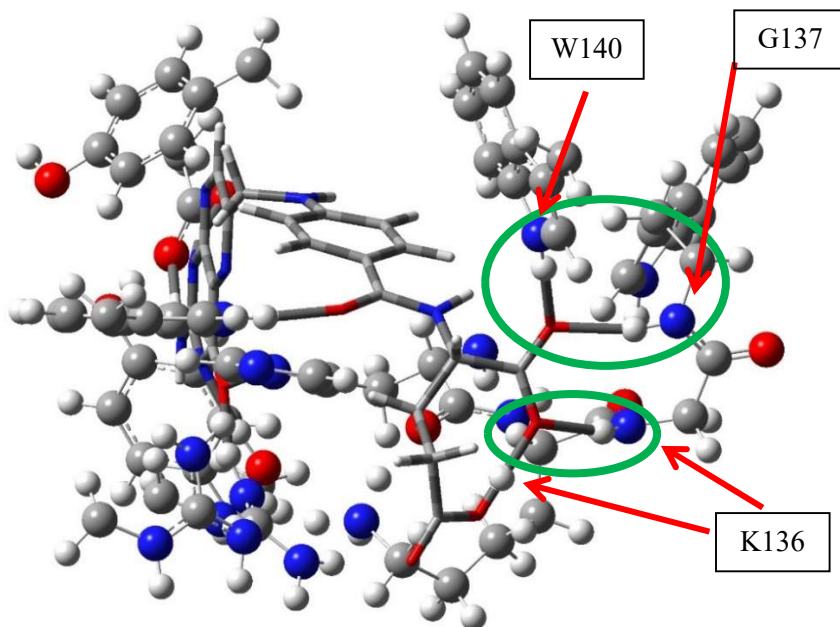


Figure 37. Hydrogen bonding between FA and amino acid (K136, G137, and W140) in the FR $\alpha$  at pH 7.4. Optimized using DFT 3-21G



**Table 6.** List of amino acids and interaction with FA at pH 7.4

| Abbreviation of the amino acid | Full name of the amino acid | Type of interaction with FA         | Bond length with FA |
|--------------------------------|-----------------------------|-------------------------------------|---------------------|
| Y60                            | Tyrosine - 60               | Hydrophobic: $\pi$ - $\pi$ stacking | N/A                 |
| D81                            | Aspartic Acid - 81          | Hydrogen bond                       | 1.61, 1.56          |
| Y85                            | Tyrosine - 85               | Hydrophobic: $\pi$ - $\pi$ stacking | N/A                 |
| W102                           | Tryptophan - 102            | No Bonding                          | No Bonding          |
| R103                           | Arginine - 103              | No Bonding                          | No Bonding          |
| R106                           | Arginine - 106              | Hydrogen bond                       | 1.62                |
| H135                           | Histidine - 135             | Hydrogen bond                       | 1.68                |
| K136                           | Lysine - 136                | No Bonding                          | No Bonding          |
| G137                           | Glycine - 137               | Hydrogen bond                       | 1.83                |
| W138                           | Tryptophan - 138            | Hydrogen bond                       | 1.95                |
| W140                           | Tryptophan - 140            | Hydrogen bond                       | 1.77                |
| W171                           | Tryptophan - 171            | Hydrophobic: $\pi$ - $\pi$ stacking | N/A                 |
| S174                           | Serine - 174                | Hydrogen bond                       | 1.81                |
| Y175                           | Tyrosine - 175              | Hydrophobic: $\pi$ - $\pi$ stacking | N/A                 |

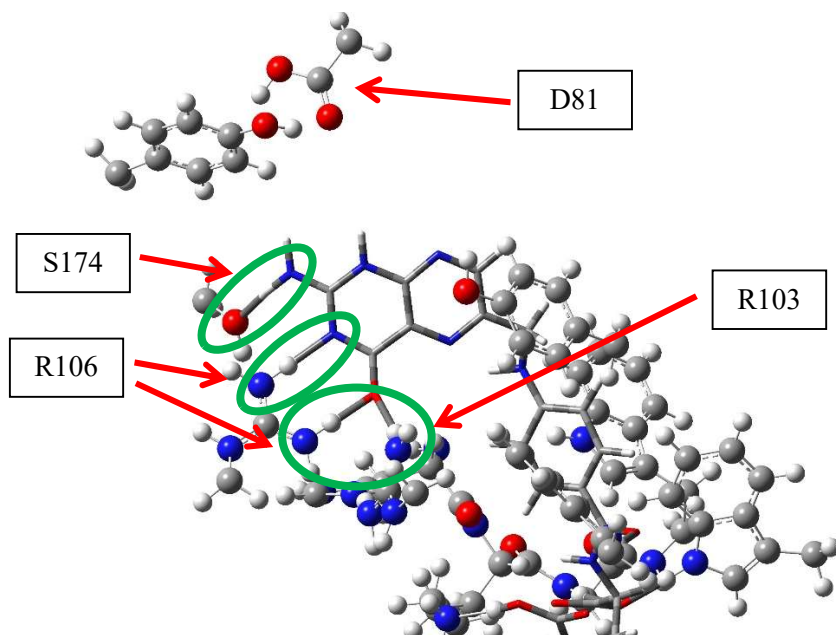


Figure 38. Hydrogen bonding between FA and amino acid (R103, R106, and S174) in the FR $\alpha$  at pH 5.5. Optimized using DFT 3-21G

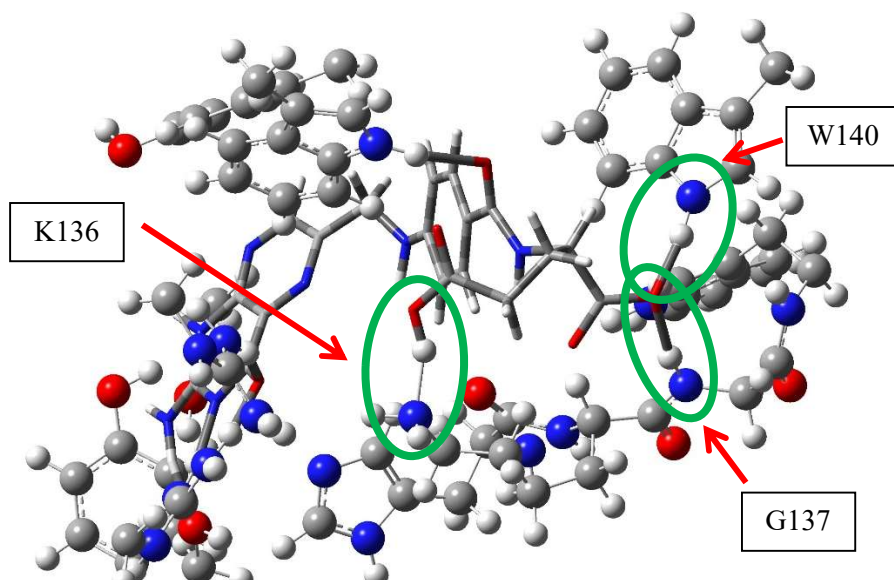


Figure 39. Hydrogen bonding between FA and amino acid (K136, G137, and W140) in the FR $\alpha$  at pH 5.5. Optimized using DFT 3-21G

**Table 7.** List of amino acids and interaction with FA at pH 5.5

| Abbreviation of the amino acid | Full name of the amino acid | Type of interaction with FA         | Bond length with FA           |
|--------------------------------|-----------------------------|-------------------------------------|-------------------------------|
| Y60                            | Tyrosine - 60               | Hydrophobic: $\pi$ - $\pi$ stacking | N/A                           |
| D81                            | Aspartic Acid - 81          | No Bonding                          | No Bonding                    |
| Y85                            | Tyrosine - 85               | Hydrophobic: $\pi$ - $\pi$ stacking | N/A                           |
| W102                           | Tryptophan - 102            | No Bonding                          | No Bonding                    |
| R103                           | Arginine - 103              | Hydrogen bond                       | 1.84                          |
| R106                           | Arginine - 106              | Hydrogen bond                       | 1.74 (N-H-N),<br>1.65 (N-H-O) |
| H135                           | Histidine - 135             | No Bonding                          | No Bonding                    |
| K136                           | Lysine - 136                | Proton Exchange                     | 1.06                          |
| G137                           | Glycine - 137               | Hydrogen bond                       | 1.86                          |
| W138                           | Tryptophan - 138            | No Bonding                          | No Bonding                    |
| W140                           | Tryptophan - 140            | Hydrogen bond                       | 1.72                          |
| W171                           | Tryptophan - 171            | Hydrophobic: $\pi$ - $\pi$ stacking | N/A                           |
| S174                           | Serine - 174                | Hydrogen bond                       | 1.72                          |
| Y175                           | Tyrosine - 175              | Hydrophobic: $\pi$ - $\pi$ stacking | N/A                           |

Optimization using method number #2 resulted in different structures compared to method number #1. First, in the pH 7.4 optimization, amino acid S174 can be seen forming a hydrogen bond with the nitrogen in the pterin ring. This formation was not observed in the previous figures. At pH 7.4, a hydrogen from K136 was drawn into the carboxylic group of the glutamate group of the FA. This hydrogen was indicated with a green arrow in *Figure 37*. After leaving the hydrogen, it moved to the inner pocket of the receptor to form a hydrogen bond with R103. Earlier, protonation of the receptor to pH 5.5 showed that the hydrogen added to D81 repelled away from the pterin ring, but the carboxylic group of D81 remained, forming a hydrogen bond with the nitrogen of the pterin group. In contrast, as *Figure 38* suggests, the D81 here completely moved away from the pterin, without any formation of a hydrogen bond with the pterin ring of the FA. This is indeed the expected movement when protonation of the receptor occurs. However, amino acids R103, R106, and S174 formed hydrogen bonds despite the decrease in pH, as depicted in *Figure 39* and this could be due to the lack of protons existing in the FR $\alpha$  pocket. Next, the structures were optimized using 6-31G\*\* (d,p) to determine if the polarization of the basis set would alter the formation of the hydrogen bonds between the FR $\alpha$  and FA.

#### 4.3.2.2. Interaction of FA with FR $\alpha$ optimized using 6-31G\*\*

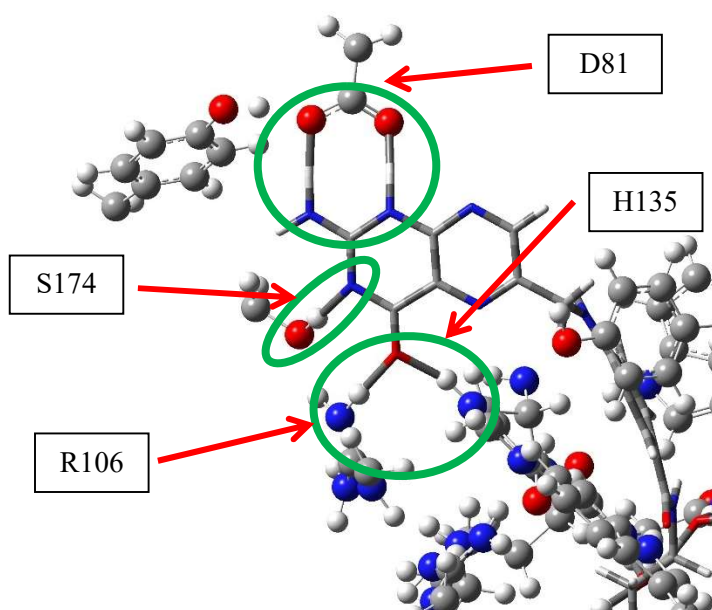


Figure 40. Hydrogen bonding between FA and amino acid (D81, R106, S174, and H135) in the FR $\alpha$  at pH 7.4. Optimized using DFT 6-31G\*\*

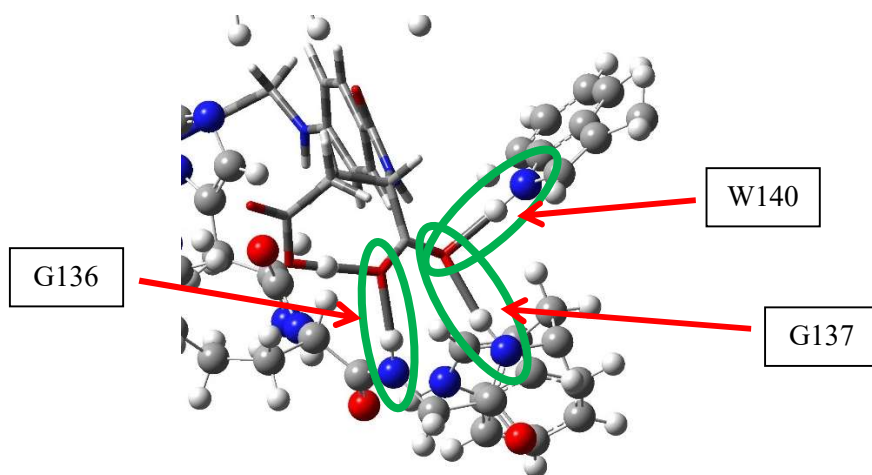


Figure 41. Hydrogen bonding between FA and amino acid (G137, K137, and W140) in the FR $\alpha$  at pH 7.4. Optimized using DFT 6-31G\*\*

**Table 8.** List of amino acids and interaction with FA at pH 7.4

| Abbreviation of the amino acid | Full name of the amino acid | Type of interaction with FA         | Bond length with FA |
|--------------------------------|-----------------------------|-------------------------------------|---------------------|
| Y60                            | Tyrosine - 60               | Hydrophobic: $\pi$ - $\pi$ stacking | N/A                 |
| D81                            | Aspartic Acid - 81          | Hydrogen bond                       | 1.55, 1.61          |
| Y85                            | Tyrosine - 85               | Hydrophobic: $\pi$ - $\pi$ stacking | N/A                 |
| W102                           | Tryptophan - 102            | No Bonding                          | No Bonding          |
| R103                           | Arginine - 103              | Hydrogen bond                       | N/A                 |
| R106                           | Arginine - 106              | Hydrogen bond                       | 1.62                |
| H135                           | Histidine - 135             | Hydrogen bond                       | 1.68                |
| K136                           | Lysine - 136                | No Bonding                          | No Bonding          |
| G137                           | Glycine - 137               | Hydrogen bond                       | 1.83                |
| W138                           | Tryptophan - 138            | Hydrogen bond                       | 1.95                |
| W140                           | Tryptophan - 140            | Hydrogen bond                       | 1.77                |
| W171                           | Tryptophan - 171            | Hydrophobic: $\pi$ - $\pi$ stacking | N/A                 |
| S174                           | Serine - 174                | Hydrogen bond                       | 1.85                |
| Y175                           | Tyrosine - 175              | Hydrophobic: $\pi$ - $\pi$ stacking | N/A                 |

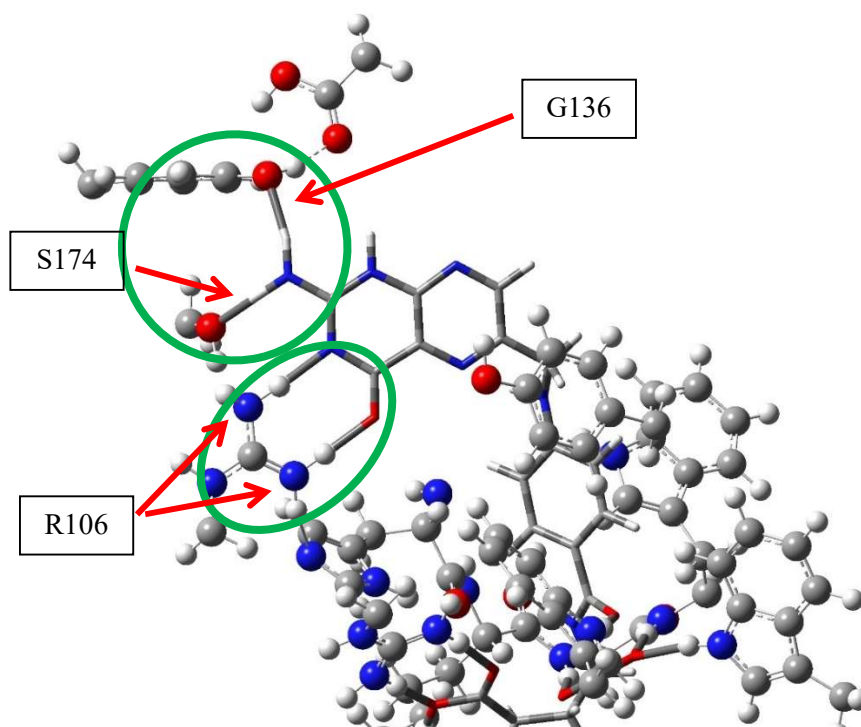


Figure 42. Hydrogen bonding between FA and amino acid (R103, S174, and Y175) in the FR $\alpha$  at pH 5.5. Optimized using DFT 6-31G\*\*

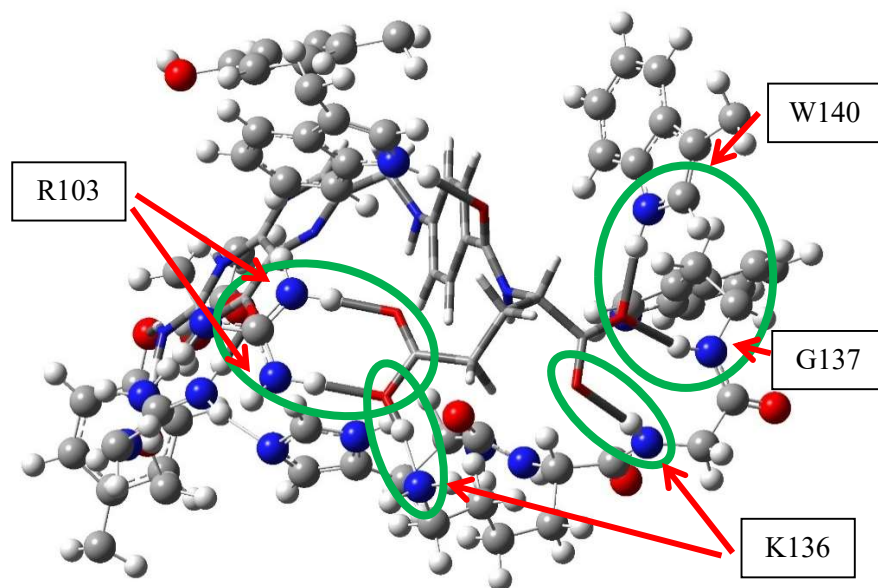


Figure 43. Hydrogen bonding between FA and amino acid (R103, K136, G137, and W140) in the FR $\alpha$  at pH 5.5. Optimized using DFT 6-31G\*\*

**Table 9.** List of amino acids and interaction with FA at pH 5.5

| Abbreviation of the amino acid | Full name of the amino acid | Type of interaction with FA                         | Bond length with FA          |
|--------------------------------|-----------------------------|---|------------------------------|
| Y60                            | Tyrosine - 60               | Hydrophobic: $\pi$ - $\pi$ stacking                 | N/A                          |
| D81                            | Aspartic Acid - 81          | No Bonding  | No Bonding                   |
| Y85                            | Tyrosine - 85               | Hydrophobic: $\pi$ - $\pi$ stacking                 | N/A                          |
| W102                           | Tryptophan - 102            | No Bonding  | No Bonding                   |
| R103                           | Arginine - 103              | Hydrogen bond                                       | 1.76, 1.84                   |
| R106                           | Arginine - 106              | Hydrogen bond                                       | 1.81 (N-H-N)<br>1.72 (N-H-O) |
| H135                           | Histidine - 135             | No Bonding  | No Bonding                   |
| K136                           | Lysine - 136                | Proton Exchange                                     | 1.04                         |
| G137                           | Glycine - 137               | Hydrogen bond                                       | 2.02                         |
| W138                           | Tryptophan - 138            | No Bonding  | No Bonding                   |
| W140                           | Tryptophan - 140            | Hydrogen bond                                       | 1.85                         |
| W171                           | Tryptophan - 171            | Hydrophobic: $\pi$ - $\pi$ stacking                 | N/A                          |
| S174                           | Serine - 174                | Hydrogen bond                                       | 1.85                         |
| Y175                           | Tyrosine - 175              | Hydrophobic: $\pi$ - $\pi$ stacking / Hydrogen Bond | 1.91                         |

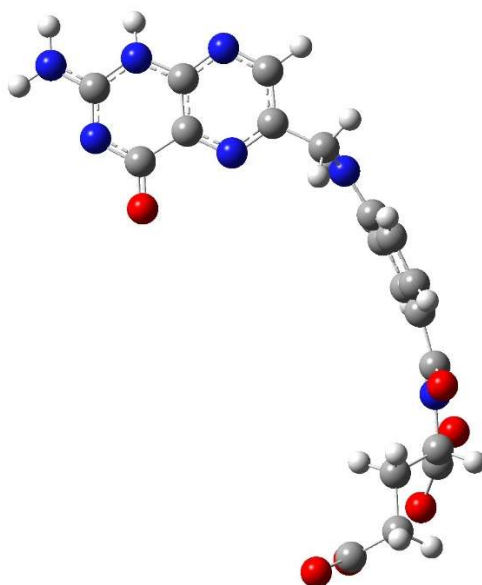


Figure 44. The structure of FA at pH 7.4 from the FR $\alpha$  complex. The complex was optimized using basis set 6-31G\*\*.

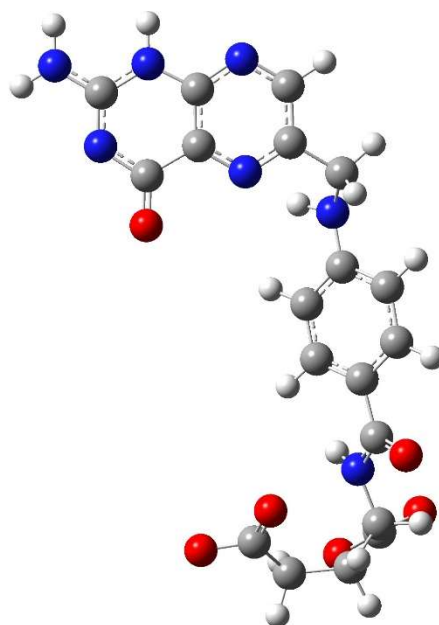


Figure 45. The structure of FA at pH 5.5 from the FR $\alpha$  complex. The complex was optimized using basis set 6-31G\*\*.



Changes in hydrogen bonds formation or length were not observed for the FA with FR $\alpha$  at pH 7.4, optimized using a 6-31G\*\* basis set when compared to the 3-21G optimized complex. Conversely, at pH 5.5, for the first time, the pterin ring of the FA was seen forming a hydrogen bond with amino acid Y175, an amino acid that is supposed to be interacting with the pterin ring through hydrophobic interactions seen from *Figure 40*. From previous figures, R103 was seen interacting exclusively with oxygen in the pterin ring of FA. Yet, the glutamate group of the FA exerted severe torsion inwards to the receptor, forming two hydrogen bonds with R103 as seen in *Figure 43*. The torsion of the FA can be compared between *Figure 44* and *Figure 45* where the change in dihedral angle of the aminobenzoate and glutamate group can be observed. The dihedral angle between the pterin group and the aminobenzoate group was -144.2° for pH 7.4 FA and -123.0° for pH 5.5 FA. The dihedral angle of the glutamate group was -121.0° for pH 7.4 FA and -83.6° for pH 5.5 FA. This significant change in the dihedral angles of the FA suggests that the receptor is heavily hindering the most stable structure of the FA due to a change in the pH. This could be an intermediate complex structure of the FA release from the FR $\alpha$  with the head, pterin group pulling away from the pocket of the receptor. *In vitro*, a constant proton pump would push the protons in the caveolae to create an acidic environment<sup>145</sup>. Thus, with the presence of excessive hydrogens, the glutamate group of the FA may interact with these hydrogens instead of receptors and formulate a release. The binding energy and interaction energy of the complex using two different basis sets were calculated.

**Table 10.** Summary of binding and interaction energy between FA and FR $\alpha$  using method # 2, 3-21G vs 6-31G\*\*

|                                     | FR $\alpha$<br>FA<br>pH 7.4<br>3-21G | FR $\alpha$<br>FA<br>pH 5.5<br>3-21G | FR $\alpha$<br>FA<br>pH 7.4<br>6-31G** | FR $\alpha$<br>FA<br>pH 5.5<br>6-31G** |
|-------------------------------------|--------------------------------------|--------------------------------------|--|--|
| Binding<br>Energy<br>(kcal/mol)     | -475.8                               | -515.4                               | -410.4                                 | -408.0                                 |
| Interaction<br>Energy<br>(kcal/mol) | -616.91                              | -598.23                              | -574.3                                 | -582.2                                 |

From calculation method #2, unlike the previous method, a decrease in interaction energy for the FA complex was seen when the pH was lowered. Yet, the overall binding and interaction energy of complex optimization using 3-21G were significantly higher than the previous method, *Table 1*. The 6-31G\*\* basis set provided more flexibility in the polarized system and is often chosen for accurate representation and modeling of H-bonded system<sup>146,147</sup>. Comparing the 3-21G results, it's interesting to note that the pH 5.5 complex had higher binding energy compared to the pH 7.4 complex, yet a slight decrease in interaction energy was observed. For 6-31G\*\* optimization, while the binding energy was nearly identical, with pH 5.5

complex 2.4 kcal/mol decreased from pH 7.4 complex, the interaction energy saw a slight increase. This could be representative of the structure reorientation of the receptor to allow binding. Through calculation using method #2, although major structural changes were observed, the release of the FA, a significant decrease in the binding energy, or a positive binding energy couldn't be achieved. Next, optimization using FA-DABA-PSMA was completed to compare with method #1.

#### 4.3.2.3. Interaction of FA-DABA-PSMA with FR $\alpha$

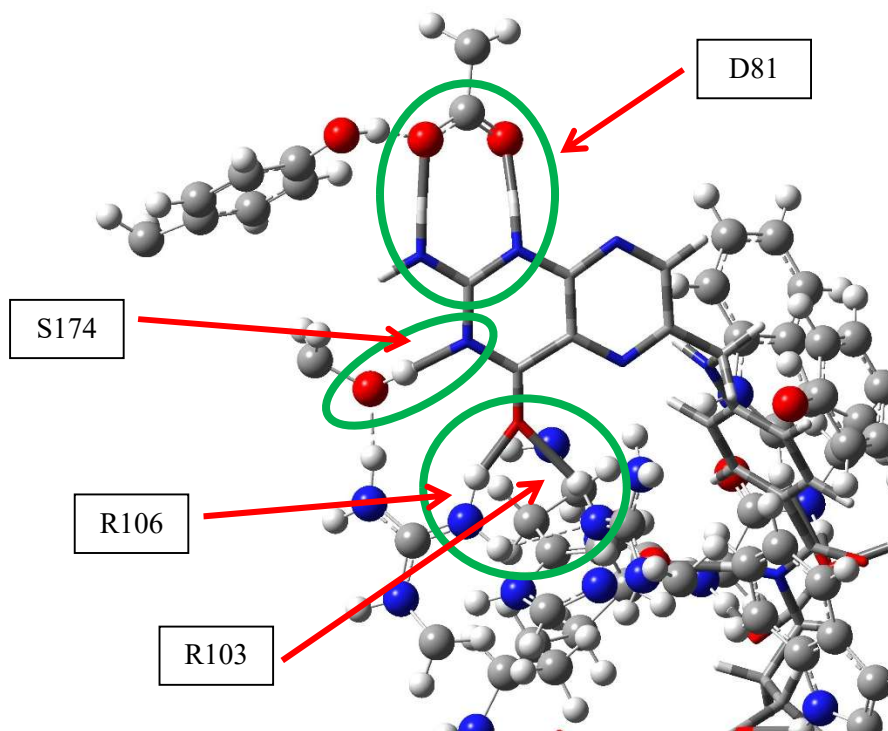


Figure 46. Hydrogen bonding between FA-DABA-PSMA and amino acid (D81, R103, R106, and S174) in the FR $\alpha$  at pH 7.4. Optimized using DFT 3-21G

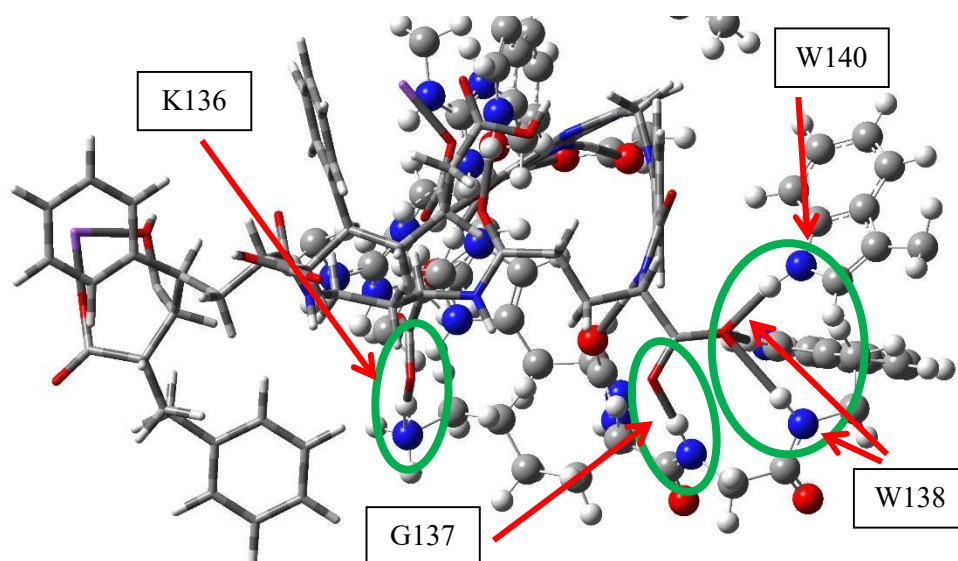


Figure 47. Hydrogen bonding between FA-DABA-PSMA and amino acid (K136, G137, W138, and W140) in the FR $\alpha$  at pH 7.4. Optimized using DFT 3-21G

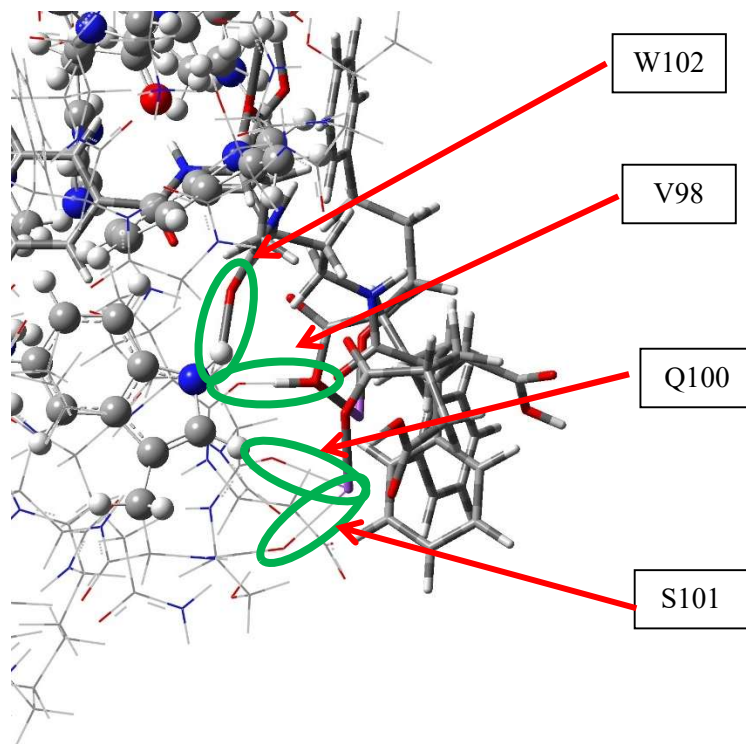


Figure 48. Hydrogen bonding between FA-DABA-PSMA and amino acid (V98, Q100, S101, and W102) in the FR $\alpha$  at pH 7.4. Optimized using DFT 3-21G

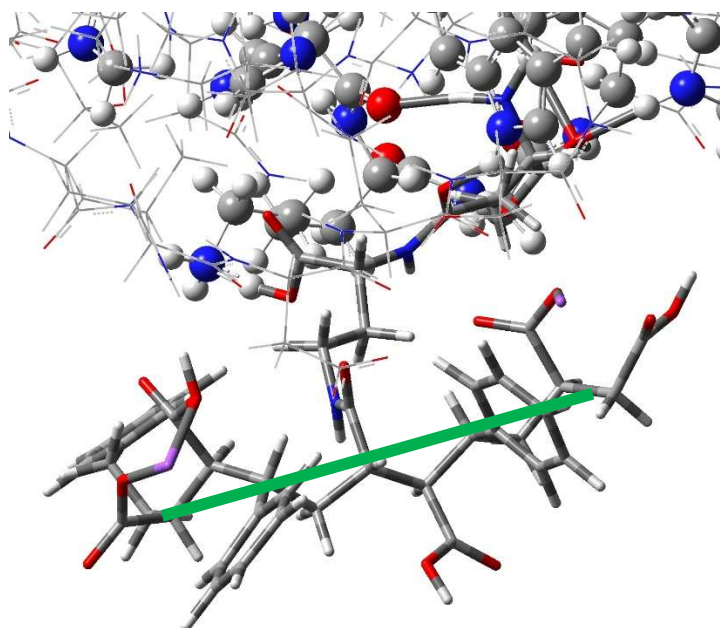


Figure 49. Top view of the PSMA chain with a green line to present the bending of the polymer backbone

**Table 11.** List of amino acids and interaction with FA-DABA-PSMA at pH 7.4

| Abbreviation of the amino acid | Full name of the amino acid | Type of interaction with FA         | Bond length with FA-DABA-PSMA |
|--------------------------------|-----------------------------|-------------------------------------|-------------------------------|
| Y60                            | Tyrosine - 60               | Hydrophobic: $\pi$ - $\pi$ stacking | N/A                           |
| D81                            | Aspartic Acid - 81          | Hydrogen bond                       | 1.57, 1.62                    |
| Y85                            | Tyrosine - 85               | Hydrophobic: $\pi$ - $\pi$ stacking | N/A                           |
| V98                            | Valine - 98                 | Hydrogen bond                       | 2.18                          |
| Q100                           | Glutamine - 100             | Hydrogen bond                       | 2.29                          |
| S101                           | Serine - 101                | Hydrogen bond                       | 2.38                          |
| W102                           | Tryptophan - 102            | Hydrogen bond                       | 1.78                          |
| R103                           | Arginine - 103              | Hydrogen bond                       | 2.02                          |
| R106                           | Arginine - 106              | Hydrogen bond                       | 1.59                          |
| H135                           | Histidine - 135             | No Bonding                          | No Bonding                    |
| K136                           | Lysine - 136                | Proton Exchange                     | 1.14                          |
| G137                           | Glycine - 137               | Hydrogen bond                       | 1.55                          |
| W138                           | Tryptophan - 138            | Hydrogen bond                       | 2.33                          |
| W140                           | Tryptophan - 140            | Hydrogen bond                       | 1.83                          |

|      |                  |                                     |      |
|------|------------------|-------------------------------------|------|
| W171 | Tryptophan - 171 | Hydrophobic: $\pi$ - $\pi$ stacking | N/A  |
| S174 | Serine - 174     | Hydrogen bond                       | 1.74 |
| Y175 | Tyrosine - 175   | Hydrophobic: $\pi$ - $\pi$ stacking | N/A  |

Few notable changes from optimization method #2 were seen in contrast to method #1. First, from *Figure 27*, amino acid S174 did not form a hydrogen bond with the nitrogen from the pterin group of FA-DABA-PSMA while the optimization using the 2nd method allowed the H-bond formation as *Figure 46* depicts. Another notable change is the number of hydrogen bonds the PSMA chain was able to form with the hydrophilic groups of the receptor. Method #1 chains formed two hydrogen bonds with D99 and K136 amino acids, *Figure 29*, while method #2 formed four hydrogen bonds with amino acids V98, Q100, S101, and W102 as seen in *Figure 48*. This increase in hydrogen bonding agrees with the binding energy difference between method #1 and method #2, which will be discussed below. The trimer of the polymer chain remained linear, which is the same observation seen with method #1. The linearity of the polymer is an important factor in its efficiency to transporting the drug inside the cell<sup>95</sup>. From optimization using two methods, a common ground is found where the hydrophilic maleic acid of the polymer chain interacts strongly with the amino acids of the receptor. Next, optimized structures of FA-DABA-PSMA at pH 5.5 using a 3-21G basis set will be discussed and compared to method #1.

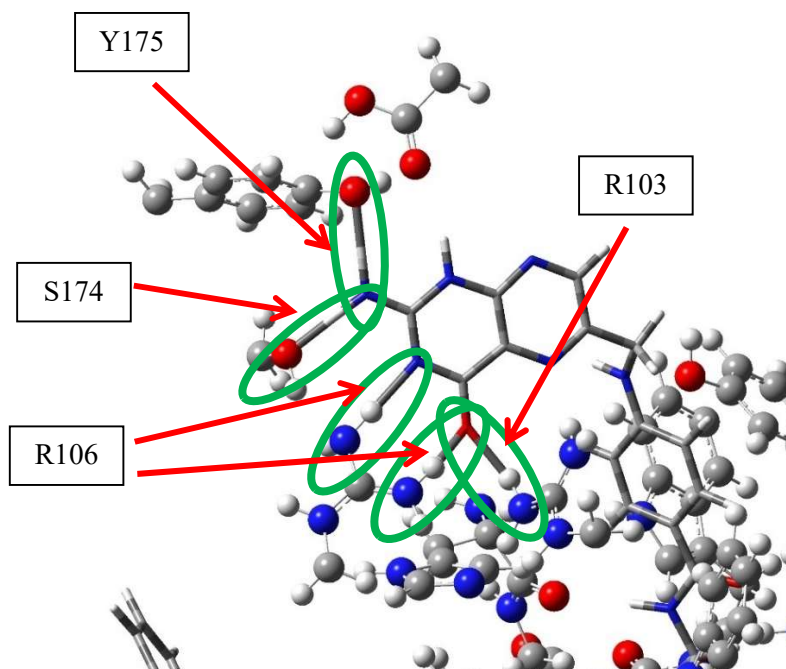


Figure 50. Hydrogen bonding between FA-DABA-PSMA and amino acid (R103, R106, and S174) in the FR $\alpha$  at pH 5.5. Optimized using DFT 3-21G

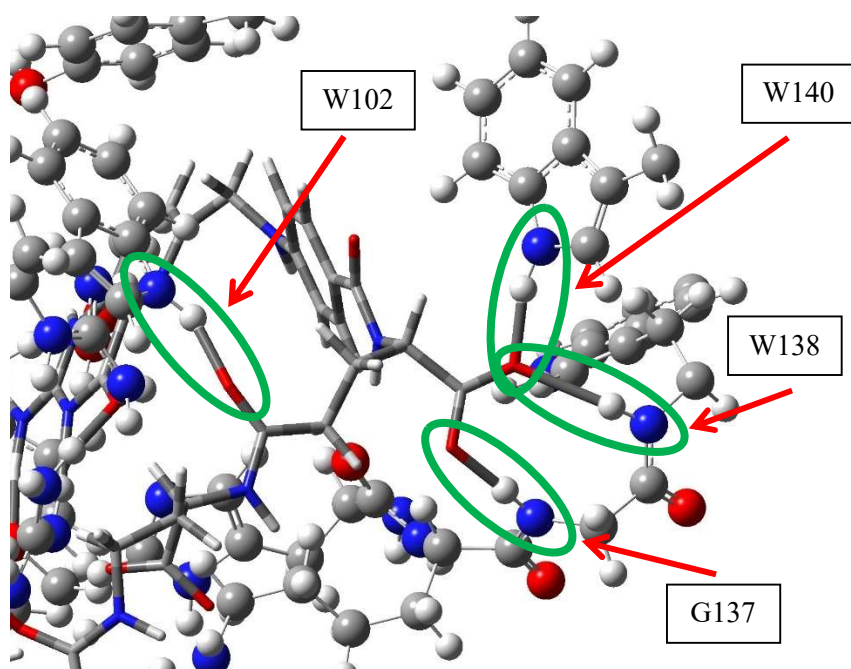


Figure 51. Hydrogen bonding between FA-DABA-PSMA and amino acid (W102, G137, W138, AND W140) in the FR $\alpha$  at pH 5.5. Optimized using DFT 3-21G

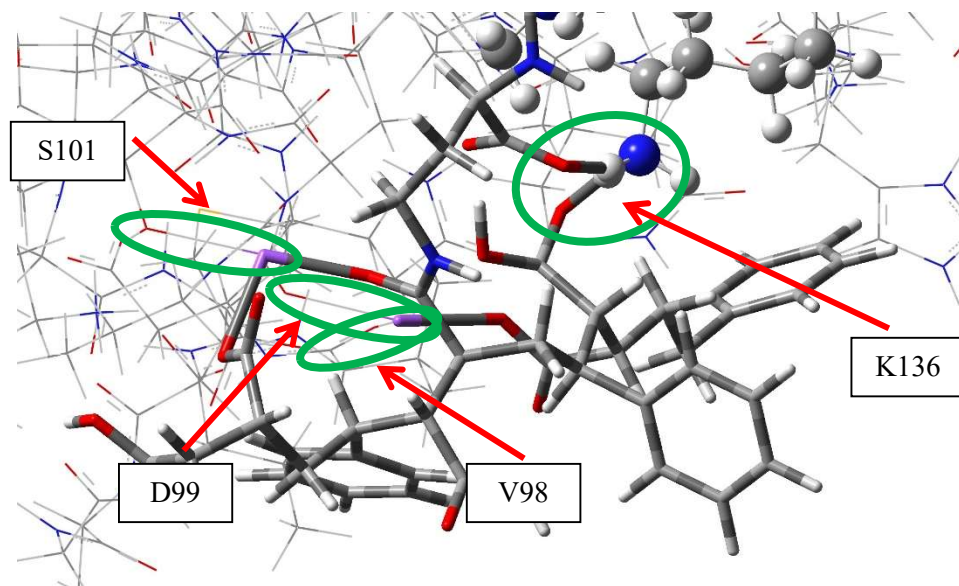


Figure 52. Hydrogen bonding between PSMA and amino acid (V98, D99, S101, and K136) in the FR $\alpha$  at pH 5.5. Optimized using DFT 3-21G



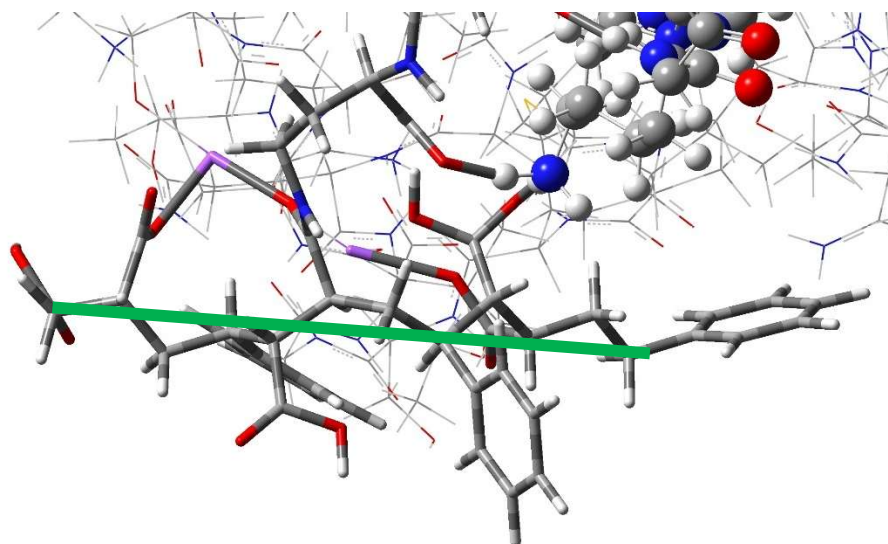


Figure 53. Top view of the FA-DABA-PSMA chain at pH 5.5 with a green line to present the bending of the polymer backbone

**Table 12.** List of amino acids and interaction with FA-DABA-PSMA at pH 5.5

| Abbreviation of the amino acid | Full name of the amino acid | Type of interaction with FA         | Bond length with FA-DABA-PSMA |
|--------------------------------|-----------------------------|-------------------------------------|-------------------------------|
| Y60                            | Tyrosine - 60               | Hydrophobic: $\pi$ - $\pi$ stacking | N/A                           |
| D81                            | Aspartic Acid - 81          | No bond                             | No bond                       |
| V98                            | Valine - 98                 | Hydrogen bond                       | 2.37                          |
| D99                            | Aspartic Acid - 99          | Hydrogen bond                       | 2.31                          |
| S101                           | Serine - 101                | Hydrogen bond                       | 2.40                          |
| Y85                            | Tyrosine - 85               | Hydrophobic: $\pi$ - $\pi$ stacking | N/A                           |
| W102                           | Tryptophan - 102            | Hydrogen bond                       | 1.75                          |
| R103                           | Arginine - 103              | Hydrogen bond                       | 1.82                          |
| R106                           | Arginine - 106              | Hydrogen bond                       | 1.83 (N-H-N)<br>1.60 (N-H-O)  |
| H135                           | Histidine - 135             | No bond                             | No bond                       |
| K136                           | Lysine - 136                | Hydrogen bond                       | 1.50, 1.53                    |
| G137                           | Glycine - 137               | Hydrogen bond                       | 1.60                          |
| W138                           | Tryptophan - 138            | Hydrogen bond                       | 2.28                          |

|      |                  |   |      |
|------|------------------|---|------|
| W140 | Tryptophan - 140 | Hydrogen bond                                       | 1.69 |
| W171 | Tryptophan - 171 | Hydrophobic: $\pi$ - $\pi$ stacking                 | N/A  |
| S174 | Serine - 174     | Hydrogen bond                                       | 1.66 |
| Y175 | Tyrosine - 175   | Hydrophobic: $\pi$ - $\pi$ stacking / Hydrogen Bond | 1.79 |

The repulsion of amino acid D81, an important amino acid that binds strongly with the nitrogen of the pterin group, was seen repelling away due to protonation, which was observed earlier in *Figure 40* when method #2 was used for optimization. In contrast, when optimized with method #1, as seen in *Figure 30*, the pterin ring was able to form two hydrogen bonds with the D81 amino acid. With method #2, interestingly, instead of forming a hydrogen bond with D81, a hydrogen bond was formed with Y175 an amino acid that is expected to only have a hydrophobic interaction with the pterin ring as depicted in *Figure 50*. A hydrogen bond was also formed with S174, which is consistent with pH 7.4 findings but different from method #1. It is interesting to note that while method #1 had six hydrogen bonds between the maleic acid groups of the polymer and amino acids of the receptor, D99, Q100, S101, and G137 as seen from *Figure 33*. The method #2 had five hydrogen bonds with amino acid V98, D99, S101, and K136 from the receptor, *Figure 52*. Comparing findings from pH 5.5 using method #2 to pH 7.4 of method #2, W102, which forms hydrogen bonding with the polymer, was replaced with K136 as seen in *Figure 52*. This suggests that the receptor is undergoing conformational change due to the change in pH. In contrast to method #1, in method #2, bending of the polymer backbone was not observed as seen in *Figure 53*. Despite the linearity of the chain, a multiple formation of hydrogen bonds between the maleic acid of the polymer and amino acids of the receptor suggests that the FA-DABA-PSMA can remain strongly bonded to FR $\alpha$  even with a decrease in pH. Next, the binding and interaction energies will be compared.

**Table 13.** Summary of binding and interaction energy between FA-DABA-PSMA and FR $\alpha$  using method # 2, 3-21G

|                                  | FR $\alpha$<br>FA-DABA-PSMA<br>pH 7.4<br>3-21G | FR $\alpha$<br>FA-DABA-PSMA<br>pH 5.5<br>3-21G |
|----------------------------------|--|--|
| Binding Energy<br>(kcal/mol)     | -559.1   | -592.5   |
| Interaction Energy<br>(kcal/mol) | -1716.6  | -805.9   |



In agreement with early findings from *Table 5*, an increase in both the binding and interaction energy was observed with the FA-DABA-PSMA complex for pH 5.5 and 7.4 complex. The pH 5.5 complex had a lower interaction energy compared to pH 7.4 complex, while the binding was higher. This finding may suggest and agree with our early findings where the decrease in pH doesn't allow the release of FA-DABA-PSMA from the receptor due to hydrogen bonding between the PSMA and the receptor. The overall binding and interaction energy using method #2 was higher than method #1, and this increase could be due to a stronger interaction between the maleic acid and hydrophilic AAs. Comparing the method #2 FA-DABA-PSMA results to previous FA results, a significant binding energy increase was not observed; however, the interaction energy was seen to increase significantly. This suggests that when FA-DABA-PSMA binds to the receptor, it has a very strong interaction with hydrophilic AAs, which is a constant finding seen previously.

#### 4.4. Conclusion

Through computational modeling and optimization, optimized structures were obtained, and hydrogen bonds between the FA / FA-DABA-PSMA ligand with AAs of the FR $\alpha$  were measured and analyzed. The energies obtained from the optimized structures were used to find the binding and interaction energy between the ligand and the receptor. Through the simulations, it was determined that the simulations were not able to successfully simulate the complete release of the FA / FA-DABA-PSMA from the FR $\alpha$ . The binding and interaction energies obtained also couldn't depict the release of the ligand, as positive energy was not achieved. Here, a positive energy binding energy between the ligand and the receptor would indicate no binding between the two. However, an increase in binding and interaction was observed when FA-DABA-PSMA was replaced the FA with the FR $\alpha$ . Multiple hydrogen bond formation was seen between the maleic acid of the PSMA and hydrophilic AAs of the receptors, which contributed to the increase the energies. The polymer chain was also seen bending towards to receptor, surrounding it. This agrees with the early finding in the studies where the rigidity of the polymer altered the results. The overall finding suggests multiple hydrogen bond formation can be made between the PSMA chains and the receptor, and at pH 5.5, the FA-DABA-PSMA may not be able to be released from the FR $\alpha$ .

The computational study provided essential information on the electronic interaction occurring between the receptor and FA when attached to the polymer, predicting potential higher interaction through hydrogen bonding. These interactions could influence the pH-controlled release of FA in cancer cells. However, computational studies do not take into account solvent effect, ionic strength, or the complexity of the cellular environment. This can be directly related to the functionals, basis set, lack of solvation model, and lack of dispersion correction. The computational method used for this study is based on gas model of the atoms and their behaviour as a gas state. As a result, it creates a distortion between the theoretical model and real model which would be observed *in vitro* or *in vivo*. This

distortion may explain the negative energy found between FA and FR $\alpha$  in pH 5.5. Here, a positive binding energy was expected however, despite the protonation, it yielded a negative energy. This may be due to the missing parameters to successfully simulate the release ligand. Addition of solvation model and or dispersion correction may yield more accurate results yet, due to resource and time it requires to calculate such model, it is not realistic with the degree of freedom the FR $\alpha$  possesses. Therefore, for a complete understanding of the interaction, an experimental characterization will be presented in the next chapter.

## **5. Microscale Thermophoresis**

### **5.1. Introduction**

The debate of accuracy between theoretical calculation and experimental results will always be present due to the limitations of both methods. To compensate for the limitations, a comparison between the theoretical and experimental is a must to successfully conclude if the findings are indeed accurate and consistent. Finding the binding affinity between a receptor and ligand can be completed in multiple ways. For the purpose of this study, microscale thermophoresis was selected as the instrument due to the ease of sample preparation and instrument performance.

### **5.2. Methods**

#### **FA-DABA-PSMA Synthesis**

FA-DABA-PSMA 350 kDa and 20 kDa were synthesized according to Li et al<sup>62</sup>. 0.27586 mg of freeze-dried sample was added to 5 mL of pH 7.5 adjusted ultrapure water to a final concentration of 200  $\mu$ M. The sample was sonicated for 5 minutes and mixed overnight using a plate shaker.

#### **Expression and Purification**

The human folate receptor alpha plasmid (hFR $\alpha$ ) was a gift from Karsten Melcher (Addgene plasmid # 177841; [http://n2t.net/addgene:177841;RRID:Addgene\\_177841](http://n2t.net/addgene:177841;RRID:Addgene_177841)). A stable HEK293 cell line was generated. DMEM media was supplemented with 5% fetal bovine serum, 20 mM HEPES, and 5 $\mu$ M kifunensine. Media was changed and collected every four days. The collected media was then dialyzed against Folic Acid buffer (25 mM Tris, pH 8.0 150 NaCl) for 3 days, changing the buffer every 24 hours. Following dialysis, the sample was subject to size exclusion chromatography (SEC) on a Superdex 75 Increase GL 10/300 via an AKTA pure FPLC with a flow rate of 0.5mL/min in a Protein Labeling buffer (0.1M sodium bicarbonate, pH 9.0).

#### **FITC Labelling**

Post SEC, the protein was concentrated to 2 mg/ml and labeled with Fluorescein isothiocyanate, FITC. FITC was dissolved to 1 mg/ml in DMSO and added in 5 $\mu$ L increments to 50  $\mu$ L. The solutions were incubated in the dark at 4°C for 12 hours. The reaction was quenched by adding ammonium chloride to a final concentration of 50 mM followed by a 2-hour incubation at 4°C in the dark. SEC using a Superdex 200 GL 10/300 and a flow rate of 0.4mL/min was used to remove the excess dye and salts and separate hFR $\alpha$  protein into the binding buffer (20mM

HEPES, pH 7.0, 150mM NaCl, 5% glycerol). hFR $\alpha$  was then concentrated to 8.5  $\mu$ M for downstream experiments.

### **Microscale thermophoresis**

A 2-fold serial dilution was performed on the FA-DABA-PSMA, either 350kDa or 20kDa, where the highest concentration in the assay was 5 and 1  $\mu$ M, respectively. A constant amount of fluorescently labelled protein target, hFR $\alpha$  was added to each serial diluted polymer solution resulting to a final concentration of 25 nM. Mixtures were incubated at room temperature in the dark for 25 minutes and then loaded into a Nanotemper Technologies Monolith® NT.115 instrument using standard capillaries. After loading mixtures in the standard capillaries, 7.5  $\mu$ L of pH 5.5 buffer (20 mM MES, pH 5.5, 150 mM NaCl, 5% glycerol) was added to the tube. This changed the highest concentration of 350kDa and 20kDa polymer to 2.5  $\mu$ M and 500nM, respectively, while also lowering the hFR $\alpha$  Concentration to 12.5 nM.

Loaded into standard capillaries after thermophoresis was measured at room temperature (25°C) and performed using 70% excitation power along with medium IR-Laser power. Initial fluorescence migration was measured from -1.0 to 0 s and used to normalize the measured fluorescent migration time (14.0 to 15.0 s). Three independent replicates were analyzed using MO. Affinity Analysis software v2.1.3 and fit to the standard KD fit model, which describes a 1:1 stoichiometric molecular interaction according to the law of mass action. The dissociation constant ( $K_d$ ) is estimated by equation describe in chapter 3. The data obtained was fitted through non-linear regression using GraphPad Prism (version 10.0.0 for Windows, GraphPad Software, Boston, Massachusetts USA).

## **5.3. Results and Discussion**

### **Declaration**

This study was performed in collaboration with Scott Tersteeg from Dr. Trushar Patel's lab at Lethbridge Alberta. The protein expression, purification and FITC labeling was performed by Scott while the MST was performed together.

### **MST results**

The binding energy of using the MST was able to provide a valuable answer. A strong FR $\alpha$  – FA / FA-DABA-PSMA interaction would hinder the release of the ligands. Due to the limitation of the instrument, the binding energy between FA and FR $\alpha$  couldn't be unobtained. However, previous studies have determined the  $K_d < 1$  nM between FA and FR $\alpha$ <sup>148–150</sup>. Subsequently, a study with a similar procedure was able to determine  $K_d$  to be  $10.2 \pm 4.3$  nM between FA and FR $\alpha$  however, the Nanotemper Technologies Monolith® NT.115 pico instrument, which has a higher sensitivity, was used<sup>151</sup>. The referenced studies were performed using different

procedures and instruments and therefore will not be compared to the study but only used as a reference guide. This method looks at the concentration of FA needed to bind  $\frac{1}{2}$  of the receptors. However, not every FA on the SMA will be at the correct distance to bind to each FR $\alpha$ . For free FA, it should be able to freely bind to FR $\alpha$  while FA-DABA-PSMA may not be able to. Thus, a direct comparison between free FA and FA-DABA-PSMA can't be made. However, comparison between 20 kDa and 350 kDa can be made. For this study, samples were initially prepared at pH 7.5, then pH 5 MES buffer was added to the samples to simulate to create an acidic environment inside the cancer cells and the potential release of the ligands. First, the binding affinity of FA-DABA-PSMA 350 kDa and 20 kDa at pH 7.5 was obtained to compare the binding affinity between the 350 kDa and 20 kDa and with FA.

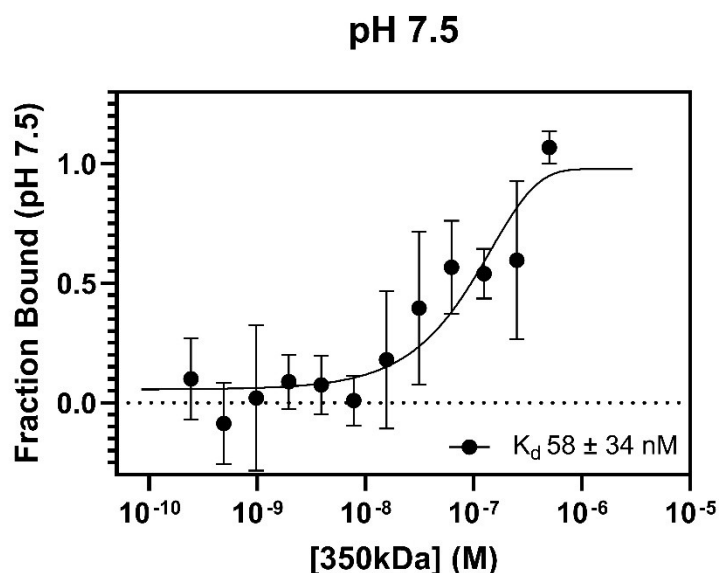


Figure 54. Binding affinity curve of FA-DABA-PSMA 350 kDa at pH 7.5

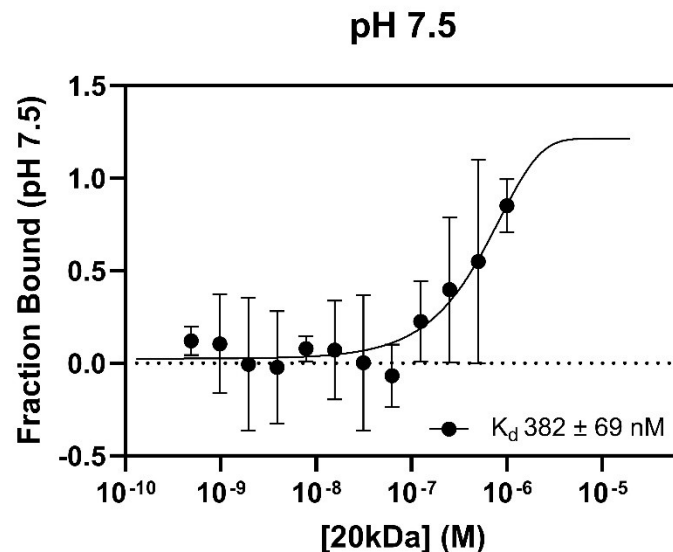


Figure 55. Binding affinity curve of FA-DABA-PSMA 20 kDa at pH 7.5

The FA-DABA-PSMA 350 kDa had binding affinity of  $58 \pm 34$  nM, *Figure 54*. This is relatively high binding affinity as in comparison to methotrexate, a chemotherapy agent that is very similar to FA in structure, the binding affinity similar<sup>152</sup>. The 20 kDa FA-DABA-PSMA revealed a lower affinity for FR $\alpha$  with an increase in  $K_d$  to  $382 \pm 69$  nM, *Figure 55*. This increase in  $K_d$  highlights the weaker interaction observed between the 20 kDa functional polymer and cancer cells in previous studies. Indeed, superior results of 350 kDa in reducing the cell viability of a cancer DU-145 *in vitro* compared to 20 kDa were reported<sup>63</sup>. In addition, a previous study visually confirmed the internalization of FA-DABA-PSMA 350 kDa into the cytoplasm of the cell while the 20 kDa remained on the cell membrane<sup>138</sup>. This finding could be backed up by the characteristics of the polymer. Mentioned previously, the 350 kDa sheets have high malleability, allowing the chains to bend while maintaining their shape integrity. The 20 kDa cylinder in contrast, is very rigid compared to the sheet structure of the 350 kDa similar to a blanket at the surface of the cell. This becomes a significant factor as the computer simulations revealed the hydrophilic carboxylic groups of the polymer actively interacting with the surface of the receptor. This could result in an increase in the binding affinity depending on its malleability. From a previous study, internalization of 20 kDa was observed with the usage of WGA, wheat germ agglutinin, which binds to N-acetyl-D-Glucosamine on FR $\alpha$ , increasing the flexibility of the receptor<sup>138</sup>. Thus, the binding affinity is highly correlated with the structural flexibility of the polymer. In addition, a recent study of FA-DABA-PSMA with cell interaction in presence of lectin provided evidence of the need of flexibility either for the receptor or polymer self-assembly to maximize the FA-FR $\alpha$  interaction<sup>138</sup>. Next, a test to determine if the polymer is able to maintain its bond to the receptor when the pH is decreased to 5.5.

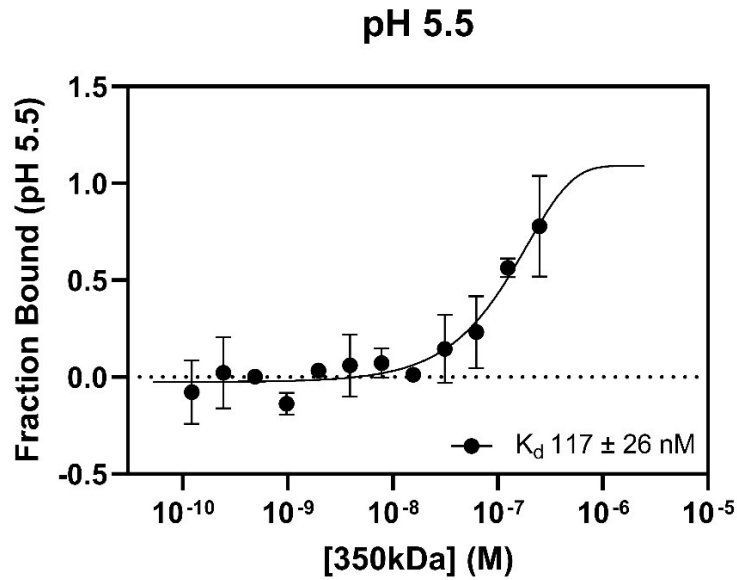


Figure 56. Binding affinity curve of FA-DABA-PSMA 350 kDa at pH 7.5

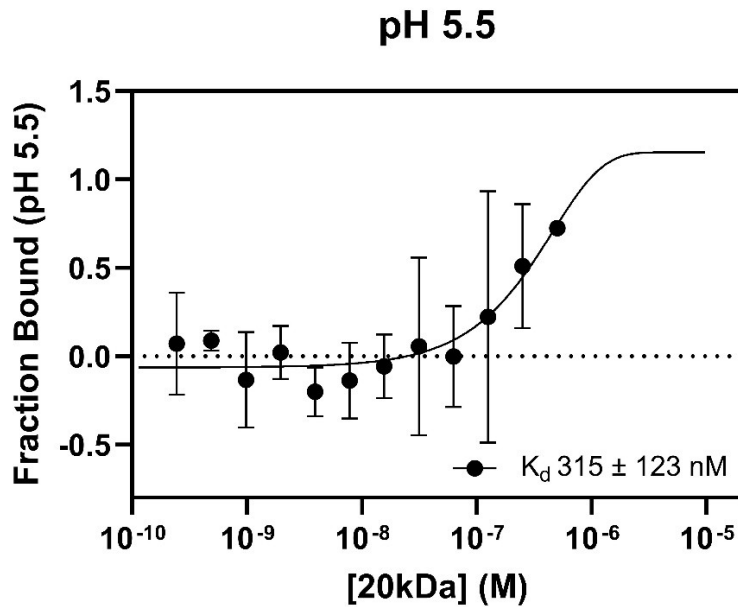


Figure 57. Binding affinity curve of FA-DABA-PSMA 20 kDa at pH 5.5

Despite the decrease in pH to generate an acidic environment for polymer release, the 350 kDa and 20 kDa were able to maintain a high binding affinity with

the FR $\alpha$ . A decrease in binding affinity was observed with the 350 kDa to  $117 \pm 26$  nM, *Figure 56* while 20 kDa was within the error,  $315 \pm 123$  nM, *Figure 57*, indicating a possibility of no change as the  $K_d$  remained within proximity of the pH 7.5 result. This is an interesting result as it indicates that the FA-DABA-PSMA was able to remain bonded to FR $\alpha$  despite the change in the pH. At pH 5.5, release of FA was observed and corresponds to its characteristic where the ligand receptor separation occurs at the lysosome, which has an approximate pH of 5<sup>153,154</sup>. Considering the fundamental characteristic of the polymer, a pH-sensitive polymer, a change in pH will correspond to a disruption in the self-assembly structure. The acidic protons can disturb the hydrogen bonds in the polymer, and destruction of the polymer self-assembly for a controlled release of the payload after endocytosis of the FR $\alpha$  and FA-DABA-PSMA. However, the results reveal that the FA-DABA-PSMA will remain with the FR $\alpha$  even after the drop in pH experienced in the cancer cell environment. With a decrease of pH, the self-assembly of the polymer is disrupted and the free chains of the polymers can surround the receptor through hydrogen bonding with hydrophilic amino acids of the receptor. This wrap around could prevent the interaction between acidic protons and amino acids that needs to be protonated to release the FA-DABA-PSMA from the receptor as the protons may be interacting with the polymer instead of entering the pocket of the receptor. Specifically, this prevention of the protons prohibits the amino acid D81 from protonating. As mentioned previously, D81 had the highest binding affinity with FA, and without protonation of this amino acid, a release of FA-DABA-PSMA is impossible<sup>94</sup>. It is clear from this experiment that the shape and the pH play a crucial part in affecting the binding affinity between the FR $\alpha$  with FA-DABA-PSMA 350 kDa and 20 kDa.

## 5.4. Conclusion

This study determined the inability of the FR $\alpha$  to release FA-DABA-PSMA 350 kDa and 20 kDa through MST. The binding affinity,  $K_d$  of FA-DABA-PSMA 350 kDa and 20 kDa was lower than the binding affinity of FA, suggesting the observation is not due to the binding energy but its inability to be released from the receptor. This was a finding that agrees with the results from computational simulation discussed earlier in this thesis, where the maleic acid of the PSMA was seen forming multiple hydrogen bonds with AAs on the surface of the FR $\alpha$ . Combining the results from the computational simulation and experimental, it could be concluded that due to the pH sensitivity of the PSMA, a change in pH may increase the FR $\alpha$  – polymer interaction chemotherapeutic, causing the polymer chains to disable the release of FA. With this novel finding, the FA-DABA-PSMA may be used as a complement to chemotherapeutic drug enhancing their potency for cancer treatment.



## 6. Indium Oxine Encapsulation

### 6.1. Introduction

One of the main causes of the low 5-year survival rate of pancreatic cancer is due to poor diagnosis<sup>155</sup>. The stealthy properties of pancreatic cancer often result in a diagnosis of stage 3 or 4, where the treatment options become very limited. Currently, the instruments used to diagnose patients with pancreatic cancer is by using computed tomography (CT), magnetic resonance imaging (MRI), ultrasound, X-ray, single photon emission computed tomography (SPECT), and positron emission tomography (PET)<sup>156</sup>. Besides the PET scan, the other instruments depend highly on a person's ability to analyze the scans/imaging to determine if an abnormality is observed. This could lead to a false diagnosis or a missed diagnosis of the tumour.

Radiopharmaceuticals have been used for various detection and treatment of cancer in the body<sup>157</sup>. One of the main advantages of radiopharmaceuticals its ability to be incorporated into an existing method of treatment as a diagnostic tool or as a therapeutic agent. The gamma ray emitted by the radioisotope is often used for diagnosis using SPECT or PET, while the alpha or beta particle emitted by the radioisotope could be used for therapy. Often almost identical chemical characteristics of the radioisotope metals, a diagnostic radioisotope can be swapped with a therapeutic radioisotope and used as a theragnostic agent where diagnosis and therapy can be achieved simultaneously.

Currently, multiple FDA-approved radiopharmaceuticals are being used for imaging cancer and various diseases. FDG, <sup>18</sup>F-fludeoxyglucose is one of the most successful and widely used radiotracers, which is used to detect cancer<sup>158</sup>. Yet, FDG is a derivative of glucose and its targeting relies on the characteristic of cancer, where nutrition is focused on supporting its uncontrolled growth and glucose is used by multiple types of healthy cells as well<sup>158</sup>. To increase the precision of radio imaging, direct targeting drugs, antibodies, and nanoparticles were developed using radioactive isotopes. <sup>111</sup>Indium-Oxyquinoline was used for labeling white blood cells in the body, <sup>68</sup>Gallium-prostate-specific membrane antigen-617 for prostate imaging, and <sup>111</sup>Indium-diethylenetriamine pentaacetate (DTPA)-octreotide for somatostatin receptors are three examples of radiopharmaceuticals that have been approved by the FDA for radio imaging cancer cells using direct targeting mechanism<sup>159,160</sup>. However, these radiopharmaceuticals have drawbacks associated with them. <sup>111</sup>In-Oxine labeled WBC rely on WBC to be activated by the immune system and target cancer thus, when it is not activated, it reduces the precision of the imaging<sup>161</sup>. For <sup>68</sup>Ga-prostate-specific membrane antigen-617 and <sup>111</sup>In-DTPA-octreotide, both radiolabeled compounds target specific receptors that are present in cancer. Thus, the imaging becomes challenging when the receptors are not overexpressed on the cells<sup>162</sup>. While there are limitations, the advantages of these drugs outweigh the negatives associated. Thus, similar to <sup>68</sup>Ga-prostate-specific membrane antigen-617

and  $^{111}\text{In}$ -DTPA-octreotide, FA-DABA-PSMA, which specifically targets  $\text{FR}\alpha$ , which is overexpressed in various cancer cells, could be labelled with a radioactive compound and used as an imaging agent.

Among the different radioisotopes used for radio imaging,  $^{111}\text{In}$ -Oxine was chosen to be the compound for radiolabeling the FA-DABA-PSMA.  $^{111}\text{In}$ -Oxine is  $^{111}\text{In}$ Indium chelated with a hydrophobic 8-hydroxyquinoline compound. As a result, the  $^{111}\text{In}$ -Oxine becomes a hydrophobic radioactive compound that could be encapsulated into the hydrophobic core of the FA-DABA-PSMA. As a result, this would allow the polymer system to be radiolabelled and potentially used for radio imaging to find cancer using SPECT. To determine the encapsulation potential for In-Oxine, non-radioactive In-Oxine was used for fluorescence spectroscopy and neutron activation analysis, while radioactive  $^{111}\text{In}$ -Oxine was used for thin layer chromatography. Various mixing techniques were used to test the encapsulation of radioactive and non-radioactive In-Oxine.

## 6.2. Methods

FA-DABA-PSMA 350 kDa and 20 kDa were prepared using the synthesis method from Li<sup>62</sup>. Both 350 kDa and 20 kDa were dissolved in 10 mL of 1x PBS buffer. The solution was sonicated for 5 minutes and left overnight on a plate shaker.

The synthesis of non-radioactive and radioactive In-Oxine was synthesized following previously published procedures<sup>163</sup>. 0.3g of  $\text{InCl}_3$  (99.99%, Sigma-Aldrich) was dissolved in 10 mL of 1M NaOAc pH 5.5. 0.5g of 8-hydroxyquinoline (Sigma-Aldrich) was dissolved in 10 mL of EtOH. The solutions were mixed for 15 minutes at room temperature then 10 mL of  $\text{CHCl}_3$  was added and stirred. This bottom layer of the separated mixture was extracted and dried at 70°C. A yellow precipitate was collected and characterized using the NMR spectrum (Ascend 400, Bruker, MA, US).

Radioactive  $^{111}\text{In}$ -Oxine was synthesized with the same procedures as the non-radioactive with a difference in the quantity of the compounds. 1  $\mu\text{L}$  of 1mCi  $^{111}\text{InCl}_3$  (BWXT Medical, Vancouver, Canada) was dissolved in 2 mL of 0.1M NaOAc pH 5.5. 20 mg of 8-hydroxyquinoline (Sigma-Aldrich) was dissolved in 1 mL of EtOH. 15  $\mu\text{L}$  of 8-hydroxyquinoline solution was added to  $^{111}\text{InCl}_3$  solution and mixed for 15 minutes at room temperature. 1 mL of  $\text{CHCl}_3$  was added and stirred. This bottom layer of the separated mixture was extracted and dried at 70°C. 40  $\mu\text{L}$  of EtOH was added to dissolve the dried powder. The characterization was completed using TLC with 100% EtOAc and strips of Whatman #1 filter paper (Sigma-Aldrich).

The radioactive and non-radioactive In-Oxine was added to the FA-DABA-PSMA solution in various ways and quantities. The solution of non-radioactive In-Oxine with FA-DABA-PSMA was mixed for 3 hours on a plate rocker. The

radioactive solution was mixed for 1 hour using a plate shaker. Details of the exact volume and radioactivity will be discussed below. The characterization of encapsulation using non-radioactive In-Oxine was performed using Duetta fluorescence and absorbance spectrometer (Horiba, Kyoto, Japan) for fluorescence spectroscopy, NAA was completed by irradiating the sample using RMC SLOWPOKE-2 reactor, and analysis was completed using HPGe detector. All the samples used for NAA were completed using a 2 mL solution.

## 6.3. Results and Discussion

### 6.3.1. Non-Radioactive Indium-Oxine

The non-radioactive In-Oxine was characterized using fluorescence spectroscopy and neutron activation analysis. The experimental procedure mirrored a previous encapsulation experiment developed for the delivery of curcumin as a cancer treatment using the FA-DABA-PSMA polymer as a carrier<sup>95</sup>. The initial experiment was performed to mimic the same procedure followed by subsequent experiments for improvement and tailoring for this specific application.

#### 6.3.1.1. Fluorescence Spectroscopy

Before characterization of In-Oxine encapsulation inside the hydrophobic core of the functionalized polymer, the fluorescence of the In-Oxine was obtained by obtaining an, excitation emission matrix, EEM plot. Obtaining an EEM plot allows the determination of the excitation and emission wavelength of the In-Oxine before encapsulation.

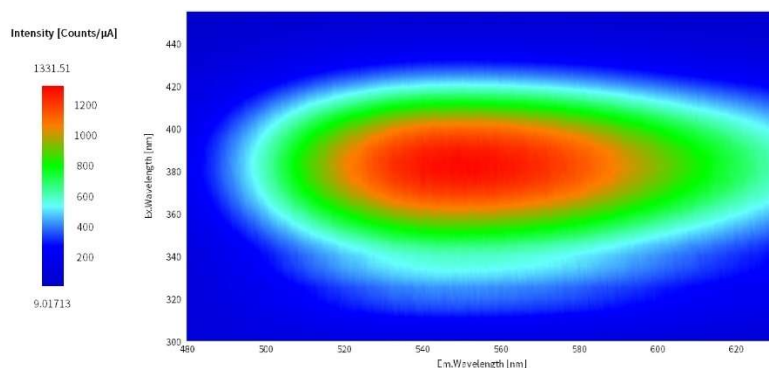


Figure 58. 3D EEM plot of Indium-Oxine

As depicted in *Figure 58*, the EEM plot of In-Oxine was obtained using excitation and emission bandpass of 5 nm. The y-axis represents the excitation wavelength in nanometer and x-axis in emission wavelength in nanometer. From this plot, the fluorescence of In-Oxine can be seen from an excitation wavelength of 320 nm to 430 nm when the emission wavelength is 485 nm to 640 nm. Next,

the fluorescence of FA-DABA-PSMA must be measured to determine if the fluorescence is present and if it doesn't overlap with the In-Oxine spectra as seen in *Figure 59* to *Figure 62*.

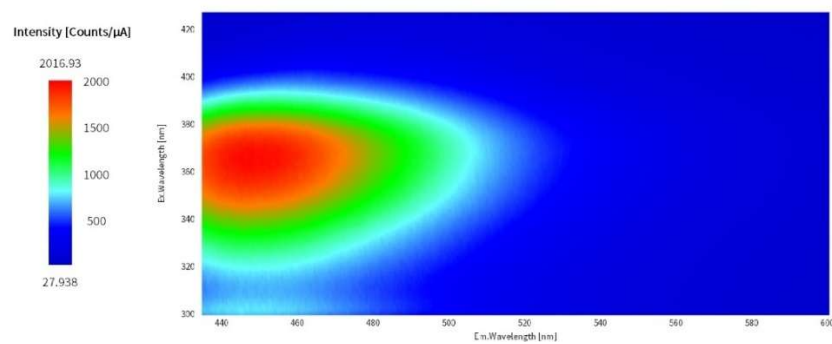


Figure 59. 3D EEM plot of FA-DABA-PSMA 350 kDa

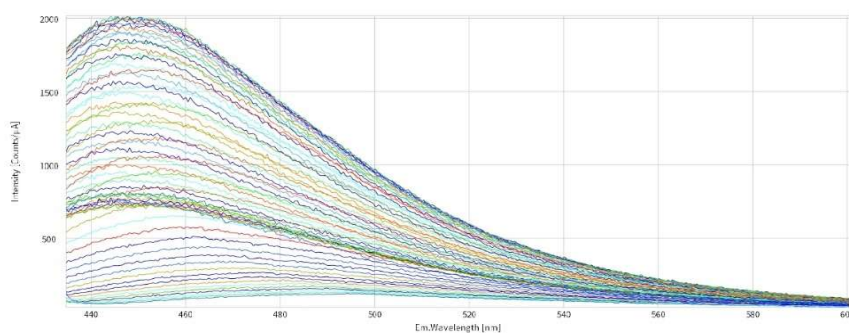


Figure 60. 2D Emission plot converted from 3D EEM plot of FA-DABA-PSMA 350 kDa

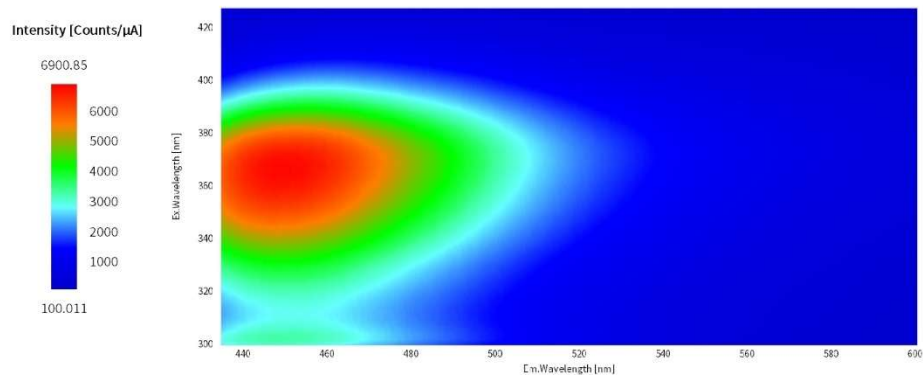


Figure 61. 3D EEM plot of FA-DABA-PSMA 20 kDa

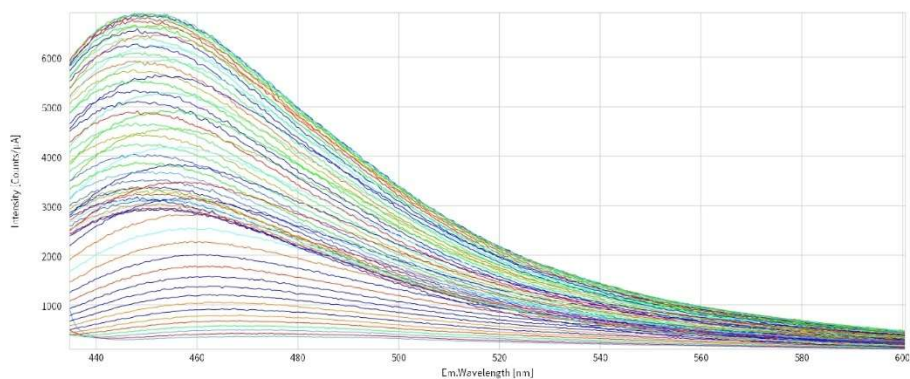


Figure 62. 2D Emission plot converted from 3D EEM plot of FA-DABA-PSMA 20 kDa

The FA-DABA-PSMA 350 kDa and 20 kDa both emit fluorescence from 310 nm to 400 nm for excitation wavelength and 420 nm to 530 nm for emission wavelength as seen from *Figure 59 to 62*. An overlap exists between the FA-DABA-PSMA and In-Oxine however, the highest peak of each spectrum is separated, which allows the characterization of encapsulated In-Oxine. As mentioned, initially, solid In-Oxine powder 0.3 mg was added to 7 mL of 200  $\mu$ M FA-DABA-PSMA 350 kDa and 20 kDa. The solutions were sonicated for 5 minutes and placed on a plate rocker for three hours. After mixing, the solutions were centrifuged for 6 minutes at 3400g, and the supernatant was collected and used for analysis.

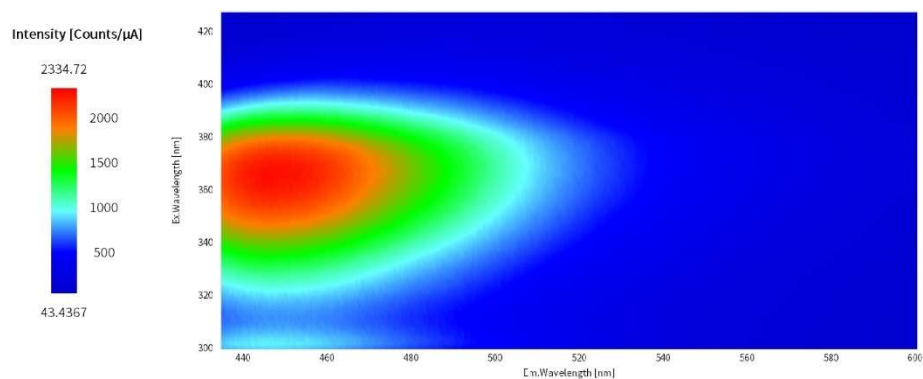


Figure 63. 3D EEM plot of 0.3 mg of In-Oxine added to FA-DABA-PSMA 350 kDa

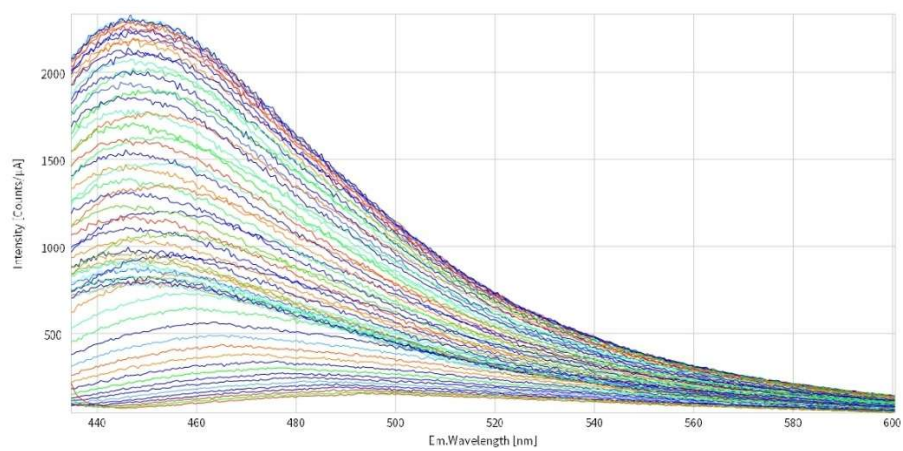


Figure 64. 2D Emission plot converted from 3D EEM of 350 kDa and In-Oxine

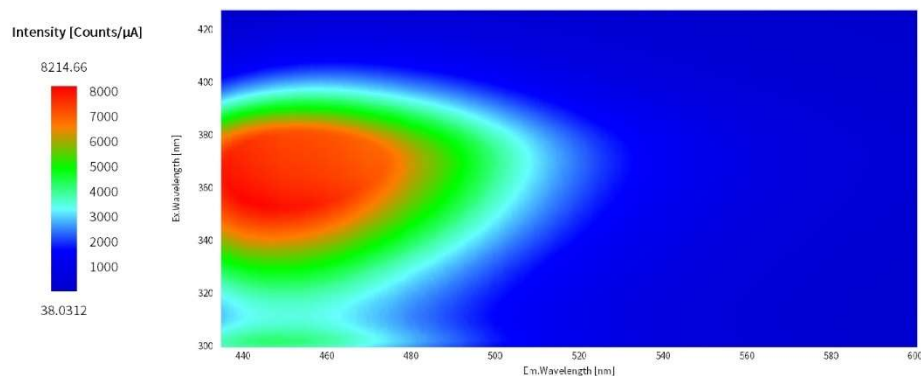


Figure 65. 3D EEM plot of 0.3 mg of In-Oxine added to FA-DABA-PSMA 20 kDa

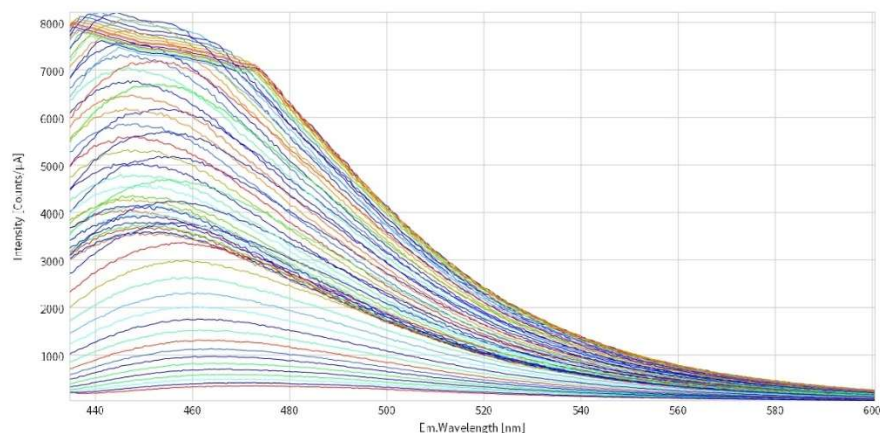


Figure 66. 2D Emission plot converted from 3D EEM of 20 kDa and In-Oxine

In *Figures 63 to 66* it can be observed that the fluorescence spectra of both 350 kDa and 20 kDa only include fluorescence characteristics of the functionalized polymer. The fluorescence of In-Oxine, 320 nm to 430 nm for emission wavelength and 485 nm to 640 nm for excitation wavelength completely absent. It should be noted that when the solution was sonicated, the powder was able to break into dust; however, after centrifugation, sediments of In-Oxine were observed at the bottom of the conical centrifuge tubes. Due to the high hydrophobicity of the In-Oxine could be unable to dissolve in the solution and allow encapsulation into the hydrophobic core of the polymer. Thus, the identical quantity of In-Oxine was dissolved in 50  $\mu$ L



of DMSO and added to the polymeric solution to determine if this method would allow successful encapsulation of In-Oxine.

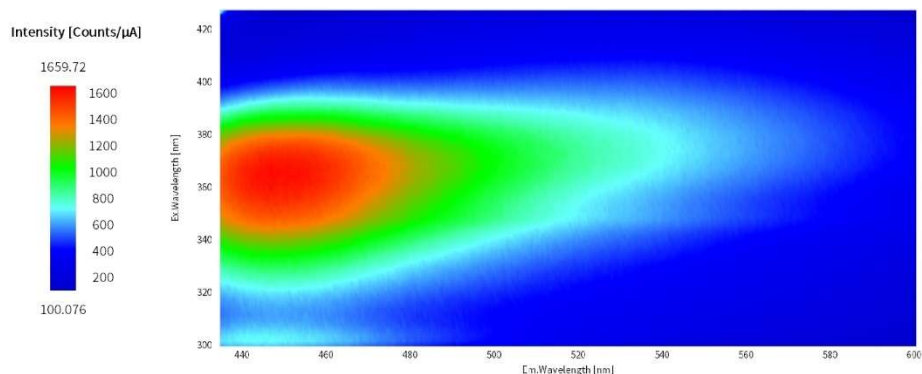


Figure 67. 3D EEM plot of In-Oxine dissolved in DMSO added to FA-DABA-PSMA 350 kDa

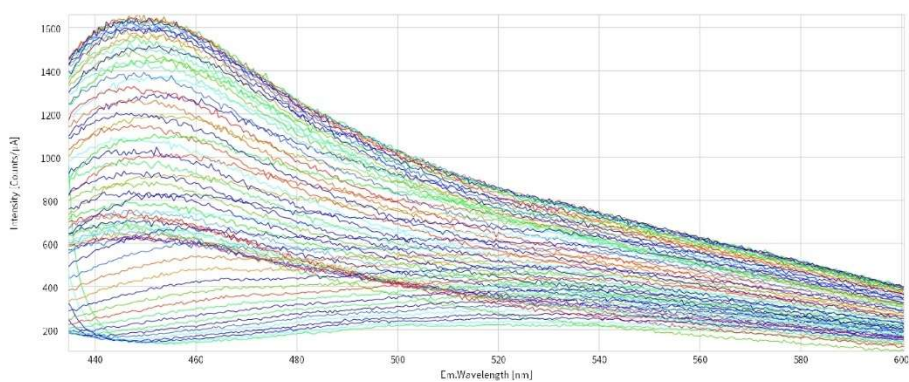


Figure 68. 2D emission plot from 3D EEM plot of In-Oxine dissolved in DMSO added to FA-DABA-PSMA 350 kDa



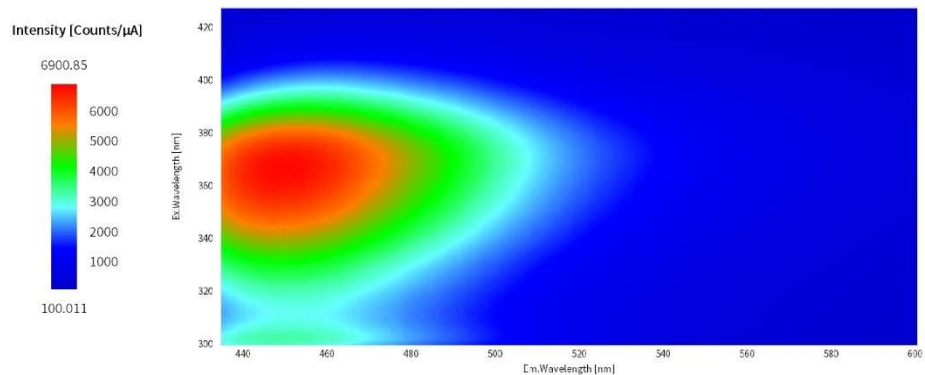


Figure 69. 3D EEM plot of In-Oxine dissolved in DMSO added to FA-DABA-PSMA 20 kDa

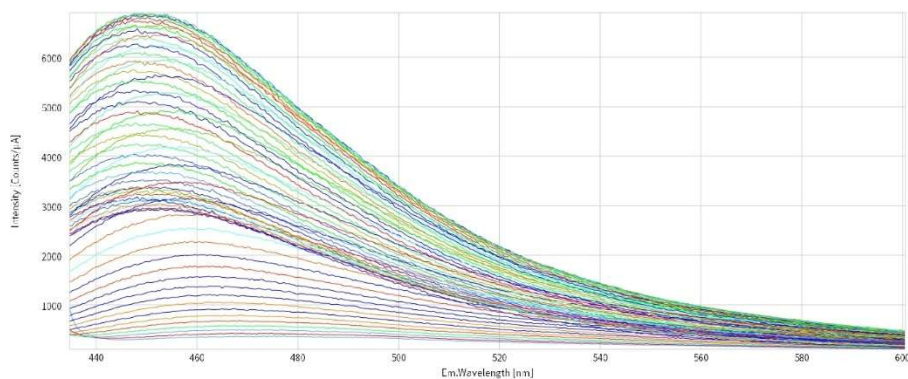


Figure 70. 2D emission plot from 3D EEM plot of In-Oxine dissolved in DMSO added to FA-DABA-PSMA 20 kDa

A change in fluorescence spectra of the 350 kDa was observed when In-Oxine was dissolved in DMSO. From *Figure 67 and 68*, an extension of the intensity was observed to 580 nm of emission wavelength, where the previous, non-DMSO dissolved spectra only expanded up to 520 nm. A change in 2D graphs of the spectra can also be observed. With DMSO, a small hump from 500 nm to 600 nm can be observed in *Figure 68*. This finding corresponds to the fluorescence spectra of the pure In-Oxine. This suggests that the polymer is capable of encapsulating In-Oxine, yet a solid In-Oxine is unable to be encapsulated inside the polymer as it is unable to interact with the polymer due to its high hydrophobicity. Interestingly, as seen in *Figure 69* and *Figure 70*, the 20 kDa, despite the addition of DMSO, the spectra

didn't detect any In-Oxine. This was an odd finding as success in encapsulation was observed in the 350 kDa.

### 6.3.1.2. Neutron Activation Analysis

Neutron activation analysis serves as an excellent method of analysis due to its capability to measure the number of specific elements within the sample and its detection limit suited for *in situ* analysis with a low concentration sample. The detection limit of NAA is highly dependent on the detector used for the analysis. High purity Germanium (HPGe) was selected for this study as it serves as a sensitive detector that could analyze down to PPB quantities depending on the element. This is highly advantageous in determining the presence of an element as a qualitative and quantitative method. In the real world, radiation diagnosis using  $^{111}\text{In}$ -Oxine as WBC labelling, 300 to 500  $\mu\text{Ci}$  is used for a human adult<sup>164</sup>. This dosage of radiation is equivalent to 0.714 to 1.19 ng of  $^{111}\text{In}$  atoms. Thus, when determining the possibility of  $^{111}\text{In}$ -Oxine encapsulation, a similar amount should be used to simulate similar conditions. At the nanogram scale, the detection becomes increasingly challenging due to the sensitivity of the instruments. Here, we present the results obtained through NAA of the identical samples used for fluorescence spectroscopy.

**Table 14.** NAA results of sample used for fluorescence spectroscopy

|              | FA-DABA-<br>350 kDa<br>(solid In-<br>Oxine) | FA-DABA-<br>350 kDa<br>(DMSO In-<br>Oxine) | FA-DABA-<br>20 kDa<br>(solid In-<br>Oxine) | FA-DABA-<br>20 kDa<br>(DMSO In-<br>Oxine) |
|--------------|---|--|--|---|
| Indium (ppm) | 0.53<br>$\pm 0.02$                          | 3.55<br>$\pm 0.05$                         | 0.38<br>$\pm 0.02$                         | 4.57<br>$\pm 0.06$                        |

The NAA results, *Table 14* are in agreement with the fluorescence spectroscopy results, where we see a significant increase in the amount of Indium present in the samples when it was dissolved in DMSO. Interestingly, from the fluorescence results, despite the addition of DMSO, in the 20 kDa sample, the fluorescence of In-Oxine was not visible. Yet, in the NAA results, the 20 kDa with In-Oxine in DMSO had the highest amount present. Furthermore, after the mix of the four samples, 4 mL of the supernatant was added to 4 mL of 200  $\mu\text{M}$  polymer solution to determine if the In-Oxine was indeed encapsulated within the polymer. By the addition of empty polymers, the In-Oxine is able to form an equilibrium with the polymer. The samples were mixed and centrifuged identically to the previous samples.

**Table 15.** NAA result of diluted samples from Table 14

|                                    | FA-DABA-<br>350 kDA<br>(solid In-<br>Oxine) | FA-DABA-<br>350 kDA<br>(DMSO In-<br>Oxine) | FA-DABA-<br>20 kDA<br>(solid In-<br>Oxine) | FA-DABA-<br>20 kDA<br>(DMSO In-<br>Oxine) |
|------------------------------------|---|--|--|---|
| Indium (ppm)                       | 0.23<br>± 0.01                              | 1.48<br>± 0.04                             | 0.11<br>± 0.02                             | 2.16<br>± 0.04                            |
| Comparison<br>with Table 14<br>(%) | 48%   | 42%  | 30%  | 47%                                       |

As predicted, the dilution was able to reduce the Indium to a desired quantity as seen in *Table 15*. Previously, when samples were centrifuged, the non-encapsulated In-Oxine were seen as sediment at the bottom of the tube. Therefore, if the supernatant solution is the functionalized polymer with In-Oxine encapsulated, the amount of Indium present in the diluted sample should be approximately half as the centrifugation will push non-encapsulated In-Oxine to be a sediment at the bottom of the tube. To successfully conclude the necessity of dissolving the In-Oxine in a solvent before mixing with the polymeric sample, a controlled study was performed identically to the previous procedure, with the addition of ethanol, EtOH as a solvent of test and the polymer solution was replaced with PBS buffer.

**Table 16.** Control Test of In-Oxine in PBS

|              | Solid          | DMSO           | EtOH           | Blank              |
|--------------|----------------|----------------|----------------|--------------------|
| Indium (ppm) | 0.40<br>± 0.01 | 0.37<br>± 0.01 | 0.45<br>± 0.01 | 0.0010<br>± 0.0010 |

From the control experiment, *Table 16*, the amount of Indium without any addition of solvent was 0.40 ppm. Comparing this result to previous NAA results with the polymer solution and solid In-Oxine, it can't be successfully concluded that the ppm of Indium detected is encapsulated in the polymer. However, when the DMSO samples are compared, the background of the In-Oxine count only accounts for about 10% of the value obtained. If the amount of Indium with the DMSO sample was close to the value obtained using the polymer solution, the encapsulation of In-Oxine couldn't be successfully identified. However, since the values obtained from the control are within 12% of the amount of polymer solution is significantly different. It can be determined that the In-Oxine is encapsulated. Since dissolving the In-Oxine in a solvent is a requirement, an ideal solvent that doesn't cause toxicity to the human body must be determined. Since this study is a build-up for a future *in vitro* or *in vivo* test, a biocompatible solvent must be selected.

As a result, ethanol, EtOH was chosen as a solvent as the human body is capable of stabilizing EtOH. The EtOH used to dissolve In-Oxine is in  $\mu\text{L}$  scale

which wouldn't cause any chemical change to the polymer solution or poses toxicity to the body<sup>165</sup>. Therefore, a test using 200  $\mu$ L EtOH as a solvent for In-Oxine was tested with the polymers. The procedure was identical to the previous polymer samples.

**Table 17.** FA-DABA-PSMA with EtOH as a solvent for In-Oxine

|              | FA-DABA-PSMA 350<br>kDa | FA-DABA-PSMA 20<br>kDa |
|--------------|-------------------------|------------------------|
| Indium (ppm) | 1.75<br>$\pm$ 0.03      | 1.73<br>$\pm$ 0.03     |

As predicted, *Table 17* shows that dissolving In-Oxine in EtOH increased the ppm of Indium when compared to Indium without any solvent. The values are about half of the DMSO dissolved values and this agrees with the correlation to the solubility of the solvent. DMSO is considered one of the best solvents used to dissolve hydrophobic compounds. The polarity of the solvent correlates its the solubility of hydrophobic compounds. When DMSO and ethanol are compared, while both solvents are water miscible, DMSO is less polar than ethanol, thus its solubility to dissolve In-Oxine would be higher. It should be noted that as previously mentioned, the amount of In-Oxine needed for encapsulation for diagnosis is in the nanoscale. Here, converting the ppm values to grams gives 3.52  $\mu$ g, which is a thousand times higher than the needed amount. In addition, 2 mL of supernatant solution was used to test for NAA. Therefore, in the case of a 10 mL sample, the amount of In-Oxine present would be 5 times higher than obtained from NAA results. As a result, EtOH can be used as an ideal solvent to encapsulate In-Oxine inside the polymer. Finally, a polymer concentration was performed with a constant amount of In-Oxine to determine if the concentration of the polymer would affect the In-Oxine encapsulation. This would also serve as an excellent tool to determine the encapsulation of In-Oxine, as a decrease in Indium detection due to polymer concentration would indicate that In-Oxine is encapsulated in the polymer, as excess would be sediment after centrifuging.

For *in vivo* or clinical trials, an appropriate concentration of the polymer must be selected. While maximizing the concentration may maximize the targeting ability and effect, cytotoxicity of the polymer must be considered. While the polymer is biocompatible and safe, there is a concentration it must be kept below before it becomes toxic to the body. While our polymer has not been tested to determine such, we selected a concentration range between 3  $\mu$ M to 2000  $\mu$ M based on previous experiment where the half-maximal inhibitory concentration,  $IC_{50}$ , for 350 kDa was 3.979  $\mu$ M and 28231  $\mu$ M for 20 kDa at 24 hours *in vitro* using DU-145, prostate cancer cells<sup>63</sup>. It should be noted that this cytotoxicity experiment was performed *in vitro* where the FA-DABA-PSMA solutions are added directly to the cells. However, *in vivo*, the injected solutions enter the bloodstream and distribute around the body. Thus, a higher concentration can be used and is tolerable. Various concentration of

FA-DABA-PSMA 350 kDa and 20 kDa was used to determine if change concentration will impact the encapsulation of In-Oxine.

200  $\mu$ M of FA-DABA-PSMA 350 kDa and 20 kDa were prepared and diluted to a concentration of 3  $\mu$ M. Note that the In-Oxine solution was added after the dilution, whereas in the previous dilution from Table 4, the dilution was performed using a supernatant solution after the addition of In-Oxine. 2.74  $\mu$ M of In-Oxine dissolved in EtOH was prepared, and 15  $\mu$ L of the solution was added to the 3 mL polymer solution. This low concentration was used to mimic the nanogram scale In-Oxine that would be used for application in medical settings. The samples were mixed for 3 hours on a plate rocker. The solution was centrifuged for 5 minutes at 3400g. 2 mL of the supernatant was obtained and used for analysis. A control sample was prepared identically to the polymer solution with PBS solution.

**Table 18.** 3  $\mu$ M vs 200  $\mu$ M concentration test of FA-DABA-PSMA

|                 | Control                | 200 $\mu$ M<br>FA-<br>DABA-<br>PSMA<br>350 kDa | 3 $\mu$ M<br>FA-<br>DABA-<br>PSMA<br>350 kDa | 200 $\mu$ M<br>FA-<br>DABA-<br>PSMA<br>20 kDa | 3 $\mu$ M<br>FA-<br>DABA-<br>PSMA<br>20 kDa |
|-----------------|------------------------|--|--|---|---|
| Indium<br>(ppm) | 0.0021<br>$\pm$ 0.0002 | 0.0039<br>$\pm$ 0.0003                         | 0.0018<br>$\pm$ 0.0002                       | 0.0023<br>$\pm$ 0.0002                        | 0.0015<br>$\pm$ 0.0002                      |

In agreement with previous results, in *Table 18*, a decrease in polymer concentration decreased the amount of In-Oxine encapsulated. To confirm this finding, an additional test was conducted to determine if increasing the polymer concentration would allow an increase in encapsulation. An excess of In-Oxine was added to determine if maximum encapsulation could be achieved. 2000  $\mu$ M polymer solution was prepared and diluted to 500  $\mu$ M. 15  $\mu$ L of 548  $\mu$ M In-Oxine was added to 3 mL of polymer solutions. The solution was mixed for 3 hours on a plate rocker, centrifuged for 5 minutes at 3400g and 2 mL of supernatant was collected and used for analysis. The control sample in this run was prepared differently, indeed he 15  $\mu$ L of In-Oxine was added to 2 mL of PBS solution. The solution was not mixed or centrifuged and was analyzed directly. The control sample was not centrifuged to produce a theoretical encapsulation yield, as no Indium-Oxine would be lost from centrifugation. Thus, encapsulation efficiency can be calculated by comparing this value with the Indium ppm obtained from polymer samples. The adjusted Indium for volume was calculated by multiplying the amount of Indium obtained by 1.5, as the total volume of the solution before centrifugation was 3 mL. The encapsulation efficiency was calculated using the adjusted Indium values.

**Table 19.** 500  $\mu\text{M}$  vs 2000  $\mu\text{M}$  concentration test of FA-DABA-PSMA

|   | Control                | 2000 $\mu\text{M}$<br>FA-<br>DABA-<br>PSMA<br>350 kDa | 500 $\mu\text{M}$<br>FA-<br>DABA-<br>PSMA<br>350 kDa | 2000 $\mu\text{M}$<br>FA-<br>DABA-<br>PSMA<br>20 kDa | 500 $\mu\text{M}$<br>FA-<br>DABA-<br>PSMA<br>20 kDa |
|---|------------------------|---|--|--|---|
| Indium (ppm)                              | 0.3873<br>$\pm$ 0.0019 | 0.1852<br>$\pm$ 0.0013                                | 0.1511<br>$\pm$ 0.0012                               | 0.0784<br>$\pm$ 0.0012                               | 0.0852<br>$\pm$ 0.0012                              |
| Adjusted<br>Indium for<br>volume<br>(ppm) | 0.3873<br>$\pm$ 0.0019 | 0.2278<br>$\pm$ 0.0013                                | 0.2267<br>$\pm$ 0.0012                               | 0.1176<br>$\pm$ 0.0012                               | 0.1278<br>$\pm$ 0.0012                              |
| Encapsulation<br>Efficiency<br>(%)        | 100%                   | 71.73%  | 58.52%   | 30.36%   | 33.00%  |

Here, *Table 19*, a direct encapsulation percentage can be calculated as the control sample was not centrifuged. This allows the amount value obtained from the control to be the theoretical encapsulation yield for comparison if encapsulation of the In-Oxine in the polymer was 100%. A direct comparison can't be made with *Table 7* as the amount of In-Oxine used between the two tables is different. However, a trend of an increase in encapsulation with increased polymer concentration can be observed in both tables. It's worth mentioning that when the polymer solutions were centrifuged, some sediments of 350 kDa were observed at the bottom of the tube along with In-Oxine sediments, suggesting it may be supersaturated. This observation was also seen when 10 mg of the 350 kDa was added to 10 mL of PBS, some sediments were observed despite mixing for over 3 days. The two observations suggest that approximately 2000  $\mu\text{M}$  is the supersaturation concentration of FA-DABA-PSMA 350 kDa. It is important to note that for 20 kDa samples, a decrease of 500  $\mu\text{M}$  from 2000 $\mu\text{M}$  increased the encapsulation efficiency. The encapsulation efficiency of both samples was poor when compared to 350 kDa. The In-Oxine used for this run is much higher compared to the concentration that will be used for medical applications. Thus, proven that the polymer is able to encapsulate such a high amount compared to the radioactive amount, and it could be utilized for radiolabeling.

### 6.3.2. Radioactive In-Oxine

To fully determine the possibility of encapsulation of radioactive  $^{111}\text{In}$ -Oxine at the desired activity, a test was performed using radioactive  $^{111}\text{In}$ -Oxine. Due to the gamma radiation, there are limited tests that could be performed. TLC serves as one of the fastest efficient, and accurate tests that could be used for encapsulation characterization<sup>166</sup>. The testing with the radioactivity that is currently used for diagnosis ensures the ability of FA-DABA-PSMA to be used for future *in vitro* or *in vivo* studies.

### 6.3.2.1. Thin Layer Chromatography

The stripes used for TLC were prepared by measuring and cutting Whatman #1 filter papers. The dimensions of the strips were 6.5 cm in length and 0.5 cm in width, with retention factor,  $R_f = 0.0$  placed 1 cm from the bottom of the strip, while  $R_f = 1.0$  was placed 0.5 cm from the top. 0.2  $\mu\text{L}$  of the sample was placed at  $R_f = 0.0$ , and 160  $\mu\text{L}$  of 100% EtOAc was used as eluent for the mobile phase. The  $^{111}\text{In}$ -Oxine was prepared as mentioned in  $\delta 6.2$ . 10  $\mu\text{L}$  of  $^{111}\text{In}$ -Oxine dissolved in EtOH was mixed with 1 mL of 500  $\mu\text{M}$  FA-DABA-PSMA 350 kDa and 20 kDa. The activity of  $^{111}\text{In}$ -Oxine was 272  $\mu\text{Ci}$  and 187.1  $\mu\text{Ci}$  for 350 kDa and 20 kDa respectively. The solution was mixed for 1 hour then 2  $\mu\text{L}$  of solution was placed on TLC strip for analysis.

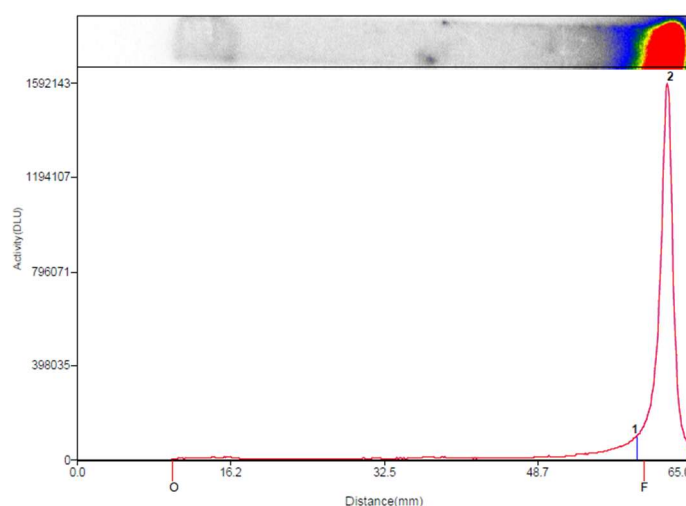


Figure 71. Lateral view of TLC of free  $^{111}\text{In}$ -Oxine

#T1 - Lane Group  
Lane #1  
Background Subtraction: Regions = 1,400.035 DLU /mm2  
Lane Origin (mm): 10.089  
Lane Front (mm): 60.013

| ID         | Dist From Origin(mm) | RF  | Area(mm2) | Net % Sum | Net % Max Reg. | Net % Total Lane |
|------------|----------------------|-----|-----------|-----------|----------------|------------------|
| 1 - Prof   | 42.6                 | 0.7 | 297.2     | 20.3      | 25.5           | 20.3             |
| 2 - Prof   | 62.3                 | 1.0 | 32.8      | 79.7      | 100.0          | 79.5             |
| 1-b - Prof |                      |     | 52.3      |           |                |                  |
| Lane       |                      |     | 391.0     |           |                | 100.0            |
| UnRes      |                      |     | 61.0      |           |                | 0.2              |

Figure 72. Summary of TLC of free  $^{111}\text{In}$ -Oxine

The synthesized  $^{111}\text{In}$ -Oxine was tested for TLC prior to encapsulation with polymer solution to determine if there would be the difference in  $R_f$  value. An increase in  $R_f$  value represents that the mobile phase of TLC with less polar

compounds will travel further on the strip, resulting in a higher  $R_f$  value. Indeed,  $R_f = 1.0$  was seen for free  $^{111}\text{In}$ -Oxine as it is highly hydrophobic. Next, the polymer solution was mixed with 272  $\mu\text{Ci}$  and 187.1  $\mu\text{Ci}$   $^{111}\text{In}$ -Oxine for 350 kDa and 20 kDa, respectively, to determine if different  $R_f$  results could be obtained.

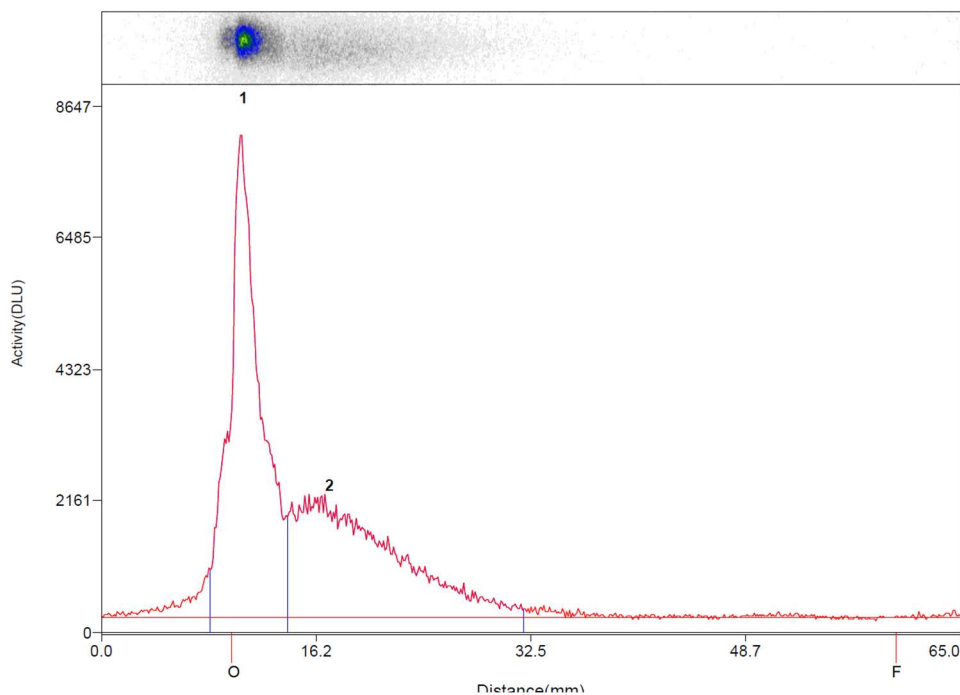


Figure 73. Lateral view of TLC of FA-DABA-PSMA 350 kDa with  $^{111}\text{In}$ -Oxine

| Lane #4  |                      |     |           |           |                |                  |
|--|----------------------|-----|-----------|-----------|----------------|------------------|
| Background Subtraction: Regions = 640.159 DLU /mm2 |                      |     |           |           |                |                  |
| Lane Origin (mm): 9.915                            |                      |     |           |           |                |                  |
| Lane Front (mm): 60.071                            |                      |     |           |           |                |                  |
| ID   | Dist From Origin(mm) | RF  | Area(mm2) | Net % Sum | Net % Max Reg. | Net % Total Lane |
| 1 - Prof   | 11.1                 | 0.0 | 29.3      | 55.2      | 100.0          | 52.5             |
| 2 - Prof   | 20.7                 | 0.2 | 89.3      | 44.8      | 81.2           | 42.6             |
| 1-b - Prof   |                      |     | 41.7      |           |                |                  |
| Lane   |                      |     | 325.0     |           |                | 100.0            |
| UnRes  |                      |     | 206.4     |           |                | 4.9              |

Figure 74. Summary of TLC of FA-DABA-PSMA 350 kDa with  $^{111}\text{In}$ -Oxine



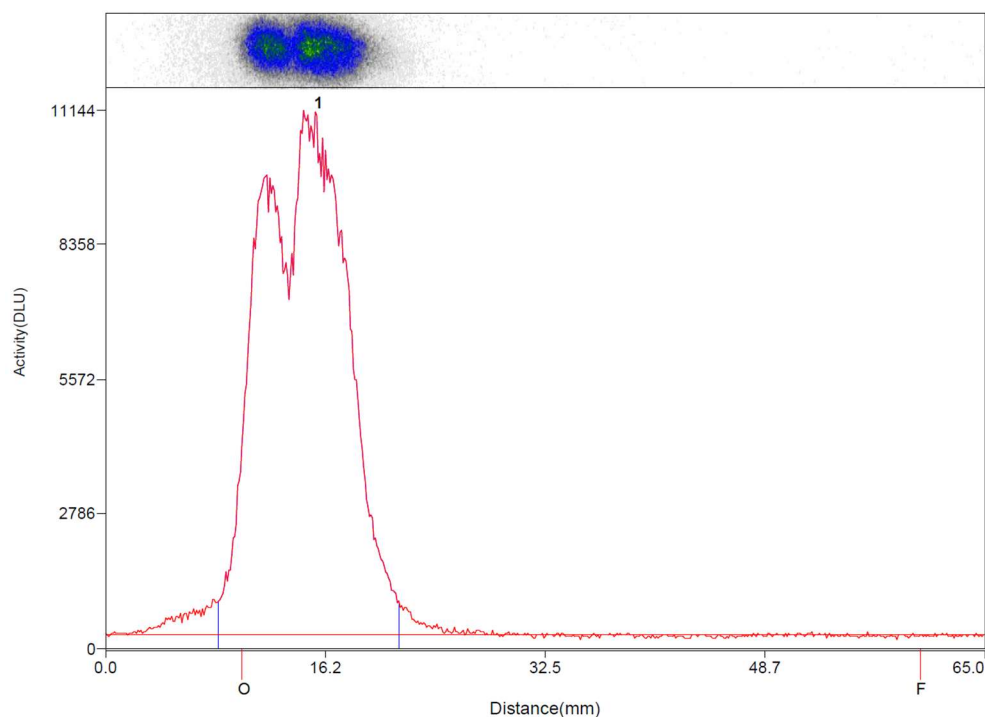


Figure 75. Lateral view of TLC of FA-DABA-PSMA 20 kDa with  $^{111}\text{In}$ -Oxine

Lane #3  
Background Subtraction: Regions = 692.736 DLU/mm<sup>2</sup>  
Lane Origin (mm): 10.089  
Lane Front (mm): 60.187

| ID         | Dist From Origin(mm) | RF  | Area(mm <sup>2</sup> ) | Net % Sum | Net % Max Reg. | Net % Total Lane |
|------------|----------------------|-----|------------------------|-----------|----------------|------------------|
| 1 - Prof   | 14.7                 | 0.1 | 66.7                   | 100.0     | 100.0          | 95.9             |
| 1-b - Prof |                      |     | 19.4                   |           |                |                  |
| Lane       |                      |     | 325.0                  |           |                | 100.0            |
| UnRes      |                      |     | 258.3                  |           |                | 4.1              |

Figure 76. Summary of TLC of FA-DABA-PSMA 20 kDa with  $^{111}\text{In}$ -Oxine

The  $R_f$  of the polymer solution with  $^{111}\text{In}$ -Oxine was 0.0. This corresponds to the characteristic of the polymer and the TLC, as PSMA sticks very well to the cellulose membrane due to the hydrophilic maleic acid which makes the polymer highly polar. A slight mobile phase was observed with the 350 kDa sample, while the 20 kDa didn't have any movement. The movement could correspond to the characteristics of the polymer. The sheet formation of the 350 kDa allows for some flexible movement, while 20 kDa is very rigid, not allowing any malleability, which agrees with the findings mentioned earlier in this paper. The two dots seen in *Figure 68* are due to an extra droplet made while the sample was pipetted onto the TLC strip.

However, when compared with *Figure 64*, a free  $^{111}\text{In}$ -Oxine, it can be concluded that they don't mirror one another. A difference in  $R_f$  between the free  $^{111}\text{In}$ -Oxine and  $^{111}\text{In}$ -Oxine with polymer is an excellent way to conclude the encapsulation of the  $^{111}\text{In}$ -Oxine inside the polymer. Such results were seen in an experiment where a polymeric micelle was used to encapsulate  $^{111}\text{In}$ -Oxine inside its hydrophobic core, and the  $R_f$  was 1 for free  $^{111}\text{In}$ -Oxine while the  $R_f$  of  $^{111}\text{In}$ -Oxine encapsulated in the micelle was 0<sup>163</sup>. This agreement allows characterization of encapsulation inside the polymer without complicated instruments. This is highly advantageous as TLC can be performed in a fast, efficient manner to determine if encapsulation has occurred. It should be noted that centrifugation or filtration was not performed as the free  $^{111}\text{In}$ -Oxine was not observed in the TLC of the polymer. With the addition of such a small amount of  $^{111}\text{In}$ -Oxine needed for radiolabeling, centrifugation or filtration may be unnecessary. While a higher amount of  $^{111}\text{In}$ -Oxine may be needed, from the NAA results, it has been found that the polymer is able to encapsulate much higher  $^{111}\text{In}$ -Oxine in its hydrophobic core, which allows the addition of  $^{111}\text{In}$ -Oxine with higher radioactivity. Thus, these findings suggest that the polymer is able to be radiolabeled and no filtration is necessary due to high encapsulation of the polymer.

This was a significant finding as we can successfully conclude that the radioactive  $^{111}\text{In}$ -Oxine is able to be encapsulated inside the polymer. This radiolabeling opens the possibility of determining the pharmacokinetics *in vivo* where the polymer can be tracked inside the mouse and its accumulation per organ using a SPECT. This finding would allow determination of its targeting ability which is critical in advancing the polymer for *in vivo* studies and clinical trials. If the FA-DABA-PSMA can exclusively target the cancer cells with minimum accumulation in different organs would be ground groundbreaking finding and also prove its purpose, a direct targeting therapy. The SPECT could also determine how long the radiolabeled polymer is detected in the cancer cells, as days of imaging can be obtained due to the 2.80 days of half-life of  $^{111}\text{In}$ -Oxine. If high radioactivity is detected in the tumour for days, this would also agree with previous findings from this paper, where FA-DABA-PSMA was able to remain bonded to the  $\text{FR}\alpha$  despite a decrease in pH for release.

## 6.4. Conclusion

The direct targeting ability and ability to encapsulate hydrophobic drugs of the FA-DABA-PSMA are highly promising for its usage with  $\text{FR}\alpha$  positive tumours. With the addition of a radioactive compound  $^{111}\text{In}$ -Oxine, the polymer could now be used as an early diagnostic tool. To successfully determine such, a characterization was completed. However, there isn't a molecular microscope that could visualize the hydrophobic core of the polymer which becomes increasingly challenging as changes in atomic properties must be measured. These types of characterizing instruments are usually very time-consuming, and there aren't guarantees that these instruments will be able to successfully determine the encapsulation of  $^{111}\text{In}$ -Oxine. Thus, in this study, characterization through comparison of concentrations and

controls was used with fluorescence spectroscopy, neutron activation analysis, and thin layer chromatography. The fluorescence spectroscopy and neutron activation analysis were first used to determine if dissolving In-Oxine in a solvent was necessary for encapsulation. It was concluded that EtOH is an ideal solvent. Next, supplementary experiments were completed using NAA to determine if the concentration of the polymer is a factor in enhancing the encapsulation of the In-Oxine. It was determined that increasing polymer concentration does indeed increase the encapsulation of In-Oxine, and the ideal concentration for *in vitro* or *in vivo* study is between 200 and 500  $\mu\text{M}$ . Lastly, TLC was conducted using radioactive  $^{111}\text{In}$ -Oxine and found  $R_f$  was 1.0 for free  $^{111}\text{In}$ -Oxine while the encapsulated solution remained at  $R_f$  of 0.0. With successful characterization and conclusion of In-Oxine encapsulation with the FA-DABA-PSMA 350 kDa and 20 kDa, its potential to be used as an early diagnostic drug is promising.

## 7. Conclusion and Future Outlook

Cancer remains one of the most challenging group of diseases that the medical industry needs to maintain its highest priority in research. Cancer can occur to anyone at any point in their life, and if found at a later stage, the consequences are detrimental. The main focus of cancer research has been on the treatment, the diagnosis research should also be sought after as early diagnosis significantly increases the survival rate. One of the main challenges in cancer treatment is the inability of the drugs to specifically target the tumour cells instead of using their characteristic fast-growing properties. As a result, other fast-growing cells in the body are damaged leading to multiple side effects that impact the patient negatively physically and mentally. Thus, a direct targeting approach to reduce the side effects is essential. As part of research for direct targeting therapy, FA-DABA-PSMA has shown promising results *in vitro*.

In this project, the interaction between FA-DABA-PSMA and FR $\alpha$  was explored using computational and experimental methods. The two were used to determine the binding affinity as well as the binding energy to compare it with the FA – FR $\alpha$  complex. A visual analysis of the structures was performed subsequently to identify the formation of hydrogen between specific amino acids of the receptor with the ligands. Computationally, a significant increase in binding energy was observed with the FA-DABA-PSMA complex compared to the FA complex, as the hydrophilic maleic acids of the polymer were seen forming a hydrogen bond with the amino acids of the receptors on the surface of the receptor. Since the optimization was performed using a trimer of the polymer, with a 350 kDa and 20 kDa chain, it may be able to surround the surface of the receptor. The experimental results from MST also corresponded to the computational simulation. Despite protonation of the receptor by decreasing the pH to 5, the FA-DABA-PSMA 350 kDa and 20 kDa maintained a high binding affinity with the receptor.

Correlating the results, the strong receptor interaction effect exerted by the FA-DABA-PSMA is a combination of strong binding energy and polymer interaction with the acidic protons, prohibiting it from entering the pocket of the receptor, disabling the release of the FA-DABA-PSMA complex. With FR $\alpha$  serving as an important DNA transcription factor, this inability to recycle the receptor would prohibit the proliferation of the tumour cells while promoting FR $\alpha$  expression at the surface of the cell. This feedback loop becomes advantageous as an increase in the FR $\alpha$  on the surface of the cells would allow more intake of the FA-DABA-PSMA, and by starving the nucleus with FR $\alpha$ , it may enter apoptosis. Multiplication of this process would ultimately lead to the death of all tumour cells, eliminating them from the body and curing the person.

With the capability of FA-DABA-PSMA to block the FR $\alpha$ , it becomes an ideal candidate for medical imaging as it is able to target the FR $\alpha$  and maintain a bond to the receptor. The hydrophobic core can encapsulate a radioactive

hydrophobic drug while it's protected by the hydrophilic outer core. As a result, Indium-Oxine was selected as a candidate and characterization was performed using fluorescence spectroscopy, neutron activation analysis, and thin-layer chromatography. It was observed that the In-Oxine must be dissolved in a solvent before addition to the polymer solution to allow encapsulation to occur. The encapsulation of the In-Oxine was also polymer concentration dependent. A higher concentration of FA-DABA-PSMA, 2000  $\mu\text{M}$  was able to encapsulate 71.73% of added In-Oxine. A further analysis using TLC was performed using radioactive  $^{111}\text{In}$ -Oxine at the range of activity desired for *in vivo* testing.  $R_f = 1.0$  was achieved with free  $^{111}\text{In}$ -Oxine while the encapsulated  $^{111}\text{In}$ -Oxine inside FA-DABA-PSMA remained at  $R_f = 0.0$ . Through three different characterizations, it was found that the FA-DABA-PSMA is capable of encapsulating In-Oxine inside its hydrophobic core.

The future of the polymeric carrier, FA-DABA-PSMA can be expanded in three ways. First, cryogenic transmission electron microscopy could be used to visualize the complex structure when FA-DABA-PSMA is bonded to  $\text{FR}\alpha$ . The imaging and modelling could confirm the findings seen from the computer simulation and the MST experiment. A detailed molecular interaction can be visualized, allowing the identification of specific amino acids that form hydrogen bonding with the hydrophilic maleic acid groups of the polymer. An energy calculation can be calculated from the model building and compared to the results obtained previously to determine the accuracy.

Second, with confirmation of  $^{111}\text{In}$ -Oxine encapsulation inside the polymer, *in vivo*, testing should be completed. The *in vivo* imaging using SPECT would allow the calculation of pharmacokinetics and tumour uptake of the FA-DABA-PSMA. This would be a critical study to visualize the movement of FA-DABA-PSMA inside the body. As multiple images can be taken at a specific time frame, the distribution and the excretion of the polymer can be traced. Furthermore, the accumulation of the polymer in the tumour cells can be quantified, which can be used to determine if FA-DABA-PSMA can be used as a diagnostic agent for  $\text{FR}\alpha$  expressed tumours.

Third, based on the results from *in vivo* experiments, the radioactive  $^{111}\text{In}$  can be replaced with  $^{177}\text{Lu}$ , a radioactive isotope that emits beta particles primarily and traces of gamma rays or with  $^{225}\text{Ac}$ , an alpha particle emitter. Currently,  $^{177}\text{Lu}$  has been attached to prostate-specific membrane antigen to directly target and treat prostate cancer <sup>167</sup>.  $^{177}\text{Lu}$  or  $^{225}\text{Ac}$  serves as an ideal replacement for  $^{111}\text{In}$  as both elements carry a charge of 3+ allowing oxines to be used as a chelator to form a hydrophobic compound. Subsequently, with a successful trial using  $^{111}\text{In}$ -Oxine,  $^{177}\text{Lu}$  or  $^{225}\text{Ac}$  can be selected to treat cancer by beta or alpha particle treatment.

The unique micelle-like characteristic of the polymer is a highly promising polymeric carrier for the diagnosis or treatment of  $\text{FR}\alpha$  overexpressed tumours. The polymer is highly flexible, where the FA attached to the polymer can be replaced

with another compound if needed to enhance the targeting effect. The possibility of different combinations of attachment on the polymer using the linker and hydrophobic chemotherapeutic compounds or hydrophobic radiolabeled compounds can be encapsulated inside the polymer for treatment diagnosis, or as a theragnostic. With such promising potential, subsequent research should be continued in hopes of finding an end to the long-lasting war between humanity and cancer, a persistent disease yet to be conquered.

## 8. Reference

1. World Population Prospects 2024, Data Sources.
2. Sung, H. *et al.* Global Cancer Statistics 2020: GLOBOCAN Estimates of Incidence and Mortality Worldwide for 36 Cancers in 185 Countries. *CA. Cancer J. Clin.* **71**, 209–249 (2021).
3. Knowles, M. A. & Selby, P. J. Introduction to the Cellular and Molecular Biology of Cancer.
4. Shurin, M. R. Cancer as an immune-mediated disease. *ImmunoTargets Ther.* **1**, 1–6 (2012).
5. Ferrara, M., Samaden, M., Ruggieri, E. & Vénéreau, E. Cancer cachexia as a multiorgan failure: Reconstruction of the crime scene. *Front. Cell Dev. Biol.* **10**, 960341 (2022).
6. Alhmoud, J. F., Woolley, J. F., Al Moustafa, A.-E. & Malki, M. I. DNA Damage/Repair Management in Cancers. *Cancers* **12**, 1050 (2020).
7. Fares, J., Fares, M. Y., Khachfe, H. H., Salhab, H. A. & Fares, Y. Molecular principles of metastasis: a hallmark of cancer revisited. *Signal Transduct. Target. Ther.* **5**, 1–17 (2020).
8. Guan, X. Cancer metastases: challenges and opportunities. *Acta Pharm. Sin. B* **5**, 402–418 (2015).
9. Hassanpour, S. H. & Dehghani, M. Review of cancer from perspective of molecular. *J. Cancer Res. Pract.* **4**, 127–129 (2017).
10. Hausman, D. M. What Is Cancer? *Perspect. Biol. Med.* **62**, 778–784 (2019).

11. Burningham, Z., Hashibe, M., Spector, L. & Schiffman, J. D. The Epidemiology of Sarcoma. *Clin. Sarcoma Res.* **2**, 14 (2012).
12. Tubiana, M. Tumor Cell Proliferation Kinetics and Tumor Growth Rate. *Acta Oncol.* **28**, 113–121 (1989).
13. Government of Canada, S. C. Five-year cancer survival by stage at diagnosis in Canada. <https://www150.statcan.gc.ca/n1/pub/82-003-x/2023001/article/00001-eng.htm> (2023).
14. Blackadar, C. B. Historical review of the causes of cancer. *World J. Clin. Oncol.* **7**, 54–86 (2016).
15. Baba, A. I. & Câtoi, C. CARCINOGENESIS. in *Comparative Oncology* (The Publishing House of the Romanian Academy, 2007).
16. Ames, B. N., Gold, L. S. & Willett, W. C. The causes and prevention of cancer. *Proc. Natl. Acad. Sci.* **92**, 5258–5265 (1995).
17. Huang, R. & Zhou, P.-K. DNA damage repair: historical perspectives, mechanistic pathways and clinical translation for targeted cancer therapy. *Signal Transduct. Target. Ther.* **6**, 1–35 (2021).
18. Agents Classified by the International Agency for Research on Cancer, World Health Organization, Monographs, Volumes 1–137. <https://monographs.iarc.who.int/agents-classified-by-the-iarc>.
19. D’Orazio, J., Jarrett, S., Amaro-Ortiz, A. & Scott, T. UV Radiation and the Skin. *Int. J. Mol. Sci.* **14**, 12222–12248 (2013).



20. Borrego-Soto, G., Ortiz-López, R. & Rojas-Martínez, A. Ionizing radiation-induced DNA injury and damage detection in patients with breast cancer. *Genet. Mol. Biol.* **38**, 420–432 (2015).
21. Weston, A. & Harris, C. C. Chemical Carcinogenesis. in *Holland-Frei Cancer Medicine. 6th edition* (BC Decker, 2003).
22. Wadgaonkar, P. Chapter 4 - Environmental causes of cancer. in *Cancer Epigenetics and Nanomedicine* (eds. Kesharwani, P. & Thakur, C.) 69–92 (Academic Press, 2024). doi:10.1016/B978-0-443-13209-4.00017-9.
23. Agents Classified by the International Agency for Research on Cancer, World Health Organization, Monographs, Volumes 1–137. <https://monographs.iarc.who.int/agents-classified-by-the-iarc>.
24. Schiller, J. T. & Lowy, D. R. An Introduction to Virus Infections and Human Cancer. *Recent Results Cancer Res. Fortschritte Krebsforsch. Progres Dans Rech. Sur Cancer* **217**, 1–11 (2021).
25. Chen, Y., Williams, V., Filippova, M., Filippov, V. & Duerksen-Hughes, P. Viral Carcinogenesis: Factors Inducing DNA Damage and Virus Integration. *Cancers* **6**, 2155–2186 (2014).
26. Coussens, L. M. & Werb, Z. Inflammation and cancer. *Nature* **420**, 860–867 (2002).
27. Lax, A. J. Bacterial toxins and cancer — a case to answer? *Nat. Rev. Microbiol.* **3**, 343–349 (2005).
28. van Tong, H., Brindley, P. J., Meyer, C. G. & Velavan, T. P. Parasite Infection, Carcinogenesis and Human Malignancy. *EBioMedicine* **15**, 12–23 (2016).

29. Peng, J., Sun, J., Yu, Y., Yuan, Q. & Zhang, Y. Integrative multi-omics analysis reveals the role of toll-like receptor signaling in pancreatic cancer. *Sci. Rep.* **15**, 52 (2025).
30. Pandol, S. J. *The Exocrine Pancreas*. (Morgan & Claypool Life Sciences, San Rafael (CA), 2010).
31. Ro, C., Chai, W., Yu, V. E. & Yu, R. Pancreatic neuroendocrine tumors: biology, diagnosis, and treatment. *Chin. J. Cancer* **32**, 312–324 (2013).
32. Amri, F. *et al.* Association between pancreatic cancer and diabetes: insights from a retrospective cohort study. *BMC Cancer* **23**, 856 (2023).
33. McGuigan, A. *et al.* Pancreatic cancer: A review of clinical diagnosis, epidemiology, treatment and outcomes. *World J. Gastroenterol.* **24**, 4846–4861 (2018).
34. AJCC Cancer Staging Manual. in *AJCC Cancer Staging Manual* (Springer International Publishing, 2017). doi:10.1007/978-3-319-40618-3\_1.
35. Ahles, T. A. & Root, J. C. Cognitive Effects of Cancer and Cancer Treatments. *Annu. Rev. Clin. Psychol.* **14**, 425–451 (2018).
36. Coffman, A., Torgeson, A. & Lloyd, S. Correlates of Refusal of Surgery in the Treatment of Non-metastatic Pancreatic Adenocarcinoma. *Ann. Surg. Oncol.* **26**, 98–108 (2019).
37. Gilbar, O. The quality of life of cancer patients who refuse chemotherapy. *Soc. Sci. Med.* **32**, 1337–1340 (1991).

38. Aslam, M. S. *et al.* Side Effects of Chemotherapy in Cancer Patients and Evaluation of Patients Opinion about Starvation Based Differential Chemotherapy. *J. Cancer Ther.* **5**, 817–822 (2014).
39. Alexakis, N. *et al.* Current standards of surgery for pancreatic cancer. *Br. J. Surg.* **91**, 1410–1427 (2004).
40. Bishop, M. A. & Simo, K. Distal Pancreatectomy. in *StatPearls* (StatPearls Publishing, Treasure Island (FL), 2025).
41. Arvold, N. D., Niemierko, A., Mamon, H. J., Castillo, C. F. & Hong, T. S. Pancreatic Cancer Tumor Size on CT Scan vs. Pathologic Specimen: Implications for Radiation Treatment Planning. *Int. J. Radiat. Oncol. Biol. Phys.* **80**, 1383–1390 (2011).
42. Whipple Procedure. <https://www.hopkinsmedicine.org/health/conditions-and-diseases/pancreatic-cancer/whipple-procedure> (2021).
43. Schabel Jr., F. M. Rationale for adjuvant chemotherapy. *Cancer* **39**, 2875–2882 (1977).
44. Ismail, N. I. & Ibham, S. F. Chemotherapy – Types, Side Effects and Resistance. *J. Tomogr. Syst. Sens. Appl.* **3**, (2020).
45. Malhotra, V. & Perry, M. C. Classical Chemotherapy: Mechanisms, Toxicities and the Therapeutic Window. *Cancer Biol. Ther.* **2**, 1–3 (2003).
46. Nygren, P. What is cancer chemotherapy? *Acta Oncol.* **40**, 166–174 (2001).
47. Hortobágyi, G. N. Anthracyclines in the Treatment of Cancer. *Drugs* **54**, 1–7 (1997).

48. Debela, D. T. *et al.* New approaches and procedures for cancer treatment: Current perspectives. *SAGE Open Med.* **9**, 20503121211034366 (2021).
49. Zugazagoitia, J. *et al.* Current Challenges in Cancer Treatment. *Clin. Ther.* **38**, 1551–1566 (2016).
50. Abshire, D. & Lang, M. K. The Evolution of Radiation Therapy in Treating Cancer. *Semin. Oncol. Nurs.* **34**, 151–157 (2018).
51. Boshuizen, J. & Peeper, D. S. Rational Cancer Treatment Combinations: An Urgent Clinical Need. *Mol. Cell* **78**, 1002–1018 (2020).
52. Anand, U. *et al.* Cancer chemotherapy and beyond: Current status, drug candidates, associated risks and progress in targeted therapeutics. *Genes Dis.* **10**, 1367–1401 (2023).
53. Mokhtari, R. B. *et al.* Combination therapy in combating cancer. *Oncotarget* **8**, 38022–38043 (2017).
54. Eno, J. Immunotherapy Through the Years. *J. Adv. Pract. Oncol.* **8**, 747–753 (2017).
55. Gupta, S. & Shukla, S. Limitations of Immunotherapy in Cancer. *Cureus* **14**, e30856.
56. Mansouri, S., Alharbi, Y. & Alqahtani, A. Current status and prospects for improved targeted delivery approaches for cancer. *Pathol. - Res. Pract.* **253**, 154993 (2024).
57. Bayda, S., Adeel, M., Tuccinardi, T., Cordani, M. & Rizzolio, F. The History of Nanoscience and Nanotechnology: From Chemical–Physical Applications to Nanomedicine. *Molecules* **25**, 112 (2019).

58. Shan, X. *et al.* Current approaches of nanomedicines in the market and various stage of clinical translation. *Acta Pharm. Sin. B* **12**, 3028–3048 (2022).
59. Tian, H., Zhao, F., Qi, Q., Yue, B. & Zhai, B. Targeted drug delivery systems for elemene in cancer therapy: The story thus far. *Biomed. Pharmacother.* **166**, 115331 (2023).
60. McCarthy, D., Malhotra, M., O'Mahony, A., Cryan, J. & O'Driscoll, C. Nanoparticles and the Blood-Brain Barrier: Advancing from In-Vitro Models Towards Therapeutic Significance. *Pharm. Res.* **32**, (2014).
61. Malardier-Jugroot, C. Novel self-assembly of an alternating copolymer into nanotubes: theoretical investigation and experimental characterisation. *McGill University Libraries*, (2004)
62. Li, X., McTaggart, M. & Malardier-Jugroot, C. Synthesis and characterization of a pH responsive folic acid functionalized polymeric drug delivery system. *Biophys. Chem.* **214–215**, 17–26 (2016).
63. DeCarlo, A., Malardier-Jugroot, C. & Szewczuk, M. Folic Acid-Functionalized Nanomedicine: Folic Acid Conjugated Copolymer and Folate Receptor Interactions Disrupt Receptor Functionality Resulting in Dual Therapeutic Anti-Cancer Potential in Breast and Prostate Cancer. *Bioconjug. Chem.* **32**, (2021).
64. Sambi, DeCarlo, Malardier-Jugroot, & Szewczuk. Next-Generation Multimodality of Nanomedicine Therapy: Size and Structure Dependence of Folic Acid Conjugated Copolymers Actively Target Cancer Cells in Disabling Cell Division and Inducing Apoptosis. *Cancers* **11**, 1698 (2019).

65. Lee, S.-H. & Griffiths, J. R. How and Why Are Cancers Acidic? Carbonic Anhydrase IX and the Homeostatic Control of Tumour Extracellular pH. *Cancers* **12**, 1616 (2020).
66. Nanda Karmaker *et al.* Fundamental characteristics and application of radiation. *GSC Adv. Res. Rev.* **7**, 064–072 (2021).
67. Lázaro-Ibáñez, E. *et al.* Selection of Fluorescent, Bioluminescent, and Radioactive Tracers to Accurately Reflect Extracellular Vesicle Biodistribution *in Vivo*. *ACS Nano* **15**, 3212–3227 (2021).
68. Thakur, M. L. Gallium-67 and indium-111 radiopharmaceuticals. *Int. J. Appl. Radiat. Isot.* **28**, 183–201 (1977).
69. Mettler, F. A. & Guiberteau, M. J. 1 - Radioactivity, Radionuclides, and Radiopharmaceuticals. in *Essentials of Nuclear Medicine and Molecular Imaging (Seventh Edition)* (eds. Mettler, F. A. & Guiberteau, M. J.) 1–18 (Elsevier, Philadelphia, 2019). doi:10.1016/B978-0-323-48319-3.00001-8.
70. Jalilian, A. R. *et al.* Production and Clinical Applications of Radiopharmaceuticals and Medical Radioisotopes in Iran. *Semin. Nucl. Med.* **46**, 340–358 (2016).
71. Experimental study of K-electron capture probability in the decay of <sup>111</sup>In. *ResearchGate* (2024).
72. Indium In <sup>111</sup> White Blood Cells. in *Drugs and Lactation Database (LactMed®)* (National Institute of Child Health and Human Development, Bethesda (MD), 2006).

73. Indium In 111 Oxyquinoline. in *Drugs and Lactation Database (LactMed®)* (National Institute of Child Health and Human Development, Bethesda (MD), 2006).
74. Love, C. & Palestro, C. J. Radionuclide Imaging of Infection. *J. Nucl. Med. Technol.* **32**, 47–57 (2004).
75. Folate. *Linus Pauling Institute* <https://lpi.oregonstate.edu/mic/vitamins/folate> (2014).
76. Imbard, A., Benoist, J.-F. & Blom, H. J. Neural Tube Defects, Folic Acid and Methylation. *Int. J. Environ. Res. Public. Health* **10**, 4352–4389 (2013).
77. Greenberg, J. A., Bell, S. J., Guan, Y. & Yu, Y. Folic Acid Supplementation and Pregnancy: More Than Just Neural Tube Defect Prevention. *Rev. Obstet. Gynecol.* **4**, 52–59 (2011).
78. Tjong, E., Dimri, M. & Mohiuddin, S. S. Biochemistry, Tetrahydrofolate. in *StatPearls* (StatPearls Publishing, Treasure Island (FL), 2025).
79. Duthie, S. J., Narayanan, S., Brand, G. M., Pirie, L. & Grant, G. Impact of Folate Deficiency on DNA Stability. *J. Nutr.* **132**, 2444S-2449S (2002).
80. Huang, R.-F. S., Ho, Y.-H., Lin, H.-L., Wei, J.-S. & Liu, T.-Z. Folate Deficiency Induces a Cell Cycle-Specific Apoptosis in HepG2 Cells<sup>123</sup>. *J. Nutr.* **129**, 25–31 (1999).
81. Larenkov, A. *et al.* Pharmacokinetic Properties of <sup>68</sup>Ga-labelled Folic Acid Conjugates: Improvement Using HEHE Tag. *Molecules* **25**, 2712 (2020).

82. Crider, K., Yang, T., Berry, R. & Bailey, L. Folate and DNA Methylation: A Review of Molecular Mechanisms and the Evidence for Folate's Role. *Adv. Nutr. Bethesda Md* **3**, 21–38 (2012).
83. Cai, L. *et al.* Expression status of folate receptor alpha is a predictor of survival in pancreatic ductal adenocarcinoma. *Oncotarget* **8**, 37646–37656 (2017).
84. Young, O. *et al.* Folate Receptor as a Biomarker and Therapeutic Target in Solid Tumors. *Curr. Probl. Cancer* **47**, 100917 (2023).
85. Gonzalez, T., Muminovic, M., Nano, O. & Vulfovich, M. Folate Receptor Alpha—A Novel Approach to Cancer Therapy. *Int. J. Mol. Sci.* **25**, 1046 (2024).
86. Salazar, M. D. & Ratnam, M. The folate receptor: What does it promise in tissue-targeted therapeutics? *Cancer Metastasis Rev.* **26**, 141–152 (2007).
87. Kamen, B. A review of folate receptor alpha cycling and 5-methyltetrahydrofolate accumulation with an emphasis on cell models in vitro. *Adv. Drug Deliv. Rev.* **56**, 1085–1097 (2004).
88. Doucette, M. M. & Stevens, V. L. Folate Receptor Function Is Regulated in Response to Different Cellular Growth Rates in Cultured Mammalian Cells. *J. Nutr.* **131**, 2819–2825 (2001).
89. Fernández, M., Javaid, F. & Chudasama, V. Advances in Targeting the Folate Receptor in the Treatment/Imaging of Cancers. *Chem. Sci.* **9**, (2017).
90. Mohanty, V. *et al.* Folate Receptor Alpha Upregulates *Oct4* , *Sox2* and *Klf4* and Downregulates miR-138 and miR-let-7 in Cranial Neural Crest Cells. *Stem Cells* **34**, 2721–2732 (2016).



91. Boshnjaku, V. *et al.* Nuclear localization of folate receptor alpha: a new role as a transcription factor. *Sci. Rep.* **2**, 980 (2012).
92. Cheng, C.-C. *et al.* Stat3/Oct-4/c-Myc signal circuit for regulating stemness-mediated doxorubicin resistance of triple-negative breast cancer cells and inhibitory effects of WP1066. *Int. J. Oncol.* (2018) doi:10.3892/ijo.2018.4399.
93. Hansen, M. F. *et al.* Folic acid mediates activation of the pro-oncogene STAT3 via the Folate Receptor alpha. *Cell. Signal.* **27**, 1356–1368 (2015).
94. Chen, C. *et al.* Structural basis for molecular recognition of folic acid by folate receptors. *Nature* **500**, 486–489 (2013).
95. Li, X. *et al.* Functionalized Folic Acid-Conjugated Amphiphilic Alternating Copolymer Actively Targets 3D Multicellular Tumour Spheroids and Delivers the Hydrophobic Drug to the Inner Core. *Nanomaterials* **8**, 588 (2018).
96. Aucoin, E. B. *et al.* Glycosyl Mobile Radical Structures of Folic Acid Receptors Impact the Internalization of Functionalized Folate Amphiphilic Alternating Copolymer in Cancer Cells. *Receptors* **3**, 457–473 (2024).
97. Denevault-Sabourin, C., Joubert, N., beck, alain & dumontet, charle. Antibody- Drug Conjugates: The Last Decade. *Pharmaceuticals* **13**, 245 (2020).
98. de la Torre, B. G. & Albericio, F. The Pharmaceutical Industry in 2022: An Analysis of FDA Drug Approvals from the Perspective of Molecules. *Molecules* **28**, 1038 (2023).
99. Broglie, L. D. Recherches sur la théorie des Quanta. *Ann. Phys.* **10**, 22–128 (1925).

100. Schrödinger, E. Quantisierung als Eigenwertproblem. *Ann. Phys.* **384**, 361–376 (1926).
101. Panati, G., Spohn, H. & Teufel, S. The time-dependent Born-Oppenheimer approximation. *ESAIM Math. Model. Numer. Anal.* **41**, 297–314 (2007).
102. Born, M. Quantenmechanik der Stoßvorgänge. *Z. Für Phys.* **38**, 803–827 (1926).
103. (PDF) Molecular Integrals over Slater-type Orbitals. From pioneers to recent progress. in *ResearchGate*.
104. Magalhães, A. L. Gaussian-Type Orbitals versus Slater-Type Orbitals: A Comparison. *J. Chem. Educ.* **91**, 2124–2127 (2014).
105. Fock, V. Näherungsmethode zur Lösung des quantenmechanischen Mehrkörperproblems. *Z. Für Phys.* **61**, 126–148 (1930).
106. The molecular orbital theory of chemical valency VIII. A method of calculating ionization potentials.  
<https://royalsocietypublishing.org/doi/epdf/10.1098/rspa.1951.0048>  
doi:10.1098/rspa.1951.0048.
107. Roothaan, C. C. J. New Developments in Molecular Orbital Theory. *Rev. Mod. Phys.* **23**, 69–89 (1951).
108. Hohenberg, P. & Kohn, W. Inhomogeneous Electron Gas. *Phys. Rev.* **136**, B864–B871 (1964).
109. Kohn, W. & Sham, L. J. Self-Consistent Equations Including Exchange and Correlation Effects. *Phys. Rev.* **140**, A1133–A1138 (1965).

110. Bagayoko, D. Understanding density functional theory (DFT) and completing it in practice. *AIP Adv.* **4**, 127104 (2014).
111. Perdew, J. P. *et al.* Atoms, molecules, solids, and surfaces: Applications of the generalized gradient approximation for exchange and correlation. *Phys. Rev. B* **46**, 6671–6687 (1992).
112. Becke, A. D. Density-functional exchange-energy approximation with correct asymptotic behavior. *Phys. Rev. A* **38**, 3098–3100 (1988).
113. Lee, C., Yang, W. & Parr, R. G. Development of the Colle-Salvetti correlation-energy formula into a functional of the electron density. *Phys. Rev. B* **37**, 785–789 (1988).
114. Elliott, P. & Burke, K. Non-empirical derivation of the parameter in the B88 exchange functional. *Can. J. Chem.* **87**, 1485–1491 (2009).
115. Ho, J., Yu, H., Shao, Y., Taylor, M. & Chen, J. How Accurate Are QM/MM Models? *J. Phys. Chem. A* **129**, 1517–1528 (2025).
116. Thiel, W. Semiempirical quantum–chemical methods. *WIREs Comput. Mol. Sci.* **4**, 145–157 (2014).
117. Wu, Y.-Y., Zhao, F.-Q. & Ju, X.-H. A Comparison of the Accuracy of Semi-empirical PM3, PDDG and PM6 methods in Predicting Heats of Formation for Organic Compounds. *J. Mex. Chem. Soc.* **58**, 223–229 (2014).
118. Molecular Mechanics. in *Computational Chemistry: Introduction to the Theory and Applications of Molecular and Quantum Mechanics* (ed. Lewars, E.) 43–79 (Springer US, Boston, MA, 2003). doi:10.1007/0-306-48391-2\_3.

119. Poltev, V. Molecular Mechanics: Principles, History, and Current Status. in *Handbook of Computational Chemistry* (ed. Leszczynski, J.) 1–48 (Springer Netherlands, Dordrecht, 2016). doi:10.1007/978-94-007-6169-8\_9-2.
120. Vanommeslaeghe, K., Guvench, O. & MacKerell, A. D. Molecular Mechanics. *Curr. Pharm. Des.* **20**, 3281–3292 (2014).
121. Weiner, P. K. & Kollman, P. A. AMBER: Assisted model building with energy refinement. A general program for modeling molecules and their interactions. *J. Comput. Chem.* **2**, 287–303 (1981).
122. Jerabek-Willemsen, M. *et al.* MicroScale Thermophoresis: Interaction analysis and beyond. *J. Mol. Struct.* **1077**, 101–113 (2014).
123. Gaffarogullari, E. C., Krause, A., Balbo, J., Herten, D.-P. & Jäschke, A. Microscale thermophoresis provides insights into mechanism and thermodynamics of ribozyme catalysis. *RNA Biol.* **10**, 1815–1821 (2013).
124. Seidel, S. A. I. *et al.* Microscale Thermophoresis Quantifies Biomolecular Interactions under Previously Challenging Conditions. *Methods San Diego Calif* **59**, 301–315 (2013).
125. Jerabek-Willemsen, M. *et al.* MicroScale Thermophoresis: Interaction analysis and beyond. *J. Mol. Struct.* **1077**, 101–113 (2014).
126. Albani, J. R. *Principles and Applications of Fluorescence Spectroscopy*. (John Wiley & Sons, 2008).
127. Abbyad, P., Childs, W., Shi, X. & Boxer, S. G. Dynamic Stokes shift in green fluorescent protein variants. *Proc. Natl. Acad. Sci. U. S. A.* **104**, 20189–20194 (2007).

128. Schweizer, T., Kubach, H. & Koch, T. Investigations to characterize the interactions of light radiation, engine operating media and fluorescence tracers for the use of qualitative light-induced fluorescence in engine systems. *Automot. Engine Technol.* **6**, 275–287 (2021).
129. Chen, W., Westerhoff, P., Leenheer, J. A. & Booksh, K. Fluorescence Excitation–Emission Matrix Regional Integration to Quantify Spectra for Dissolved Organic Matter. *Environ. Sci. Technol.* **37**, 5701–5710 (2003).
130. What is a Fluorescence Spectrometer? - Edinburgh Instruments. <https://www.edinst.com/resource/what-is-a-fluorescence-spectrometer/>.
131. Valković, V. CHAPTER 5 - Measurements of Radioactivity. in *Radioactivity in the Environment* (ed. Valković, V.) 117–258 (Elsevier Science, Amsterdam, 2000). doi:10.1016/B978-044482954-2.50005-8.
132. R P Parker. Semiconductor nuclear radiation detectors. *Phys. Med. Biol.* **15**, 605–620 (1970).
133. Lab Experiment 7: High-Resolution Gamma-Ray Spectroscopy with HPGe.... *Mirion* <https://www.mirion.com/discover/knowledge-hub/articles/education/high-resolution-gamma-ray-spectroscopy-with-hpge-detectors-lab-experiments>.
134. Meyers, C. L. F. & Meyers, D. J. Thin-Layer Chromatography. *Curr. Protoc. Nucleic Acid Chem.* **34**, (2008).
135. Leblans, P., Vandenbroucke, D. & Willems, P. Storage Phosphors for Medical Imaging. *Materials* **4**, 1034–1086 (2011).

136. Phosphor Imaging. *Azure Biosystems* <https://azurebiosystems.com/western-blotting-applications/phosphor-imaging/>.
137. Cheung, A. *et al.* Targeting folate receptor alpha for cancer treatment. *Oncotarget* **7**, 52553–52574 (2016).
138. Aucoin, E. B. *et al.* Glycosyl Mobile Radical Structures of Folic Acid Receptors Impact the Internalization of Functionalized Folate Amphiphilic Alternating Copolymer in Cancer Cells. *Receptors* **3**, 457–473 (2024).
139. M. J. Frisch *et al.* Gaussian 16. (2016).
140. Dapprich, S., Komáromi, I., Byun, K. S., Morokuma, K. & Frisch, M. J. A new ONIOM implementation in Gaussian98. Part I. The calculation of energies, gradients, vibrational frequencies and electric field derivatives1. *J. Mol. Struct. THEOCHEM* **461–462**, 1–21 (1999).
141. Jurrus, E. *et al.* Improvements to the APBS biomolecular solvation software suite. *Protein Sci. Publ. Protein Soc.* **27**, 112–128 (2018).
142. Wibowo, A. S. *et al.* Structures of human folate receptors reveal biological trafficking states and diversity in folate and antifolate recognition. *Proc. Natl. Acad. Sci. U. S. A.* **110**, 15180–15188 (2013).
143. Lewis, D. F. V. Hydrogen Bonding in Human P450-Substrate Interactions: A Major Contribution to Binding Affinity. *Sci. World J.* **4**, 720301 (2004).
144. (PDF) Hydrogen Bonding in Human P450-Substrate Interactions: A Major Contribution to Binding Affinity. *ResearchGate* (2024) doi:10.1100/tsw.2004.210.

145. Cheung, A. *et al.* Targeting folate receptor alpha for cancer treatment. *Oncotarget* **7**, 52553–52574 (2016).
146. Mosapour Kotena, Z., Razi, M. & Ahmadi, S. Evaluation of hydrogen bonds formation in the selected rare sugars based on 6-31G\* and 6-311++G(d,p) basis sets. *J. Mol. Model.* **27**, 315 (2021).
147. Del Bene, J. E., Person, W. B. & Szczepaniak, K. Properties of Hydrogen-Bonded Complexes Obtained from the B3LYP Functional with 6-31G(d,p) and 6-31+G(d,p) Basis Sets: Comparison with MP2/6-31+G(d,p) Results and Experimental Data. *J. Phys. Chem.* **99**, 10705–10707 (1995).
148. Antony, A. C. Folate Receptors. *Annu. Rev. Nutr.* **16**, 501–521 (1996).
149. Jackman, A. Antifolates targeted specifically to the folate receptor. *Adv. Drug Deliv. Rev.* **56**, 1111–1125 (2004).
150. Rijnboutt, S. *et al.* Endocytosis of GPI-linked membrane folate receptor-alpha. *J. Cell Biol.* **132**, 35–47 (1996).
151. Boidin, L. *et al.* Targeted Photodynamic Therapy using a Vectorized Photosensitizer coupled to Folic Acid Analog induces Ovarian Tumor Cell Death and inhibits IL-6-mediated Inflammation. *J. Controlled Release* **371**, 351–370 (2024).
152. Wibowo, A. S. *et al.* Structures of human folate receptors reveal biological trafficking states and diversity in folate and antifolate recognition. *Proc. Natl. Acad. Sci.* **110**, 15180–15188 (2013).
153. Webb, B. A. *et al.* pHLARE: a new biosensor reveals decreased lysosome pH in cancer cells. *Mol. Biol. Cell* **32**, 131–142 (2021).

154. Kamen, B. A. & Smith, A. K. A review of folate receptor alpha cycling and 5-methyltetrahydrofolate accumulation with an emphasis on cell models in vitro. *Adv. Drug Deliv. Rev.* **56**, 1085–1097 (2004).
155. Zhang, L., Sanagapalli, S. & Stoita, A. Challenges in diagnosis of pancreatic cancer. *World J. Gastroenterol.* **24**, 2047–2060 (2018).
156. Fass, L. Imaging and cancer: A review. *Mol. Oncol.* **2**, 115–152 (2008).
157. Brugarolas, P. *et al.* Fifty Years of Radiopharmaceuticals. *J. Nucl. Med. Technol.* **48**, 34S–39S (2020).
158. Ashraf, M. A. & Goyal, A. Fludeoxyglucose (18F). in *StatPearls* (StatPearls Publishing, Treasure Island (FL), 2025).
159. Dhoundiyal, S. *et al.* Radiopharmaceuticals: navigating the frontier of precision medicine and therapeutic innovation. *Eur. J. Med. Res.* **29**, 26 (2024).
160. Zhang, S. *et al.* Radiopharmaceuticals and their applications in medicine. *Signal Transduct. Target. Ther.* **10**, 1–51 (2025).
161. Roca, M., de Vries, E. F. J., Jamar, F., Israel, O. & Signore, A. Guidelines for the labelling of leucocytes with 111In-oxine. *Eur. J. Nucl. Med. Mol. Imaging* **37**, 835–841 (2010).
162. Chang, S. S. Overview of Prostate-Specific Membrane Antigen. *Rev. Urol.* **6**, S13–S18 (2004).
163. de la Fuente, A. *et al.* 68Ga[Ga]-, 111In[In]-oxine: a novel strategy of in situ radiolabeling of HPMA-based micelles. *Am. J. Nucl. Med. Mol. Imaging* **9**, 67–83 (2019).



164. Herron, T. & Gossman, W. 111 Indium White Blood Cell Scan. in *StatPearls* (StatPearls Publishing, Treasure Island (FL), 2025).
165. Tsibulsky, W. L. & Amit, Z. Tolerance to effects of high doses of ethanol: 1. Lethal effects in mice. *Pharmacol. Biochem. Behav.* **45**, 465–472 (1993).
166. de la Fuente, A. *et al.* 68Ga[Ga]-, 111In[In]-oxine: a novel strategy of in situ radiolabeling of HPMA-based micelles. *Am. J. Nucl. Med. Mol. Imaging* **9**, 67–83 (2019).
167. Sartor, O. *et al.* Lutetium-177–PSMA-617 for Metastatic Castration-Resistant Prostate Cancer. *N. Engl. J. Med.* **385**, 1091–1103 (2021).